



**HAL**  
open science

## Arterial spin labelling: quality control and super-resolution

Cédric Meurée

► **To cite this version:**

Cédric Meurée. Arterial spin labelling: quality control and super-resolution. Medical Imaging. Université de Rennes, 2019. English. NNT : 2019REN1S016 . tel-02281778

**HAL Id: tel-02281778**

**<https://theses.hal.science/tel-02281778>**

Submitted on 9 Sep 2019

**HAL** is a multi-disciplinary open access archive for the deposit and dissemination of scientific research documents, whether they are published or not. The documents may come from teaching and research institutions in France or abroad, or from public or private research centers.

L'archive ouverte pluridisciplinaire **HAL**, est destinée au dépôt et à la diffusion de documents scientifiques de niveau recherche, publiés ou non, émanant des établissements d'enseignement et de recherche français ou étrangers, des laboratoires publics ou privés.

# THÈSE DE DOCTORAT DE

L'UNIVERSITE DE RENNES 1  
COMUE UNIVERSITE BRETAGNE LOIRE

Ecole Doctorale N°601  
*Mathématique et Sciences et Technologies  
de l'Information et de la Communication*  
Spécialité : *Mathématiques et leurs Interactions*  
Par

**Cédric MEURÉE**

**Arterial spin labelling : quality control and super-resolution**

Thèse présentée et soutenue à RENNES, le 25 mars 2019  
Unité de recherche : VisAGeS

## Rapporteurs avant soutenance :

Xavier GOLAY	Professor, University College London
Florence FORBES	Directrice de recherche, INRIA Grenoble Rhône-Alpes

## Composition du jury :

Président :	Jean-François MANGIN	Directeur de recherche, CEA
Examineurs :	Xavier GOLAY	Professor, University College London
	Florence FORBES	Directrice de recherche, INRIA Grenoble Rhône-Alpes
	Jan WARNKING	Chargé de recherche, Université de Grenoble
	Pierre MAUREL	Maître de conférences, ESIR Rennes
Dir. de thèse :	Christian BARILLOT	Directeur de recherche, CNRS
Co-dir. de thèse :	Jean-Christophe FERRÉ	Professeur, CHU de Rennes



---

## **Titre : Arterial spin labelling : contrôle qualité et super-résolution**

**Mot clés :** Arterial spin labelling, qualité, distorsions, super-résolution

**Resumé :** L'arterial spin labelling (ASL) est une technique d'imagerie par résonance magnétique de la perfusion cérébrale. Les travaux présentés dans cette thèse ont d'abord consisté à standardiser les acquisitions ASL dans le contexte d'études de neuroimagerie multicentriques. Un processus de contrôle de la qualité des images a par la suite été proposé. Les travaux se sont ensuite orientés vers le post-traitement de données ASL, en évaluant la capacité d'algorithmes existants à y corriger les distorsions. Des méthodes de super-résolution adaptées aux acquisitions ASL mono et multi-TI ont finalement été proposées et validées sur des données simulées, de sujets sains, ou de patients imagés pour suspicion de tumeurs cérébrales.

---

## **Title : Arterial spin labelling : quality control and super-resolution**

**Keywords :** Arterial spin labelling, quality, distortions, super-resolution

**Abstract :** Arterial spin labelling (ASL) is a brain perfusion magnetic resonance imaging technique. The objective of this thesis was first to standardize ASL acquisitions in the context of multicenter neuroimaging studies. A quality control procedure has then been proposed. The capacity of existing algorithms to correct for distortions in ASL images has then been evaluated. Super-resolution methods, developed and adapted to single and multi-TI ASL data in the context of this thesis, are then described, and validated on simulated data, images acquired on healthy subjects, and on patients imaged for brain tumours.



## Acknowledgments

I would like to start by thanking Christian Barillot for his support, trust, enthusiasm, informed advices, and for sharing his experience in the medical imaging field that guided and oriented much of the work, and some professional and personal decisions taken during these 55 months spent as a member of the VisAGeS team. Together with Jean-Christophe Ferré and Pierre Maurel, they have always been available to help me to learn the aspects that go with research activities, and provide feedback through the good and more difficult moments of this PhD, each of them with their own experience and personality.

A particular thank you to Isabelle Corouge and Élise Bannier, for following the work, helping in a lot of aspects, and also providing lots of advice since I joined the team.

I would like to thank Christian Bert, Andrea Plank, Matthieu Lepetit-Coiffé, Marc Lapert, and Thomas Troalen, for their support from the Siemens Healthineers side. Thank you to Matthieu again, and to Josef Pfeuffer, for making the one month stay at Siemens Healthineers, Erlangen, possible. Working there with the neuro pre-development team, together with Rune Monzel, on the integration of the method developed during this thesis with the tools used by the team was a particularly formative experience.

Many thanks to Marie Chupin and Jean-François Mangin for their support during the months spent as a CATI engineer, and to Jan Warnking, for participating in the study conducted during this period, and his precious advices as a member of my thesis committee.

I would also like to thank all the VisAGeS members, and former VisAGeS members, with whom I had really great times, at IRISA, as well as outside. Thanks to the Empub, squash, babyfoot, padel, badminton, running teams, and the C107-Bleu office, for all the great moments.

Working on this thesis would not have been possible without the help and support provided by my friends, and I would like to thank them, for the huge role that they have played during this journey. I can assure you that it has always been a pleasure to have you ask this question: How is it going with your thesis ?

I would also like to thank my parents, my sister, and my grandparents, who also fulfilled a very important role, through their immense support, and this since well before the beginning of this thesis. Vanessa, thank you for being at my side through these times. Finally, I have a thought for my grandparents, Denise and Léon Meurée, who have always been there for me. I would like to dedicate this manuscript to them.

Cédric Meurée



# Contents

<b>Résumé en français</b>	<b>i</b>
R.1 Contexte . . . . .	iii
R.1.1 Perfusion cérébrale . . . . .	iii
R.1.2 Arterial spin labelling . . . . .	iii
R.2 Évaluation de la qualité des images ASL . . . . .	iv
R.2.1 Standardisation des séquences et évaluation de la qualité des images dans des études multicentriques . . . . .	iv
R.2.2 Correction des distorsions . . . . .	vii
R.3 Méthodes de post-traitement des images ASL . . . . .	viii
R.3.1 Super-résolution adaptée aux cartes de CBF . . . . .	viii
R.3.2 Super-résolution adaptée aux acquisitions d'ASL multi-TI . . . . .	xiii
R.4 Discussion et perspectives . . . . .	xiv
<b>I Context and objectives</b>	<b>1</b>
<b>1 Brain perfusion: a general presentation</b>	<b>3</b>
1.1 Introduction . . . . .	4
1.2 General presentation of the human brain . . . . .	4
1.3 Brain perfusion . . . . .	5
1.3.1 Blood supply . . . . .	5
1.3.2 Parameters . . . . .	6
1.3.3 Applications . . . . .	6
1.4 Perfusion imaging techniques . . . . .	11
1.4.1 Positron Emission Tomography . . . . .	11
1.4.2 Single Photon Emission Computed Tomography . . . . .	11
1.4.3 Computed Tomography . . . . .	12
1.4.4 Dynamic Susceptibility Contrast . . . . .	12
1.4.5 Arterial Spin labelling . . . . .	13
<b>2 Arterial Spin labelling</b>	<b>15</b>
2.1 Introduction . . . . .	16
2.2 Basic principle . . . . .	16
2.3 Labelling approaches . . . . .	16
2.3.1 Continuous ASL . . . . .	16
2.3.2 Pulsed ASL . . . . .	18
2.3.3 Pseudo-continuous ASL . . . . .	19
2.3.4 Vessel encoded pCASL . . . . .	19
2.4 Acquisition parameters . . . . .	20
2.4.1 Labelling duration and post-labelling delay . . . . .	20



2.4.2	Single-TI and multi-TI acquisitions . . . . .	20
2.4.3	Background suppression . . . . .	21
2.4.4	Readout approaches . . . . .	21
2.4.5	Vascular flow crushing gradients . . . . .	23
2.5	ASL signal models . . . . .	23
2.5.1	General kinetic model . . . . .	23
2.5.2	Standard kinetic model . . . . .	24
2.5.3	Two compartment model . . . . .	26
2.6	Processing pipelines . . . . .	27
2.6.1	Single-TI ASL image processing pipeline . . . . .	27
2.6.2	Multi-TI image processing pipeline . . . . .	28
2.7	Thesis objectives . . . . .	31
<b>II</b>	<b>Image quality assessment</b>	<b>35</b>
<b>3</b>	<b>Standardization and quality assessment of ASL scans in multicenter neuroimaging studies</b>	<b>37</b>
3.1	Introduction . . . . .	38
3.2	Acquisition parameters standardization . . . . .	38
3.2.1	Material and method . . . . .	40
3.2.2	Results . . . . .	42
3.2.3	Conclusion . . . . .	43
3.3	Artifacts . . . . .	45
3.3.1	Motion . . . . .	45
3.3.2	Vascular artifacts (hyperintense ASL signal) . . . . .	46
3.3.3	Signal inhomogeneities . . . . .	46
3.3.4	Parallel imaging . . . . .	46
3.3.5	Distortion . . . . .	48
3.3.6	Conclusion . . . . .	48
3.4	Implemented quality assessment method . . . . .	48
3.4.1	Acquisition parameters conformity assessment . . . . .	49
3.4.2	ASL images quality assessment . . . . .	49
3.5	Discussion . . . . .	53
<b>4</b>	<b>Distortion correction</b>	<b>55</b>
4.1	Introduction . . . . .	56
4.2	Material and methods . . . . .	57
4.2.1	Healthy subjects dataset . . . . .	57
4.2.2	Methods . . . . .	57
4.3	Results . . . . .	58
4.4	Discussion . . . . .	60

---

<b>III Post-processing methods</b>	<b>63</b>
<b>5 CBF maps super-resolution</b>	<b>65</b>
5.1 Introduction . . . . .	66
5.2 Materials and Methods . . . . .	67
5.2.1 Summary of existing similarity-based SR methods . . . . .	67
5.2.2 A new SR method for ASL images . . . . .	68
5.2.3 Validation framework . . . . .	70
5.2.4 Implementation details . . . . .	73
5.3 Results . . . . .	73
5.3.1 Simulated dataset . . . . .	73
5.3.2 Healthy controls . . . . .	74
5.3.3 Comparison with DSC . . . . .	75
5.4 Comparison with Partial Volume Correction methods . . . . .	76
5.4.1 Method . . . . .	76
5.4.2 Results . . . . .	79
5.5 Discussion . . . . .	81
<b>6 Multi-TI ASL super-resolution</b>	<b>85</b>
6.1 Introduction . . . . .	86
6.2 Material and methods . . . . .	86
6.2.1 Non-local spatio-temporal super-resolution method . . . . .	86
6.2.2 Method evaluation . . . . .	87
6.2.3 Implementation details . . . . .	91
6.3 Results . . . . .	91
6.3.1 Simulated dataset . . . . .	91
6.3.2 Healthy subjects . . . . .	92
6.4 Discussion . . . . .	99
<b>Conclusion</b>	<b>101</b>
<b>List of Abbreviations</b>	<b>105</b>
<b>List of Figures</b>	<b>107</b>
<b>List of Tables</b>	<b>112</b>
<b>Bibliography</b>	<b>115</b>
<b>Communications</b>	<b>131</b>



# Résumé en français

---

Ce chapitre propose un résumé en français du manuscrit, rédigé en anglais, en ayant pour objectif de conserver une structure similaire à celle du reste du document.

Le travail réalisé dans le cadre de cette thèse est présenté de manière progressive. La démarche adoptée afin de standardiser les acquisitions d'images d'arterial spin labelling (ASL), ainsi que d'effectuer un contrôle de la qualité de ces acquisitions dans le cadre d'études de neuroimagerie multi-centriques est décrite dans un premier temps. Une étude d'évaluation de la capacité d'algorithmes existants à corriger les distorsions dans les images ASL est ensuite présentée. Les descriptions et évaluations de méthodes de super-résolution adaptées aux images ASL, proposées dans le cadre de cette thèse, sont présentées dans la partie suivante. Une méthode est tout d'abord adaptée aux cartes de débit sanguin cérébral, puis étendue au cas d'acquisitions de type multi-TI, en tenant compte de l'évolution temporelle du signal ASL.

In this chapter, we provide a French summary of the work presented in the rest of the manuscript. Non-french speakers can easily skip this chapter.

**Contents**

---

<b>R.1</b>	<b>Contexte . . . . .</b>	<b>iii</b>
	R.1.1 Perfusion cérébrale . . . . .	iii
	R.1.2 Arterial spin labelling . . . . .	iii
<b>R.2</b>	<b>Évaluation de la qualité des images ASL . . . . .</b>	<b>iv</b>
	R.2.1 Standardisation des séquences et évaluation de la qualité des images dans des études multicentriques . . . . .	iv
	R.2.2 Correction des distorsions . . . . .	vii
<b>R.3</b>	<b>Méthodes de post-traitement des images ASL . . . . .</b>	<b>viii</b>
	R.3.1 Super-résolution adaptée aux cartes de CBF . . . . .	viii
	R.3.2 Super-résolution adaptée aux acquisitions d'ASL multi-TI . .	xiii
<b>R.4</b>	<b>Discussion et perspectives . . . . .</b>	<b>xiv</b>

---

## R.1 Contexte

### R.1.1 Perfusion cérébrale

Le développement spectaculaire des techniques permettant l'étude du cerveau ces dernières décennies a permis de grandement augmenter les connaissances au sujet de cet organe, que ce soit sur les plans de sa structure ou de son fonctionnement. Beaucoup reste toutefois à découvrir à son sujet, ce qui explique le fait que d'importants moyens soient encore alloués aux études le concernant. Dans le cadre de cette thèse, nous nous intéressons en particulier à une méthode d'imagerie par résonance magnétique (IRM) de la perfusion cérébrale, appelée marquage de spins artériels (arterial spin labelling en anglais, d'où l'acronyme couramment utilisé d'ASL).

La perfusion cérébrale consiste en l'apport par le sang d'oxygène et de nutriments aux tissus du cerveau. Elle est surtout étudiée au niveau de la microcirculation, qui a lieu dans les vaisseaux des plus fins du système sanguin, les capillaires. Différents paramètres sont rencontrés dans la littérature afin de caractériser cette perfusion. Les plus couramment mentionnés en ASL sont le débit sanguin cérébral (CBF), exprimé en millilitres par minute pour cent grammes de tissus cérébraux ( $\text{ml}\cdot\text{min}^{-1}\cdot 100\text{g}$ ), et le temps de transit artériel (ATT), exprimé en secondes ou millisecondes.

Évaluer la perfusion cérébrale présente un intérêt dans de nombreuses pathologies, telles que les troubles cérébraux vasculaires, les cancers, les démences, certaines maladies psychiatriques ou encore l'épilepsie. Bien qu'un certain nombre de dispositifs d'imagerie permettent d'évaluer cette perfusion, l'ASL se révèle être de plus en plus utilisée dans le contexte clinique, mais encore surtout dans le cadre de travaux de recherche. En effet, cette technique a comme avantage par rapport aux autres méthodes de reposer sur l'utilisation de marqueurs endogènes, présents naturellement dans l'organisme des sujets imagés, en opposition à l'injection ou l'inhalation de produits de contraste, nécessaire pour pouvoir utiliser les autres méthodes.

### R.1.2 Arterial spin labelling

En ASL, afin de créer les marqueurs endogènes, des impulsions radiofréquences sont générés, qui modifient l'aimantation des atomes d'hydrogène des molécules d'eau présentes dans le sang au niveau du cou des sujets dont le cerveau est imagé, ces molécules étant destinées à perfuser dans les tissus cérébraux. Après une durée déterminée, appelée délai post-marquage (PLD), une image est acquise. Par différence entre cette image marquée et une image contrôle, qui en diffère de par l'absence de marquage avant son acquisition, on obtient une carte de perfusion. Le signal présent dans une telle carte est associé à un faible rapport signal à bruit (SNR), ce qui implique le fait qu'une trentaine de paires d'images contrôle et label soient généralement acquises. Différents modes de marquage ont été proposés depuis l'émergence de l'ASL. Les deux modes rencontrés dans le cadre de ces travaux de thèse sont le marquage pulsé (PASL), et le marquage pseudo-continu (pCASL). En PASL, les spins sont très rapidement marquées sur une large zone, alors qu'en

pCASL, les spins sont marqués en passant à travers un plan pendant une certaine durée de marquage (LD).

L'acquisition de données ASL peut se faire suivant une approche mono-TI, qui consiste à acquérir les images marquées en attendant une durée fixe après le marquage des spins. Les acquisitions mono-TI permettent la quantification du CBF. L'approche multi-TI repose quant à elle sur l'acquisition d'images marquées avec différentes valeurs de PLD, permettant ainsi l'estimation de paramètres supplémentaires tels que l'ATT.

Dans le cadre de cette thèse, la quantification des paramètres liés à la perfusion cérébrale est effectuée à l'aide du modèle standard de Buxton [Buxton 1998].

## R.2 Évaluation de la qualité des images ASL

### R.2.1 Standardisation des séquences et évaluation de la qualité des images dans des études multicentriques

#### R.2.1.1 Introduction

Ce travail a été réalisé en lien avec le centre pour l'acquisition et le traitement des images (CATI), une plateforme nationale qui a pour objectif d'apporter un support à des études de neuroimagerie multicentriques. L'objectif était ici de permettre l'inclusion de séquences d'acquisition d'images ASL dans les protocoles d'imagerie pilotés par cette plateforme. Dans un premier temps, le travail a consisté à standardiser les séquences d'acquisition sur des machines IRM de deux constructeurs différents. Dans un second temps, un outil d'évaluation semi-automatique de la qualité des images acquises par différents centres participant aux acquisitions a été développé et intégré au logiciel de contrôle qualité du CATI.

#### R.2.1.2 Standardisation des paramètres d'acquisition

**Matériel et méthode** La plupart des IRM participant aux études de neuroimagerie pilotées par le CATI étant équipées de séquences de type 2D-EPI, le travail de standardisation a été concentré sur de telles séquences. 10 sujets (6 femmes, 4 hommes,  $53 \pm 17$  ans) et un patient diagnostiqué avec une forme de démence (homme, 69 ans) se sont portés volontaires pour participer à cette étude. 7 sujets sains et le patient ont été imagés sur une IRM, appelée A dans la suite de cette section, et 3 sujets sains sur l'IRM B. Le protocole était constitué d'une image structurale (MPRAGE), une séquence 2D-EPI pCASL, et une image de la magnétisation à l'équilibre ( $M_0$ ). Les images de l'un des sujets imagés sur le scanner A ont du être exclues de l'étude pour cause de mauvaise qualité.

Les paramètres d'acquisition à optimiser étaient le temps de répétition (TR), le temps d'écho (TE), la durée de marquage (LD), ainsi que le délai post-marquage (PLD). Bien que la valeur de PLD recommandée pour l'imagerie de sujets adultes soit de 2000 ms [Alsop 2015], nous souhaitions en effet évaluer la possibilité de

l’allonger. En effet, les structures d’intérêt dans le cas de démences sont généralement situées dans la moitié inférieure du cerveau, les images ASL pouvant être impactées par des artefacts artériels dans ces régions en cas de trop faibles valeurs de PLD. Les combinaisons de paramètres évaluées, ainsi que le nombre de sujets imagés avec chacune de ces combinaisons, sont présentés dans le tableau 1. Un sujet supplémentaire a été imagé sur l’IRM A, afin d’évaluer l’influence des méthodes d’imagerie parallèle GRAPPA et SENSE.

Des analyses automatiques quantitatives, telles que les calculs de SNR temporel et de CBF, ainsi que des évaluations qualitatives réalisées par un neuroradiologue expérimenté ont permis de procéder au choix des paramètres les mieux appropriés, et à utiliser afin d’acquérir les images ASL dans le cadre des protocoles pilotés par le CATI.

**Résultats** Suite aux analyses quantitatives et qualitatives effectuées, et répertoriées dans le tableau 1, les paramètres sélectionnés sont LD=1800 ms, PLD=2170 ms, TR=4560 ms et TE=12 ms. SENSE avec un facteur d’accélération égal à 2 est quant à elle la méthode d’imagerie parallèle choisie.

LD	PLD	TR	TE	Subjects	tSNR scanner A	tSNR scanner B	CBF	Visual score
1650	2020	min	12	2		12.39		0*
	2170	min	12	2	8.01		29.74	0*
		4560	12	2	6.35		46.75	0*
1800	2020	min	min	2		12.28		2.5
			12	7	8.19	13.82	31.92	2*
		4560	12	7	7.06	11.41	28.64	2*
	2170	min	12	4	5.53		32.71	2
		4560	12	3	6.89		34.27	2.33
	2370	4560	12	4	6.71		29.79	1

Table 1: Nombre de sujets imagés par combinaison de paramètres, SNR temporel et CBF calculés sur des masques de cerveaux, et scores d’évaluation visuelle associés aux acquisitions ASL. Les astérisques indiquent qu’au moins l’une des cartes de CBF obtenues à partir des paramètres associés présentait un hypersignal artériel.

**Conclusion** Suite à la sélection de ces paramètres d’acquisition, des visites ont été programmées sur différents sites afin d’y installer les séquences ASL. Le développement d’un outil semi-automatique de contrôle de la qualité des images ASL a ensuite été réalisé, dans le but d’être utilisé par les attachés de recherche clinique, premières personnes du CATI à recevoir ces images.

### R.2.1.3 Développement d’un outil de contrôle de la qualité des images

**Vérification des paramètres d’acquisition** La première étape du contrôle qualité consiste à vérifier la conformité des paramètres d’acquisition. Pour ce faire, les paramètres d’intérêt sont cherchés dans les fichiers DICOM, format dans lequel les images sont partagées par les sites d’acquisition. Les paramètres analysés



sont le nom de l'antenne, le champ de vue, la matrice d'acquisition, l'épaisseur de coupe, l'espacement entre les coupes, l'orientation, la direction d'encodage de phase, l'espacement entre les pixels, le temps de répétition, l'angle de bascule, la largeur de bande, le nombre de répétitions, la correction de champ  $B_1$ , l'acquisition de Fourier partielle, la méthode d'imagerie parallèle, le facteur d'imagerie parallèle, le suréchantillonnage de phase et le temps d'écho.

**Évaluation de la qualité des images** Les données ASL sont traitées à l'aide d'un pipeline développé dans le cadre de ce travail, basé sur des fonctions propres développées en Python et des fonctionnalités de SPM8 [SPM 2006]. Des images obtenues à différents stades de ces traitements sont affichées sur l'interface mis à la disposition des attachés de recherche clinique, comme présenté dans la figure 1. Des champs spécifiques aux conditions générales de l'acquisition, ainsi que des évaluations d'artefacts plus précises doivent ensuite être renseignés par l'utilisateur. Un rapport contenant l'ensemble des évaluations réalisées sur ces données ainsi qu'une note de qualité finale sont finalement créés et sauvegardés dans la base de données du CATI.

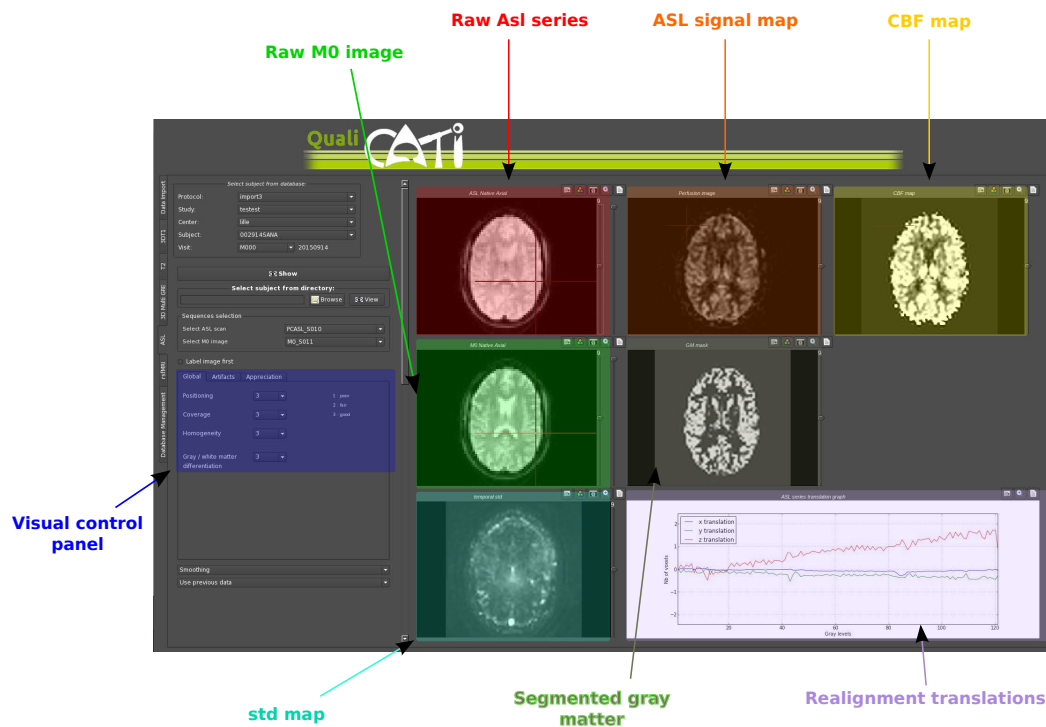


Figure 1: Interface graphique (*qualiCATI*), sur laquelle sont affichés des images et graphiques issus du post-traitement des données ASL.

#### R.2.1.4 Discussion

Ces travaux de standardisation des acquisitions d'images ASL et de contrôle de leur qualité ont permis d'évaluer des données provenant de 191 patients imagés dans le cadre d'un projet portant sur l'étude des relations entre facteurs de risques vasculaires et démences. 184 de ces patients ont effectivement été imagés avec la séquence ASL proposée. 104 de ces images ont été répertoriées comme étant de très bonne qualité, 59 d'une qualité acceptable, et 21 (11%) ont été écartées de l'étude, taux considéré comme satisfaisant.

### R.2.2 Correction des distorsions

#### R.2.2.1 Introduction

Le recours à des techniques d'acquisition rapides pour obtenir les données ASL, telles que la méthode 2D-EPI, induit parfois l'introduction de distorsions dans les images. Celles-ci apparaissent dans des régions sujettes à d'importantes différences de susceptibilité magnétique, en particulier au niveau des interfaces air/tissu ou tissu/os. Différentes méthodes ont été proposées afin de corriger ces distorsions, et appliquées à des images de diffusion, d'IRM fonctionnelle, ou encore de contraste de susceptibilité magnétique (DSC). Une méthode reposant sur l'acquisition d'images dont les directions d'encodage de phase (PED) sont inversées se révèle notamment produire des résultats encourageants. Une implémentation de cette technique, TOPUP [Andersson 2003], a été appliquée à des images ASL dans le travail de [Madai 2016]. L'objectif du travail présenté dans cette section est d'évaluer la capacité de trois méthodes qui reposent sur ce principe d'acquisition de données avec des PED inversées à corriger les distorsions dans les images ASL. Les trois méthodes évaluées sont TOPUP, HySCO [Ruthotto 2012, Ruthotto 2013], et l'algorithme Block Matching proposé par [Hedouin 2017].

#### R.2.2.2 Matériel et méthodes

5 sujets se sont portés volontaires pour participer à cette étude (2 femmes, 3 hommes,  $22 \pm 1.58$  ans). Une image structurale (MPRAGE) a été acquise pour chacun des sujets, ainsi que 4 séries pCASL et les cartes de magnétisation à l'équilibre ( $M_0$ ) associées obtenues avec des PED orientées en  $A \gg P$ ,  $P \gg A$ ,  $R \gg L$  et  $L \gg R$ .

Chacune des séries pCASL et des cartes  $M_0$  a été corrigée à l'aide des trois méthodes évaluées, avant que le CBF ne soit estimé à partir de celles-ci à l'aide d'une chaîne de traitement développée en Python et SPM8. Afin d'évaluer la capacité de chacune des techniques à corriger les distorsions de manière satisfaisante, la corrélation et l'indice de similarité structurale (SSIM) entre les cartes de CBF issues des données acquises suivant les PED inverses ont été calculés. Ces deux indices ont également été mesurés entre les images acquises en  $A \gg P$  et  $L \gg R$ .

### R.2.2.3 Résultats

Les cartes de CBF (figure 2), ainsi que les valeurs de corrélations et SSIM obtenues, indiquent que la méthode HySCO génère des images corrigées plus lisses que les deux autres méthodes, entraînant l'atténuation de certains détails. TOPUP et Block Matching parviennent quant à elles à corriger les distorsions et rapprocher les images acquises avec des PED opposées, tout en conservant des structures bien détaillées. En outre, les indices mesurés tendent à souligner une meilleure performance de la méthode Block Matching.

### R.2.2.4 Discussion

Cette étude amène à privilégier les algorithmes TOPUP et Block Matching afin de corriger les distorsions dans les images ASL, la seconde tendant à fournir des reconstructions d'une qualité légèrement supérieure à la première.

## R.3 Méthodes de post-traitement des images ASL

### R.3.1 Super-résolution adaptée aux cartes de CBF

#### R.3.1.1 Introduction

Cette section présente des méthodes proposées dans le cadre de cette thèse, avec pour objectif de réduire l'influence de certaines limitations propres aux acquisitions ASL. Les aspects principaux pris en compte dans le développement et l'adaptation de ces méthodes à l'ASL sont sa faible résolution spatiale, les effets de volumes partiels (PVE) engendrés par celle-ci, ainsi que le faible SNR des images acquises. Les travaux sont basés sur des méthodes rencontrées dans la littérature et appliquées à des images structurales, de cartographie quantitative de temps de relaxation  $T_1$ , de diffusion, ou de spectroscopie. Il s'agit de méthodes de super-résolution basées sur l'utilisation de patches, qui ont la particularité de recourir à des images structurales acquises à des résolutions élevées afin de guider la reconstruction des images d'intérêt à une résolution supérieure à celle à laquelle elles ont été acquises.

#### R.3.1.2 Matériel et méthodes

**Méthodes de super-résolution par patches** Les méthodes de super-résolution basées sur l'utilisation de patches reposent sur une hypothèse principale, selon laquelle des similitudes entre différentes régions d'une image médicale sont liées à des processus physiologiques similaires. L'évaluation de similarités entre différents patches, à la fois dans l'image à reconstruire et dans une image structurale directement acquise à une résolution élevée peut ainsi guider la reconstruction. Une étape de régularisation, qui veille à une bonne correspondance entre les images reconstruites et les images de basse résolution (BR) originales, est généralement appliquée dans ces techniques. Cette étape est par ailleurs la principale limitation de ces méthodes,

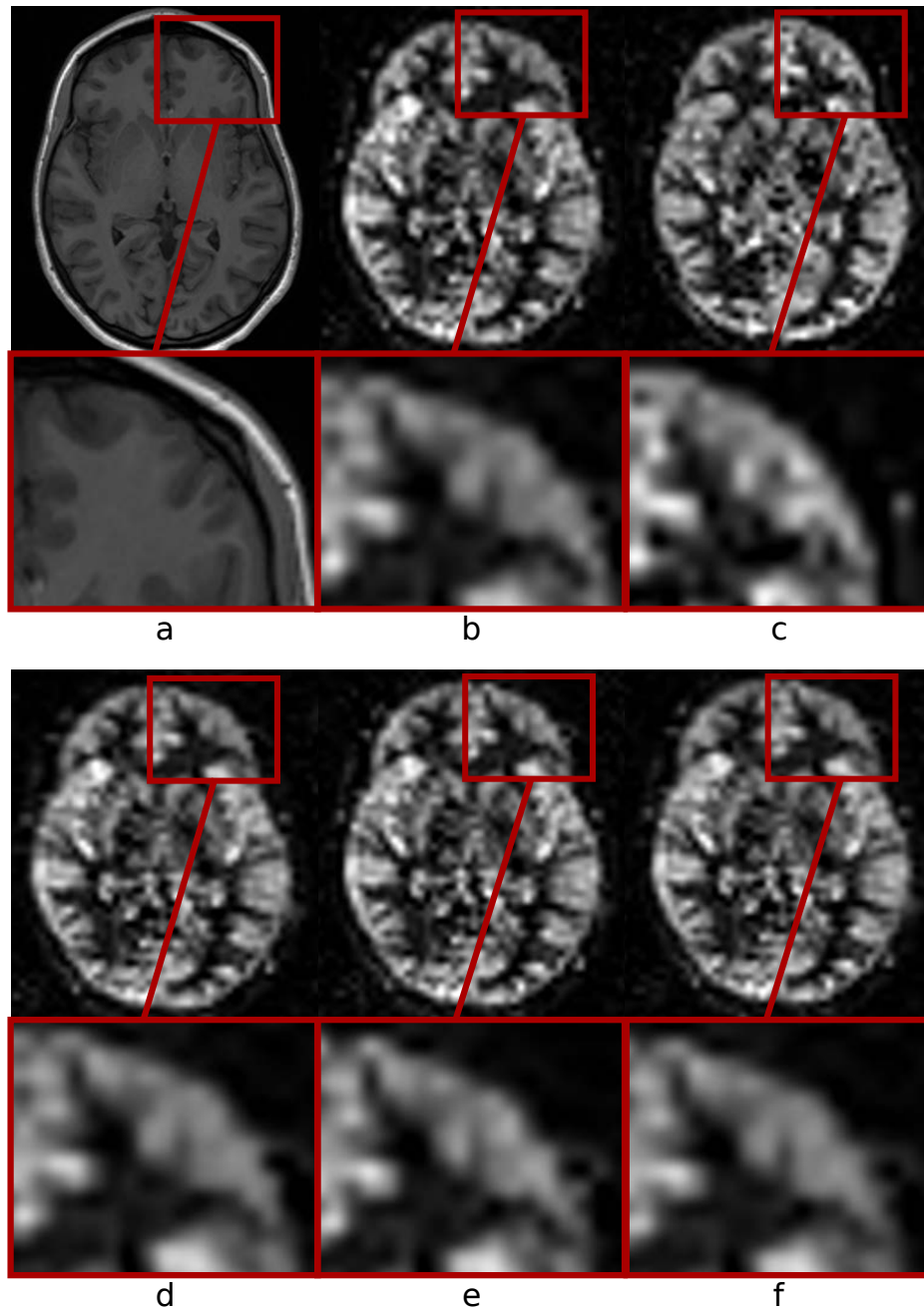


Figure 2: Images d'un sujet sain : a) image structurale, images de signal ASL à partir de b) la série L>>R, c) la série R>>L, d) la série L>>R corrigée avec l'algorithme de Block Matching, e) la série L>>R corrigée avec l'algorithme TOPUP et f) la série L>>R corrigée avec l'algorithme HySCO.

car elle implique le fait que les images BR soient débruitées avant de les reconstruire à une résolution plus élevée.

**Méthode proposée** Nous proposons dans le cadre de cette thèse de coupler débruitage et reconstruction, en imposant une fidélité de l'image reconstruite en terme de valeur moyenne sur la globalité de l'image avec l'image originale, et non une fidélité à l'échelle du voxel, comme c'est le cas dans les méthodes présentées précédemment. Selon nos connaissances, appliquer une telle méthode de super-résolution, guidée par une image structurelle acquise à haute résolution, à des données ASL, constitue l'une des principales contributions de ce travail de thèse.

**Validation** La méthode proposée a été évaluée dans un premier temps sur un jeu de 9 cartes de CBF simulées. Ces cartes ont été construites en affectant des valeurs de CBF aux substances grise et blanche segmentées d'images structurelles (MP2RAGE), avant d'être sous-échantillonnées. Différents niveaux de bruit gaussien, compris entre 3 et 14% de la valeur de CBF affectée à la substance grise, ont été ajoutés à ces images, afin de simuler le bruit pouvant être rencontré dans les cartes de CBF généralement acquises. Ces images basses résolutions ont ensuite été reconstruites à la même résolution que celle des images originales, par application de techniques d'interpolation (plus proche voisin (NN), trinéaire et B-splines d'ordre 3), et la méthode proposée. L'écart entre ces reconstructions et les images d'origine a été évalué par calcul des racines des écarts quadratiques moyens (RMSE).

La méthode a dans un second temps été évaluée sur des données obtenues à partir de 4 volontaires sains (3 femmes, 1 homme,  $34 \pm 6$  ans). Le protocole d'acquisition consistait en une image structurelle (MP2RAGE), une série pCASL de basse résolution ( $3.5 \times 3.5 \times 5$  mm<sup>3</sup>, une série pCASL de haute résolution (HR) ( $1.75 \times 1.75 \times 0.5$  mm<sup>3</sup>), ainsi que deux cartes M<sub>0</sub>, chacune à la résolution de l'une des séries ASL. De la même manière que dans le cas des données simulées, les cartes de CBF obtenues à partir des acquisitions BR ont été reconstruites à l'aide des techniques d'interpolation et de la méthode proposée. La principale limite de cette évaluation réside dans le faible SNR des cartes de CBF issues des acquisitions HR, le fait de pouvoir les considérer comme des cartes de référence auxquelles comparer les images reconstruites pouvant se révéler difficile.

Afin de pallier cette difficulté, la capacité de la méthode proposée à reconstruire des cartes de CBF corrélées avec des images de DSC, technique couramment considérée comme référence en imagerie de la perfusion, a été évaluée dans un troisième temps. Pour ce faire, des données acquises sur 10 patients imagés dans le cadre d'un protocole dédié aux tumeurs cérébrales ont été utilisées. Le protocole d'acquisition comprenait une image structurelle, une séquence PASL (résolution :  $3 \times 3 \times 7$  mm<sup>3</sup>, 0.7 mm d'espacement entre les coupes), et une séquence DSC (résolution :  $1.8 \times 1.8 \times 4$  mm<sup>3</sup>, 1.2 mm d'espacement entre les coupes). Comme précédemment, la performance de la méthode proposée a été comparée à celles obtenues par des techniques d'interpolation, en étant évaluée par mesure de la corrélation entre

ces reconstructions et les images de CBF issues de l'acquisition DSC.

### R.3.1.3 Résultats

**Données simulées** Les images dont les dimensions ont été augmentées par application des techniques d'interpolation apparaissent plus floues que celle obtenue avec la méthode proposée, qui présente plus de détails. Le tableau 2 indique les valeurs de RMSE obtenues pour différents niveaux de bruit initiaux. Ce tableau nous renseigne sur la capacité de la méthode proposée à débruiter les images reconstruites, l'écart entre les images obtenues et les images de référence augmentant moins rapidement que suite à l'application des autres techniques.

Std du bruit	3	6	9	11	14
Plus proche voisin	14.82 ± 0.82*	15.3 ± 0.78*	16.31 ± 0.80*	17.72 ± 0.97*	19.98 ± 1.43*
Trilinear	14.80 ± 0.91*	14.93 ± 0.90*	15.22 ± 0.89*	15.66 ± 0.86*	16.38 ± 0.94*
B-splines	14.01 ± 0.89	14.35 ± 0.86	15.08 ± 0.83*	16.12 ± 0.85*	17.78 ± 1.19*
Méthode proposée	<b>13.92 ± 1.05</b>	<b>14.05 ± 1.04</b>	<b>14.34 ± 1.01</b>	<b>14.79 ± 0.99</b>	<b>15.56 ± 1.08</b>

Table 2: Moyenne et écart-type (std) des 9 RMSE calculées entre les images de référence et les reconstructions obtenues par application des interpolations de type plus proche voisin, trinéaire, B-splines d'ordre 3, ou la méthode proposée, pour des niveaux de bruit croissants. L'écart-type du bruit est exprimé en pourcentage de la valeur de CBF affectée à la substance grise. Les astérisques soulignent des différences significatives avec la méthode proposée..

**Volontaires sains** Les images des sujets sains reconstruites à l'aide de la méthode proposée présentent elles aussi plus de détails que celles obtenues par application des techniques d'interpolation (figure 3). La méthode proposée est également associée à des valeurs de RMSE inférieures à celles obtenues avec les autres techniques pour trois des quatre sujets.

**Comparaison avec la DSC** Les corrélations calculées entre les images reconstruites et les cartes de CBF issues des acquisitions DSC sont significativement plus élevées dans le cas de l'application de la méthode proposée que par interpolations trinéaire ou B-splines ( $p < 10^{-4}$ ).

### R.3.1.4 Comparaison avec les méthodes de correction des volumes partiels

**Méthode** La méthode proposée et évaluée dans les paragraphes précédents permet d'augmenter la résolution de cartes de CBF issues de séries ASL en en augmentant le niveau de détails. De telles propriétés peuvent amener à penser que cette méthode réduise l'influence des PVE. La méthode de super-résolution est donc ici comparée à

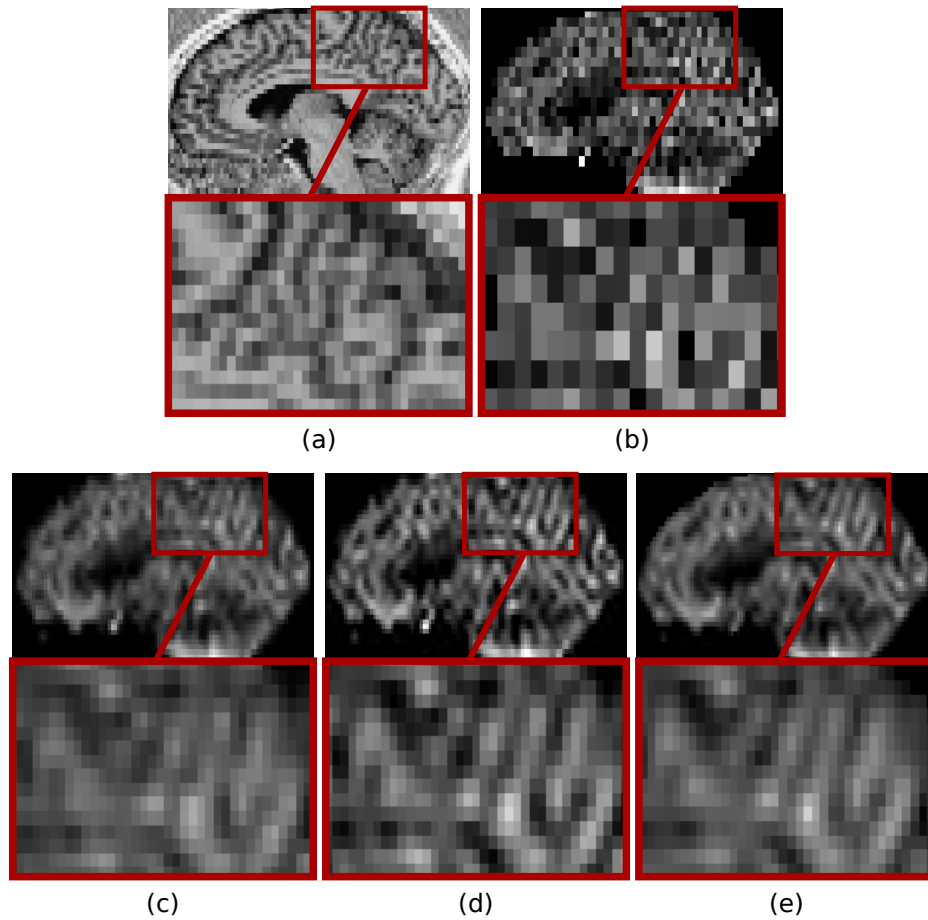


Figure 3: Sujet sain : coupes sagittales de a) l'image structurale, b) la carte de CBF issue de la série pCASL acquise à basse résolution, c) la carte reconstruite par interpolation trilinéaire, d) par application de B-splines d'ordre 3, et e) l'image obtenue à l'aide de la méthode proposée.

la méthode de correction de PVE par régression linéaire proposée par [Asllani 2008], qui est elle appliquée aux images dans leur résolution d'origine, sur un jeu de données simulées. Les 9 images structurales utilisées afin de constituer les données simulées rencontrées dans les sections R.3.1.2 et R.3.1.3 ont ainsi permis de construire, après segmentation et seuillage, des cartes de signal ASL dans lesquelles les proportions de substances grise et blanche sont connues. Des variations sinusoïdales ont été introduites dans ces images, afin d'évaluer la capacité des deux méthodes à conserver de telles variations. Les valeurs de RMSE ont été calculées entre les images corrigées et les références à des fins d'évaluation quantitative.

**Résultats** Les valeurs de RMSE mesurées montrent que la méthode proposée permet de réduire l'influence des PVE. Les images obtenues soulignent quant à elles la supériorité de la méthode proposée en ce qui concerne sa faculté à conserver et

retrouver les variations spatiales introduites dans les images de référence, celles-ci se retrouvant lissées par application de la méthode de régression linéaire.

### **R.3.1.5 Conclusion**

Une méthode de super-résolution adaptée aux images ASL a été proposée et évaluée sur des données simulées, des données acquises sur des volontaires sains, ainsi que des images de patients imagés pour cause de suspicion de présence de tumeurs cérébrales. Cette méthode s'est révélée générer des images plus proches des références dans chacun des cas, en comparaison avec des techniques d'interpolation. La capacité de cette méthode à réduire l'influence des PVE a également pu être mise en évidence.

## **R.3.2 Super-résolution adaptée aux acquisitions d'ASL multi-TI**

### **R.3.2.1 Introduction**

Cette section présente une adaptation de la méthode présentée en [R.3.1](#) au cas d'acquisitions ASL multi-TI. Cette adaptation, qui reste basée sur l'évaluation de similarités entre propriétés de voxels voisins, diffère de la précédente de par le fait que la reconstruction à une dimension supérieure intervient au niveau de la série de cartes de signal ASL associées aux différents PLD.

### **R.3.2.2 Matériel et méthodes**

Dans le cadre de cette nouvelle méthode, les similarités sont évaluées entre les évolutions temporelles des voxels dans la série de cartes de signal ASL, la comparaison de patches entre voxels voisins dans une image structurelle acquise à haute résolution étant quant à elle conservée. Cette adaptation a pour objectif de corriger les valeurs des voxels des cartes de signal ASL qui pourraient présenter des valeurs aberrantes, ou faire dévier l'évolution temporelle du signal d'un voxel de celle de voxels présentant des propriétés similaires. Cet ajustement du signal temporel est supposé permettre une estimation plus fiable des paramètres que sont le CBF et l'ATT.

Cette méthode a tout d'abord été évaluée sur des données simulées. Une série de cartes de signal ASL théoriques correspondant à l'évolution du modèle standard de Buxton a été générée à partir d'une carte de CBF et d'une carte d'ATT. 20 séries sous-échantillonnées et bruitées ont été produites à partir de cette série initiale, puis reconstruites à la résolution d'origine à l'aide de différentes méthodes. La méthode proposée dans cette section (SR4D) a en effet été comparée à une interpolation par B-splines d'ordre 3 et la méthode de la section précédente (SR3D) appliquées aux cartes de CBF et ATT estimées à partir de chacune des séries de signal ASL, ou en augmentant la résolution de chacune des cartes de signal ASL séparément à l'aide de la méthode de la section précédente (SR3D MULTI), puis en estimant les CBF et ATT. Les cartes ainsi estimées ont été comparées aux cartes originales par mesure du rapport signal à bruit maximal (PSNR).



Des images acquises sur 8 sujets sains (6 femmes, 2 hommes,  $33 \pm 9$  ans), consistant en une image structurale (MP2RAGE), deux séquences prototype pCASL multi-TI (12 PLD compris entre 500 ms et 4240 ms) et 2 cartes  $M_0$ , chacune acquise à basse et haute résolution, ont également été utilisées afin de valider cette méthode. Les estimations des cartes CBF et ATT de basse résolution ont été reconstruites à la haute résolution par application des quatre méthodes présentées dans le cas des données simulées. À partir des cartes CBF et ATT ainsi obtenues, l'évolution théorique qu'aurait dû suivre le signal ASL a été modélisé en suivant le modèle standard de Buxton. Les évolutions de signal ASL obtenues dans les différentes séries (acquisitions BR, HR, et reconstruites à l'aide de SR3D MULTI ou SR4D), ont ensuite été comparées à cette évolution théorique, par calcul de la corrélation entre leurs courbes et les évolutions simulées, suivant l'hypothèse que plus cette corrélation est élevée, plus les estimations de CBF et ATT obtenues sont fiables.

### R.3.2.3 Résultats

Sur les données simulées, la méthode proposée, SR4D, permet des estimations de CBF et ATT associées à un PSNR significativement plus élevé que dans le cas des autres méthodes évaluées ( $p < 10^{-22}$ ), par comparaison avec les images de référence. La capacité de SR4D à reconstruire des séries de cartes de perfusion à haute résolution dont les voxels suivent une évolution temporelle plus proche de celle de la série de référence a également pu être soulignée.

Les évolutions temporelles obtenues par reconstruction des données acquises sur sujets sains sont quant à elles associées à une augmentation de leur corrélation avec les évolutions théoriques. À noter notamment une augmentation significative du nombre de voxels pour lesquels cette corrélation devient supérieure à 0.5 ( $p < 10^{-4}$ ). Visuellement, les estimations de CBF obtenues à partir des séries reconstruites à l'aide de SR4D présentent plus de détails et sont moins lissées que par application de SR3D (figure 4). Ces cartes présentent également moins de valeurs aberrantes que celles obtenues en utilisant SR3D MULTI. Les cartes d'ATT se révèlent également être bien débruitées suite à l'application de SR4D (figure 5).

### R.3.2.4 Conclusion

Cette méthode de super-résolution adaptée aux acquisitions ASL multi-TI, évaluée sur des données simulées et acquises sur sujets sains, a montré sa capacité à produire des estimations fiables, à haute résolution, de CBF et ATT.

## R.4 Discussion et perspectives

La séquence adoptée suite au travail de standardisation des acquisitions ASL a permis l'acquisition des images de perfusion de 184 sujets, dans le cadre d'une étude de grande ampleur qui s'intéresse aux relations entre facteurs de risques vasculaires

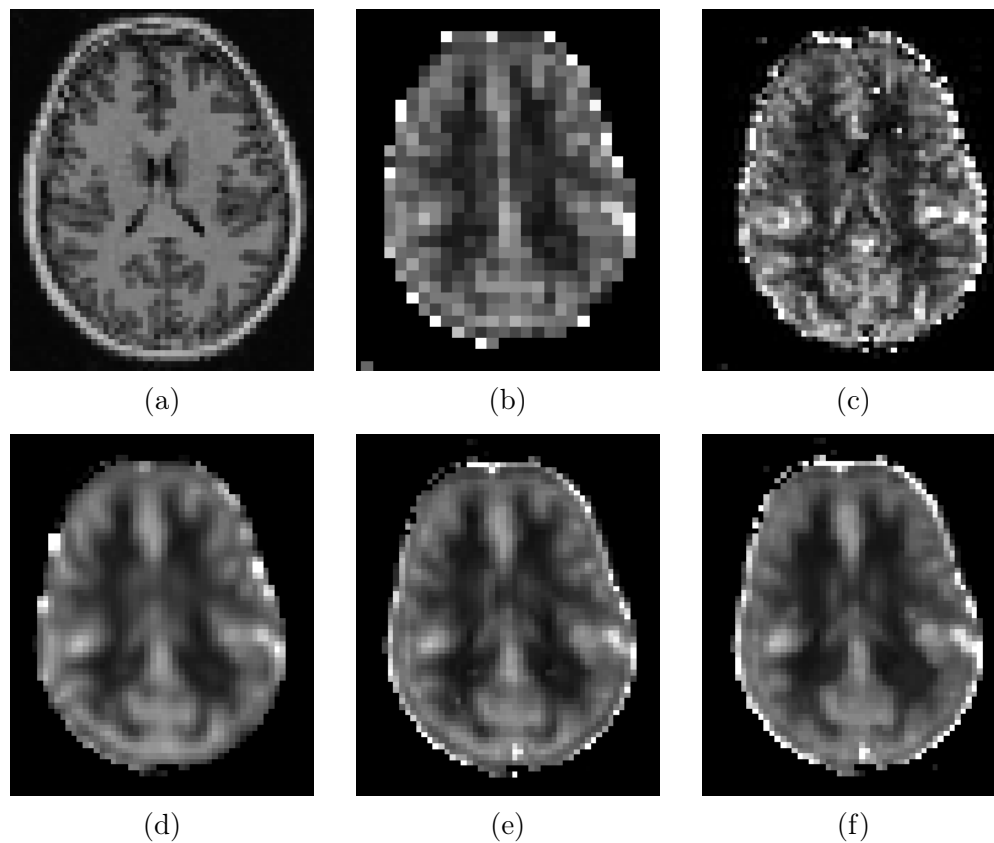


Figure 4: Sujet sain: coupes axiales d'une image structurale (a), de la carte de CBF de basse résolution (b) associée, de celle de haute résolution (c), celle reconstruite avec SR3D (d), et des estimations de CBF obtenues suite aux applications de SR3D MULTI (e) et SR4D (f).

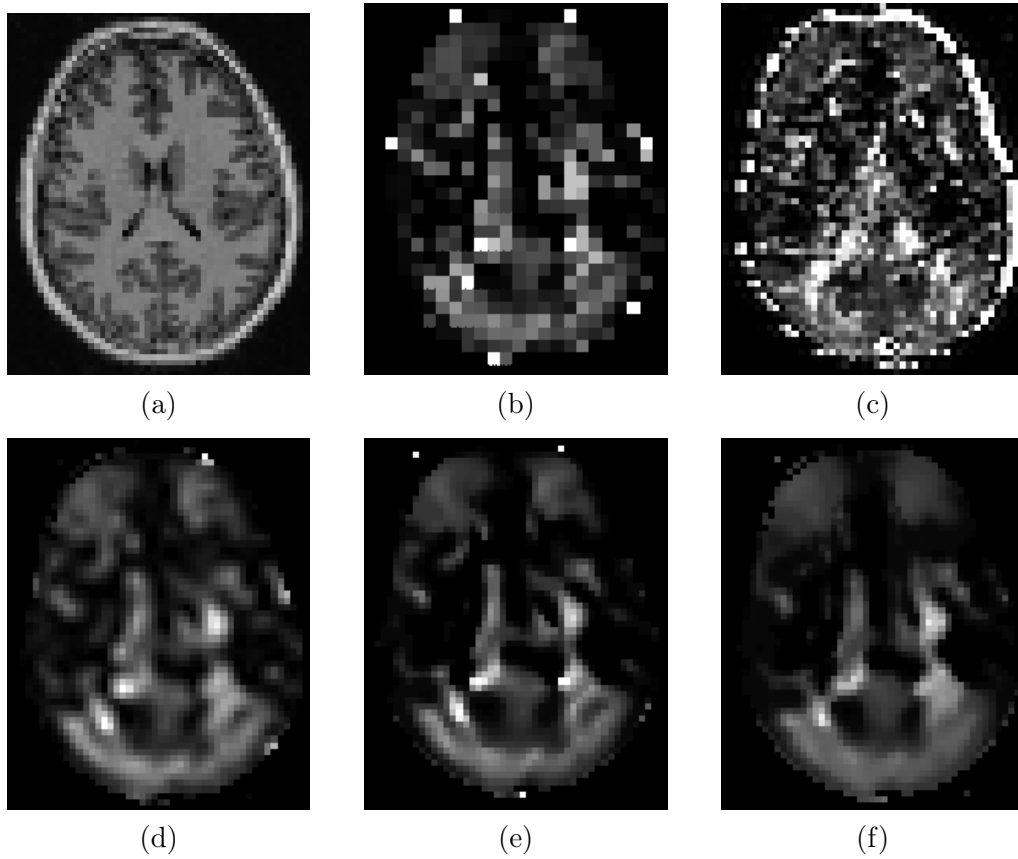


Figure 5: Sujet sain: coupes axiales d'une image structurale (a), de la carte d'ATT de basse résolution (b) associée, de celle de haute résolution (c), celle reconstruite avec SR3D (d), et des estimations d'ATT obtenues suite aux applications de SR3D MULTI (e) et SR4D (f).

et démences. L'outil développé afin d'évaluer la qualité des images ASL a quant à lui permis aux attachés de recherche clinique du CATI d'analyser ces images.

Les méthodes de super-résolutions développées dans le cadre de cette thèse ont montré permettre une augmentation du niveau de détails dans les images ASL. Une première méthode a été proposée afin de reconstruire les cartes de CBF à des résolutions supérieures à celles dans lesquelles les données ASL ont été acquises. Une extension de cette méthode dans le but de l'adapter au cas d'acquisitions de type multi-TI a quant à elle montré sa capacité à générer des estimations fiables, à haute résolution, de CBF et ATT. Ces techniques ont été évaluées sur des données simulées, de sujets sains, ou de patients imagés dans le contexte d'un protocole dédié à l'étude de tumeurs cérébrales. Des applications intéressantes dans le cadre de travaux futurs pourraient être le cas de patients diagnostiqués avec des formes précoces de démences, associées à des anomalies perfusionnelles pas encore liées à des anomalies visibles sur des images structurales.

Par ailleurs, évaluer l'influence de l'application de méthodes de correction des distorsions avant d'utiliser l'un des algorithmes de super-résolution pourrait être réalisé dans le cadre de travaux futurs.



## Part I

# Context and objectives



# Brain perfusion: a general presentation

---

## Contents

---

<b>1.1</b>	<b>Introduction</b>	<b>4</b>
<b>1.2</b>	<b>General presentation of the human brain</b>	<b>4</b>
<b>1.3</b>	<b>Brain perfusion</b>	<b>5</b>
1.3.1	Blood supply	5
1.3.2	Parameters	6
1.3.3	Applications	6
<b>1.4</b>	<b>Perfusion imaging techniques</b>	<b>11</b>
1.4.1	Positron Emission Tomography	11
1.4.2	Single Photon Emission Computed Tomography	11
1.4.3	Computed Tomography	12
1.4.4	Dynamic Susceptibility Contrast	12
1.4.5	Arterial Spin labelling	13

---



## 1.1 Introduction

The brain, part of the central nervous system, counts for around 3 % of a human's total weight, while representing 20% of its oxygen and 15% of its total glucose consumption. It had long been held to be an insignificant organ, as proven by the fact that the heart and other organs were well conserved in Egyptian mummies, while the brain was removed from them. For the Greek philosopher and scientist Aristotle, the brain served as a blood conditioner, while Descartes saw it as an antenna allowing the spirit and body to communicate.

Until the last century, most of the knowledge gained from brain structure and function were obtained by means of experimentations and accidents involving living people presenting unusual functions or behaviors related to brain injuries. Scientists usually had to wait for their patients to die before being able to relate lesions and pathological findings.

Nowadays, accumulated knowledge and spectacular technological improvements, such as the development of electroencephalography or different imaging modalities, at microscopic as well as mesoscopic scales, provide information about the role and function of the brain in healthy subjects, but also concerning a number of pathologies. Nonetheless, work is still needed to understand the brain itself, and its relation with its environment.

In the context of this thesis, we focus on arterial spin labelling (ASL), a magnetic resonance (MR) imaging modality that allows to obtain information about brain perfusion. This chapter will first provide a general presentation of the brain, before focusing on the biological process of brain perfusion, describing parameters that are related to this perfusion, and finally introducing imaging techniques in use to obtain perfusion information.

## 1.2 General presentation of the human brain

The brain can be divided into different regions, related to specific functions. Some of them constitute the four external lobes:

- The frontal lobe, hosting the primary motor cortex, involved in the control of voluntary movements. It is also associated with planning and language related tasks.
- The temporal lobe, that contains the limbic system, related to the treatment of emotions. It is also involved in auditory and visual processing.
- The parietal lobe, that integrates information from the different sensorial modalities, and plays also a role in space perception and attention.
- The occipital lobe, mostly dedicated to the processing of visual signals.

Each lobe contains a number of gyri and sulci, forming folds that allow to increase the brain surface (figure 1.1).

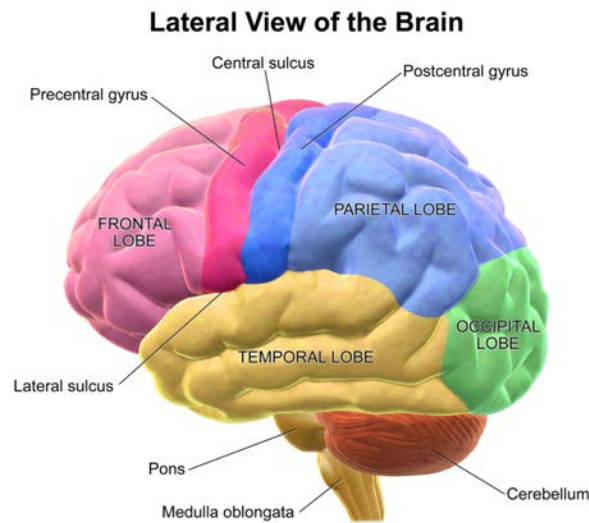


Figure 1.1: Representation of the brain lobes and some sulci and gyri. Image courtesy: [https://en.wikipedia.org/wiki/Lobes\\_of\\_the\\_brain](https://en.wikipedia.org/wiki/Lobes_of_the_brain)

The brain consists in an organization of neurons and glial cells, with a population of some 100 billions of each. The cell bodies of the neurons are mostly located at the periphery of the brain or in particular locations, and form the gray matter. The white matter consists in the neuron's axons, carrying information. These cells are supplied with nutrients by blood through brain perfusion, described in more details in the following section.

## 1.3 Brain perfusion

### 1.3.1 Blood supply

Brain perfusion is the biological process allowing the delivery of oxygen and nutrients to brain tissues. It mostly occurs by means of the microcirculation, which corresponds to blood flowing through the capillaries.

Capillaries are the smallest vessels within the brain blood supply system. The heart provides oxygen to the brain by means of four arteries, consisting of two internal carotids, supplying the anterior brain, and two vertebral arteries, supplying the brainstem and posterior brain. These arteries join the circle of Willis, regulating blood supply, notably to reduce the influence of heart pulsations on brain perfusion. Six vessels emerge from the circle of Willis, each hemisphere of the brain being supplied by an anterior, a middle and a posterior arteries. The anterior cerebral arteries deliver blood to the medial part of the frontal and parietal lobes. The posterior cerebral arteries supply medial posterior parts of the temporal and occipital lobes. The middle cerebral arteries supply the remaining parts of the frontal, temporal, parietal

and occipital lobes. The arteries are extended by arterioles, themselves branching into capillaries. After nutrients consumption, blood flows through venules, that converge into venous sinuses. These sinuses converge progressively into the two main veins flowing out of the brain, the internal jugular veins. Figures 1.2 and 1.3 provide a schematic representation of this brain vasculature.

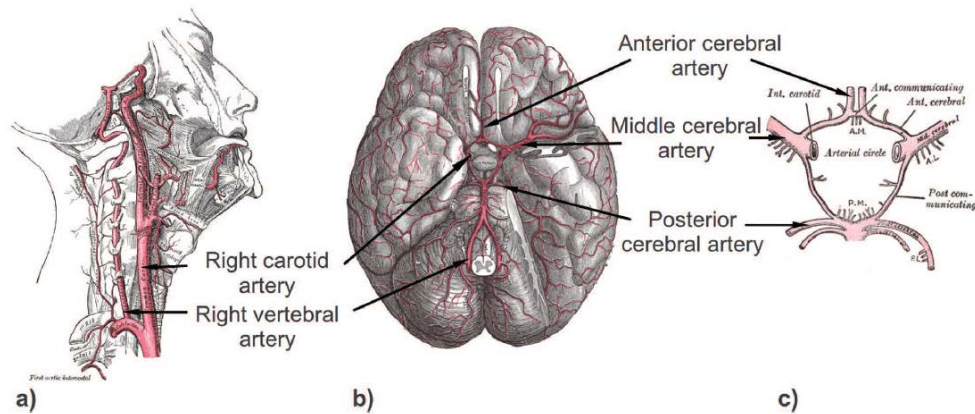


Figure 1.2: Representation of a) the carotids and vertebral arteries, b) an axial view of arteries ramifications at the basis of the brain and c) the circle of Willis. Image courtesy: [Gray 1918]

### 1.3.2 Parameters

Some parameters allow to quantify the brain perfusion process. The cerebral blood flow (CBF), usually expressed in the unit of millilitre per minute per a hundred grams of brain tissue ( $\text{ml}\cdot\text{min}^{-1}\cdot 100\text{g}^{-1}$ ) is one of the most commonly utilized parameters. Expressed in millilitre of blood per a hundred grams of tissue ( $\text{ml}\cdot 100\text{g}^{-1}$ ) is also the cerebral blood volume (CBV). Because evaluating the celerity of the brain blood flow has also a potential therapeutic value, the bolus arrival time (BAT, only obtained by means of bolus related imaging techniques), the arterial transit time (ATT) or the tissue transit time (TTT), expressed in seconds or milliseconds, can be of interest. The time to peak (TTP), measuring the time needed to obtain the maximal bolus signal, expressed in seconds or milliseconds, can also be evaluated.

### 1.3.3 Applications

Perfusion imaging can provide useful information to establish diagnosis, to follow the evolution of pathologies or to characterize the state of a disease. While usually not sufficient as a single modality, and completing a need for other diagnostic information, perfusion can be of great interest in different kinds of pathologies.

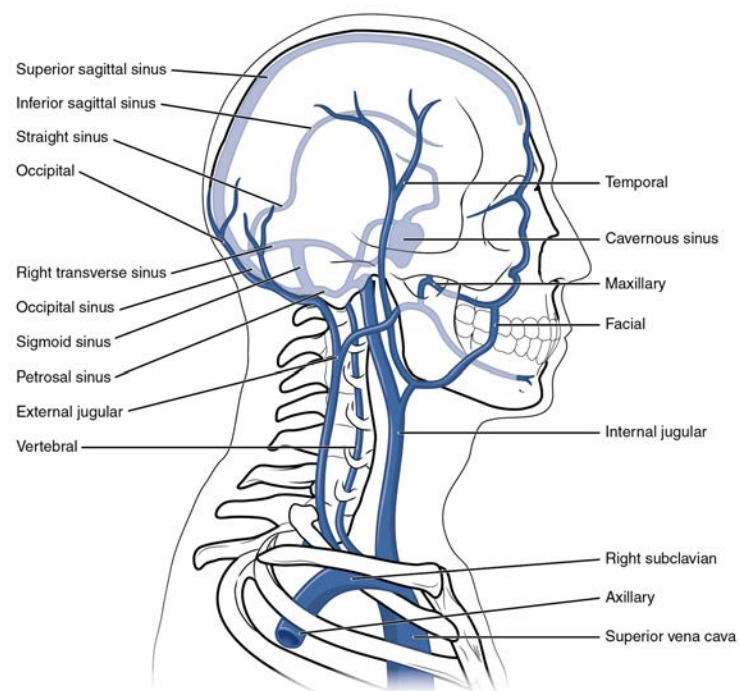


Figure 1.3: Image representing the head and neck most important veins. Image courtesy: [College 2014]

### 1.3.3.1 Cerebrovascular disease

Perfusion imaging is of particular interest in the case of pathologies affecting brain blood vessels. As a matter of fact, it has been shown in a number of studies that abnormal perfusion patterns can be the causes or consequences of vascular related disease, such as malformed, occluded or damaged blood vessels [Grade 2015, Hendrikse 2004, Kimura 2005, Bokkers 2009, Yun 2012]. Figure 1.4 shows an example of images acquired in the case of an occlusion, that implies an hypo-perfusion, visible on arterial spin labelling images.

Perfusion imaging techniques providing information about both CBF and ATT are to be preferred. Indeed, detecting an ASL signal reduction in a brain region, associated with an ATT increase in the same region can for example imply a stenosis, blood following a new pathway to reach the brain tissues.

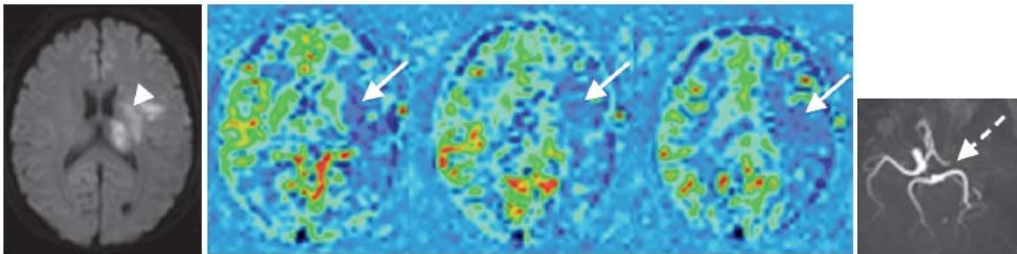


Figure 1.4: From left to right: MR diffusion image presenting an hyper-signal in the middle cerebral territory, associated with an hypo-perfusion on 3 axial slices of an ASL perfusion image, and to an occlusion of the middle cerebral artery on the MR angiography. Image courtesy: [Esquevin 2013]

### 1.3.3.2 Oncology

Brain perfusion images provide useful information in the case of brain tumours. Indeed, it can be used as a help for establishing diagnosis, for grading and for following the evolution of tumours [Grade 2015]. These possibilities are linked to the fact that tumours are subject to an angiogenesis, meaning a vascular proliferation around the tumour, while evolving from low to high grade [Warmuth 2003, Weber 2006]. Assessing perfusion in tumours areas can therefore be of interest in order to adapt treatment. Figure 1.5 provides an example of a tumour appearing under the form of an hyper-perfused area on CBF maps obtained with ASL.

### 1.3.3.3 Dementia

The study of dementia related disease conducted to the adoption of perfusion imaging techniques in imaging protocols, as a matter of diagnosis help. Indeed, brain

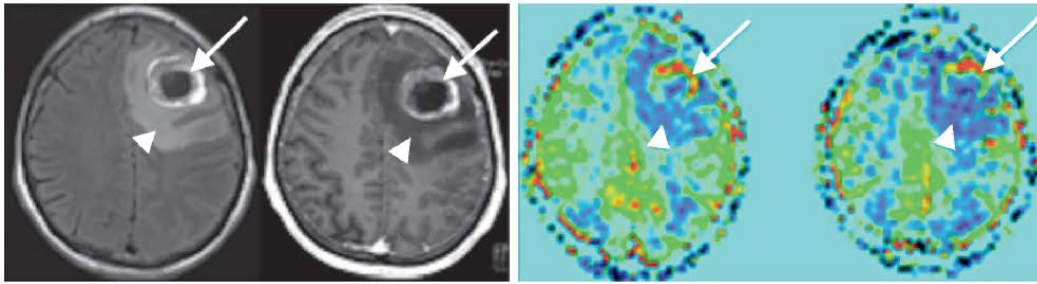


Figure 1.5: From left to right: FLAIR, post-gadolinium  $T_1$ -weighted, and CBF images obtained with ASL of a subject diagnosed with a brain tumour. The tumour appears as hyper-perfused on the CBF maps. Image courtesy: [Esquevin 2013]

regions presenting altered metabolism and perfusion, such as in figure 1.6, have been shown to correspond to areas of brain structure changes, especially in the case of Alzheimer disease (AD) [Chen 2011, Musiek 2012]. As an example, patients diagnosed with both AD and mild cognitive impairment, the early stage of Alzheimer disease presented hypo-perfusion and a reduced metabolism activity, notably in the precuneus and the posterior cingulate cortex, as well as in the frontal and parietal lobes [Yoshiura 2009, Mak 2012].

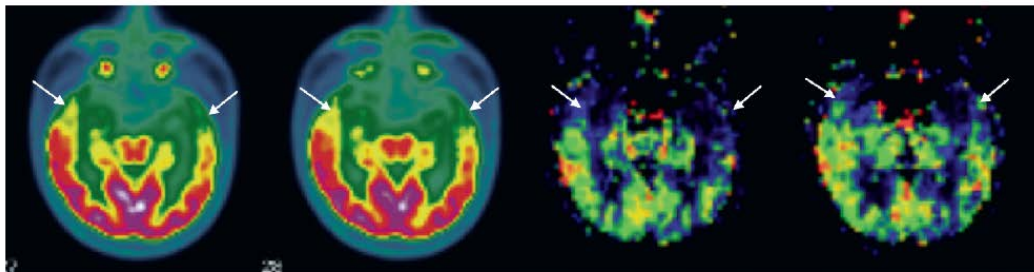


Figure 1.6: From left to right: FDG-PET and ASL CBF maps. Left predominant bitemporal anterior hypo-perfusion can be observed on the CBF maps, in agreement with hypo-metabolisms visible on the PET scans. Image courtesy: [Esquevin 2013]

#### 1.3.3.4 Psychiatric disease

Differences and abnormal perfusion patterns have been highlighted between patients and healthy subjects regarding some psychiatric disease. Different categories of depression (chronic, treatment-resistant, adolescents or late life depressions) present different hypo or hyper-perfused areas [Duhameau 2010, Ho 2013, Colloby 2012].

Schizophrenia and borderline personality also showed to be related with characteristic perfusion patterns [Kindler 2013, Wolf 2012]. Studies have also concluded to the possibility of predicting patients' responses to treatments, conducting to therapy adaptation and personalisation [Weiduschat 2013, Homan 2012].

### 1.3.3.5 Epilepsy

Assessing perfusion in epileptic patients can be useful in order to locate the epileptogenic zone. Indeed, such regions have been shown to present hypo-perfusion between seizures and hyper-perfusion during seizures, which can be assessed by locating brain perfusion asymmetries with the contralateral hemisphere [Duncan 2010]. Images acquired on a patient diagnosed with a form of epilepsy are presented in figure 1.7.

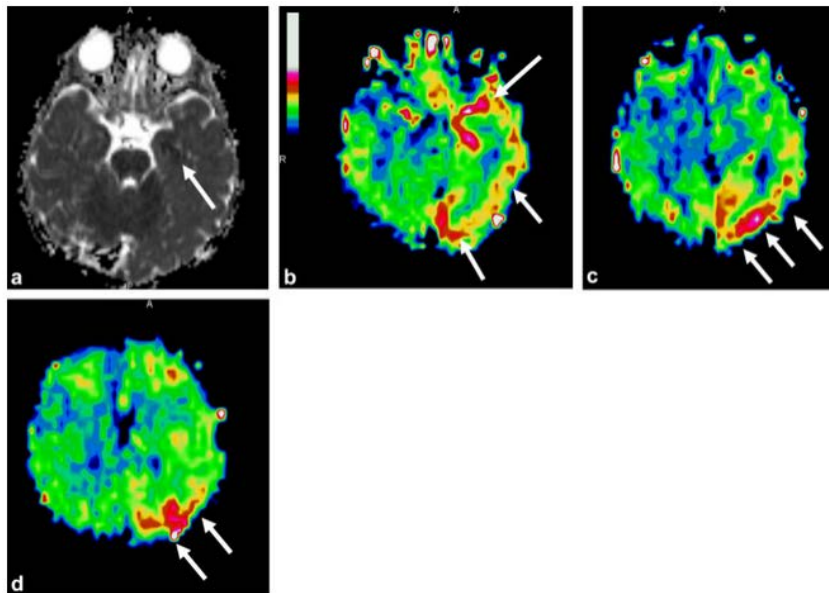


Figure 1.7: 14-month-old boy presenting with fever, right unilateral clonic seizures and ipsilateral hemiplegia that lasted for more than 1 hour. Postictal EEG showed slow focal and persistent left cerebral hemisphere activity 24 hours after the seizure. MRI performed during the postictal state shows no abnormality on conventional imaging. a) Apparent diffusion coefficient map reveals restricted focal left hippocampal diffusion (arrow). (b-d) ASL CBF map reveals a larger abnormal area of hyper-perfusion in the left temporal and parieto-occipital lobes (arrows). Image courtesy: [Proisy 2016]

The pathologies presented in this section are associated with different abnormal perfusion patterns. Various imaging modalities, described in the next section, have been developed in order to obtain useful information about brain perfusion.

## 1.4 Perfusion imaging techniques

Different imaging techniques allow to obtain maps of brain perfusion parameters and hemodynamic information. Most of them provide quantification of CBF and CBV, but differ in the type of tracers in use (endogenous or exogenous), necessary equipment (more or less expensive and space requiring), scan duration, or spatial and temporal resolution. Therefore, each of these techniques has advantages and disadvantages, making it adapted to certain kinds of populations and pathologies [Wintermark 2005].

### 1.4.1 Positron Emission Tomography

Positron Emission Tomography (PET) is a nuclear imaging technique, considered as a reference perfusion imaging method. The injection or inhalation of a radioactive tracer is required. Quantitative information concerning CBF, CBV, and the metabolic activity of tissues can be obtained. Indeed, depending on the tracer in use, the regional oxygen extraction fraction (rOEF) and the regional cerebral metabolic rate of oxygen or glucose ( $rCMRO_2 / rCMRO_{glu}$ ) can be evaluated. The radioactive tracers, having short half-lives, are emitting positrons, that annihilate with electrons present in their environment. This annihilation generates two photons sent in opposite directions, which are detected by sensors. The rate of detected photons can be evaluated, providing quantitative estimations of perfusion parameters by application of quantification models, often based on the indicator dilution theory [Kety 1948, Phelps 1979].

PET is most commonly used by injecting  $^{18}F$  fluorodeoxyglucose, a molecule close to glucose. This molecule accumulates in cells metabolising glucose, allowing evaluations of cancerous cells and regions presenting a reduced metabolism. Inhalations of  $^{15}O$  can also be prescribed in order to assess CBV,  $rCMRO_2$  and rOEF.

PET scans have a duration of 5 to 9 minutes, and a spatial resolution ranging from 4 to 6 mm.

### 1.4.2 Single Photon Emission Computed Tomography

Single photon emission computed tomography (SPECT) is similar to PET in the sense that it is based on radioactive tracers, one of the main differences being that SPECT tracers release photons corresponding to gamma emissions. The emitted particles are received and angularly selected by a collimator, tomographic reconstruction enabling 2D and 3D tracer distribution assessment [Prince 2005].  $^{133}Xe$  is the tracer that is historically used in SPECT perfusion imaging, although other tracers can be preferred, that allow reduced scattering [Wintermark 2005]. HmPAO (hexa-methyl-propyl-amineoxime) is particularly well suited to the brain, because of its disposition to target regions subject to an important cerebral activity.

While  $^{133}Xe$  allows to obtain quantitative CBF values, correction methods should be applied to maps obtained by means of other tracers [Kety 1948, Lassen 1988]. SPECT tracers can be injected before scanning, one of the main



advantages being to enable image acquisition during seizures in the case of epileptic patients. The detection of brain regions presenting a reduced activity, and thus reduced CBF, can also be performed on SPECT images, for dementia or Alzheimer disease for example.

SPECT scans have a duration of 10 to 15 minutes, and allow image acquisition at spatial resolutions from 4 to 6 mm.

### 1.4.3 Computed Tomography

Computed tomography (CT) perfusion imaging can be separated in two different sub-techniques. The first one is based on stable Xenon inhalations (XeCT), rapidly entering the brain by crossing the blood-brain barrier. Xenon is in this case used as a contrast agent, modifying the attenuation of the X-rays between the source and the detector [Wintermark 2005, Prince 2005]. CBF can be estimated by means of the Kety-Schmidt equation [Kety 1948], making this imaging method interesting in cases of cerebrovascular abnormalities.

The other CT perfusion imaging method, referred to as perfusion CT (PCT), relates on an iodinated contrast agent injection, followed by a continuous scanning during 40 to 45 seconds. This continuous scan allows to image the arrival of the first bolus of the contrast agent, and to estimate CBF, CBV and MTT. This method is also utilized for patients presenting vascular disorders, or as a prognostic factor in cases of brain injuries [Wintermark 2005].

Computed tomography perfusion imaging does not allow whole brain coverage, and is prescribed to children only after a careful evaluation of its potential benefit. XeCT can reach resolutions close to 4 mm, whereas PCT allows resolutions in the range of 1-2 mm.

### 1.4.4 Dynamic Susceptibility Contrast

Dynamic susceptibility contrast (DSC) is a magnetic resonance (MR) imaging technique, similar to CT perfusion imaging in the sense that its objective is to obtain information about the arrival of a bolus of tracer entering the brain capillary bed. This measurement is performed by recording the  $T_2$  or  $T_2^*$  decrease induced by a contrast agent, usually gadolinium chelates. DSC images can be acquired using gradient echo (GRE) or spin echo (SE) sequences, while GRE sequences are usually preferred because of higher signal and less contrast agent requirement [Speck 2000]. CBF, CBV, TTP and MTT can be estimated by means of DSC acquisitions [Østergaard 1996, Kiselev 2001].

Spatial resolutions close to  $2 \times 2 \times 4$  mm can be achieved with DSC, that is well suited for cerebrovascular disease examination. Combined with diffusion weighted images (DWI) and spectroscopy, this method is also useful in tumour evaluation, and in stroke assessment, joint to DWI and MR angiography [Wintermark 2005].

### 1.4.5 Arterial Spin labelling

Arterial spin labelling (ASL) is an other MR perfusion imaging technique, based on the use of endogenous tracers. Hydrogen atoms of circulating blood water molecules are magnetically labelled and allow to acquire perfusion images, that can provide information about CBF and ATT depending on the choice of single or multiple imaging time sequences [Detre 1992, Günther 2001, MacIntosh 2010]. While usually supposed equal to ATT in common ASL parameters estimations, TTT can also be assessed by means of specific sequences making the ASL signal sensitive to different compartments  $T_2$  relaxation times [Wells 2009, Liu 2010].

Because of the fact that ASL does not require the use of exogeneous tracers, it is of particular interest for children or vulnerable patients imaging. Scan duration is approximately equal to 4 minutes, and resolutions close to 3 mm can be achieved. While not included in a majority of clinical routine imaging protocols, ASL is of increasing interest in research investigations, concerning most of the pathologies presented in 1.3.3. ASL, which is the MR perfusion imaging sequence providing the images that are at the center of the present work, will be described in more details in chapter 2.



# Arterial Spin labelling

---

## Contents

<b>2.1</b>	<b>Introduction</b>	<b>16</b>
<b>2.2</b>	<b>Basic principle</b>	<b>16</b>
<b>2.3</b>	<b>Labelling approaches</b>	<b>16</b>
2.3.1	Continuous ASL	16
2.3.2	Pulsed ASL	18
2.3.3	Pseudo-continuous ASL	19
2.3.4	Vessel encoded pCASL	19
<b>2.4</b>	<b>Acquisition parameters</b>	<b>20</b>
2.4.1	Labelling duration and post-labelling delay	20
2.4.2	Single-TI and multi-TI acquisitions	20
2.4.3	Background suppression	21
2.4.4	Readout approaches	21
2.4.5	Vascular flow crushing gradients	23
<b>2.5</b>	<b>ASL signal models</b>	<b>23</b>
2.5.1	General kinetic model	23
2.5.2	Standard kinetic model	24
2.5.3	Two compartment model	26
<b>2.6</b>	<b>Processing pipelines</b>	<b>27</b>
2.6.1	Single-TI ASL image processing pipeline	27
2.6.2	Multi-TI image processing pipeline	28
<b>2.7</b>	<b>Thesis objectives</b>	<b>31</b>

---

## 2.1 Introduction

Arterial spin labelling (ASL) is a non-invasive magnetic resonance perfusion imaging technique, that was first proposed to assess rat brain perfusion [Detre 1992]. This technique was rapidly adapted to human brain imaging, and is now currently used in research studies that aim to evaluate perfusion patterns related to different pathologies. In this chapter, we present the basic principle of ASL data acquisitions, as well as aspects that contribute to the quality and the reliability of ASL images. The main perfusion quantification models are then presented, followed by a description of the image processing pipelines developed in the context of this thesis.

## 2.2 Basic principle

Figure 2.1 provides a schematic description of the basic principle of ASL images acquisition. In order to create the endogenous tracers required to generate an ASL signal, radio-frequency pulses are applied. An image, called labelled image, is then acquired. The difference between this labelled image and a control image, acquired without the labelling step, corresponds to a map in which voxel intensities are proportional to CBF. Because signal differences due to labelled blood water account for at most 5% of the raw ASL image intensity, the signal-to-noise ratio (SNR) of a single control-label subtraction is usually low. In order to increase this SNR, multiple image pairs are acquired, leading to acquisitions of ASL series of interleaved control and label images.

Since the first ASL sequence implementation, a large number of improvements have been proposed, particularly regarding the labelling approaches.

## 2.3 Labelling approaches

The three main labelling approaches encountered in the literature and described in this section are the continuous, pulsed and pseudo-continuous labelling schemes. Vessel encoded ASL can also be of interest in the case of certain pathologies.

### 2.3.1 Continuous ASL

In continuous ASL (CASL), the magnetization of blood water protons is inverted as blood flows through a single labelling plane [Detre 1992, Williams 1992]. This inversion occurs in a continuous way, which means that RF energy is applied continuously during 1 to 3 seconds. Figure 2.2 illustrates this process. The main advantage of this labelling technique is its impact on image signal-to-noise ratio (SNR), while drawbacks are related to the poor labelling efficiency and the necessary energy quantity, implying the use of dedicated hardware [Alsop 2015]. For these reasons, other labelling methods have been preferred since the late 1990s.

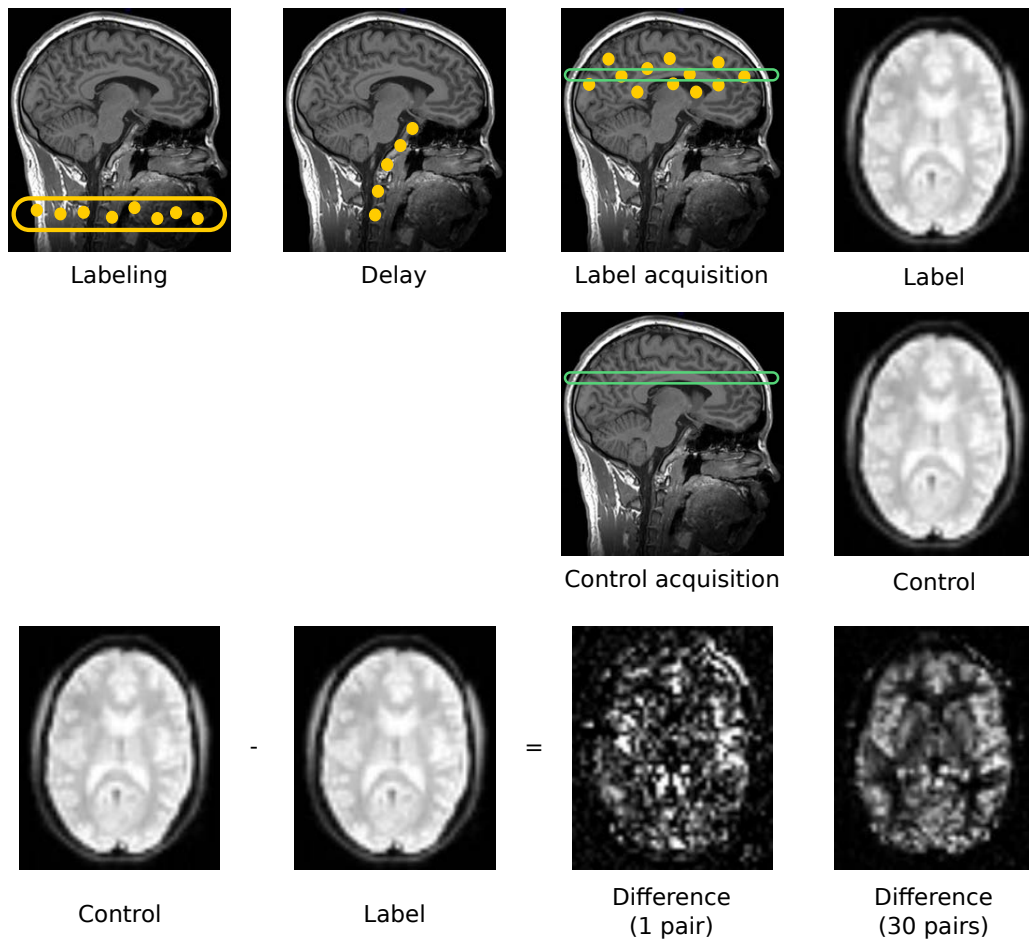


Figure 2.1: Principle of ASL image acquisitions.

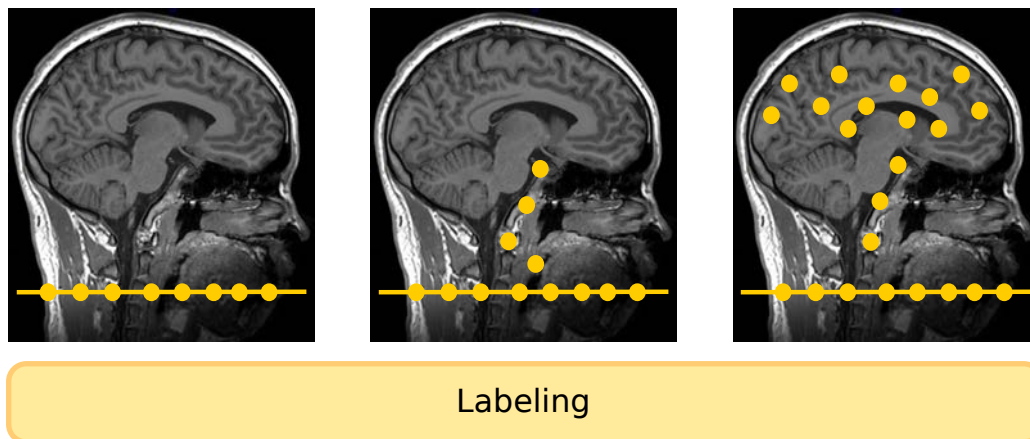


Figure 2.2: Principle of continuous arterial spin labelling.

### 2.3.2 Pulsed ASL

Contrary to CASL, pulsed arterial spin labelling corresponds to the application of one or a few radio-frequency pulses (10 to 20 ms), inverting blood water magnetization located in a thick slab (10 to 20 cm). Figure 2.3 provides a schematic view of this pulsed labelling approach. While this method allows an improvement of the labelling efficiency, PASL SNR is inferior to the one of CASL acquisitions.

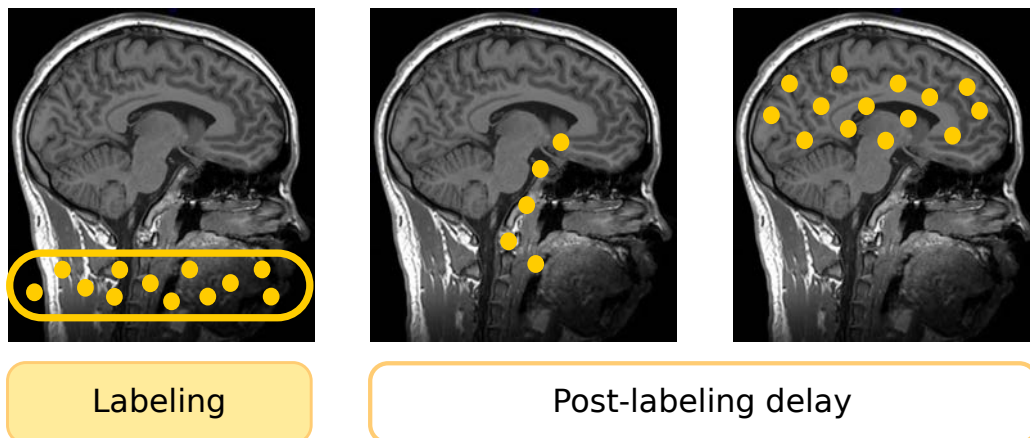


Figure 2.3: Principle of pulsed arterial spin labelling.

Different labelling schemes have been proposed in order to address limitations of this labelling approach. Echo planar imaging signal targeting with alternating

radio-frequency pulses (EPISTAR) was first introduced as a single slice PASL imaging technique [Edelman 1994]. This method begins with a  $90^\circ$  slice-selective pulse saturating magnetization in a region slightly larger than the imaged slice. This saturation is followed by a  $180^\circ$  adiabatic radio-frequency pulse inverting the magnetization of a thick slab of inflowing blood water protons. The control image is acquired by applying the same operations, but inverting the magnetization above the imaged slice. This particularity allows a limitation of the influence of magnetization transfer on the ASL signal. This technique was extended to multi-slice acquisitions in the pulsed signal targeting with alternating radio-frequency (PULSAR) method [Golay 2004].

Proximal inversion with control of off-resonance effects (PICORE), is an other PASL method, that that is similar to EPISTAR, but differs in the fact that the control inversion pulse is applied at the same frequency offset relative to the imaging slice as the tagging sequence, but in the absence of a spatial gradient [Wong 1997].

In flow-sensitive alternating inversion recovery (FAIR), the magnetization inverted slab is located around the imaged slice, and the whole volume is subject to the control inversion [Kim 1995]. This method is more sensitive to venous tagged blood contamination and difficult to implement for multi-slice acquisitions.

A precise quantification of CBF is nonetheless impossible using these methods alone, because of the short, but unknown, temporal width of the labelled bolus. Quantitative imaging of perfusion using a single subtraction (QUIPSS) applies an additional saturation pulse to the imaged slices (QUIPSS-I) or to the labelling slab (QUIPSS-II), in order to provide a better temporal definition of the bolus [Wong 1998]. An evolution of these techniques, QUIPSS-II with thin-slice T1 periodic saturation (Q2TIPS), consisting in a train of saturation pulses during 800 to 1200 ms, is also commercially available [Luh 1999].

### 2.3.3 Pseudo-continuous ASL

Pseudo-continuous arterial spin labelling (pCASL) is a method combining advantageous aspects of both CASL and PASL. Labelling is performed on blood water protons flowing through a slice located at the level of the neck of the imaged subject, by applying a train of labelling pulses [Dai 2008]. The global value of the radio-frequency pulses applied in pCASL is the same than in CASL, but the pseudo-continuous approach is preferred because of its better adaptation to commonly available hardware, and its higher labelling efficiency, closer to the one obtained using PASL. Because of this increased labelling efficiency, and a higher SNR than in the case of PASL acquisitions, pCASL has been recommended by a consortium of experts as the reference ASL acquisition scheme [Alsop 2015].

### 2.3.4 Vessel encoded pCASL

Vessel encoded pseudo-continuous arterial spin labelling provides perfusion parameter maps resulting from the labelling of blood water protons flowing through one



of the four arteries delivering blood to the brain. When the four maps are joined together, maps similar to the ones which could be obtained by means of a classical pCASL acquisition are generated. But getting individual maps for each of the arteries can provide useful information in the case of cerebrovascular disease, collateral flow or in order to study lesions blood supply [Wong 2007, Okell 2013].

## 2.4 Acquisition parameters

### 2.4.1 Labelling duration and post-labelling delay

The sensitivity of the ASL signal to arterial transit time has been outlined, leading to the introduction of a delay between blood water protons labelling and image acquisition [Alsop 1996]. This delay is named differently in the PASL and pCASL contexts, which is related to implementation differences. In PASL, the delay introduced between the short spin tagging operation and the image acquisition is called inversion time (TI). In pCASL, the duration of the spin tagging step is called labelling duration (LD), and the time between the end of this labelling operation and the image acquisition, the post-labelling delay (PLD). Figure 2.4 illustrates these aspects for pCASL and QUIPSS-II PASL acquisitions.

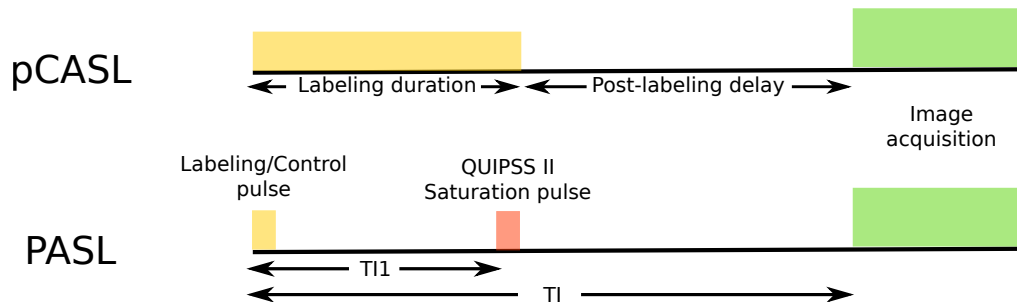


Figure 2.4: Timing diagram of pCASL and PASL (QUIPSS-II) acquisitions.

### 2.4.2 Single-TI and multi-TI acquisitions

ASL acquisitions can also be classified into single or multi-TI acquisitions, names simply chosen identical in cases of PASL and pCASL acquisitions. In single-TI ASL, a duration at least as long as the longest estimated arterial transit time must be chosen as TI or PLD. The objective is to ensure that all tagged molecules entered brain microvasculature before acquiring images. Because blood velocity is different in children, adults or clinical patients, TI and PLD have to be adapted accordingly. LD and PLD values recommended by an international consortium are presented in table 2.1 [Alsop 2015].

Parameter	Value
PASL $TI_1$	800 ms
PASL TI	Same as pCASL PLD
pCASL LD	1800 ms
pCASL PLD (neonates)	2000 ms
pCASL PLD (children)	1500 ms
pCASL PLD (healthy subjects < 70 years)	1800 ms
pCASL PLD (healthy subjects > 70 years)	2000 ms
pCASL PLD (adult clinical patients)	2000 ms

Table 2.1: Recommended LD and PLD for single-TI pCASL and QUIPSS-II PASL acquisitions [Alsop 2015].

Multi-TI acquisitions consist in acquiring images with various TI or PLD, in order to obtain ASL signal time series. These series have the advantage of allowing a direct estimation of more parameters than the single-TI approach. The main disadvantage of multi-TI scans is the reduced SNR obtained for each ASL image, because of reduced repetition numbers of label and control image acquisitions allowed at each TI during a clinically reasonable acquisition time. Figure 2.5 shows the evolution of the ASL signal in an axial slice, at different PLDs in a multi-TI acquisition.

### 2.4.3 Background suppression

As stated in 2.2, intensities between control and label images only differ by at most 5%. Because of this aspect, the ASL signal has a relatively low SNR. Artifacts can also be introduced during the acquisition, impairing the ASL signal. Therefore, the use of background suppression (BS) can be recommended [Maleki 2011, Garcia 2005]. This technique consists in canceling the longitudinal magnetization of static spins located in the imaged brain region, by means of saturation and inversion pulses. As a consequence, intensity differences between control and labelled images are preserved, while the influence of artifacts that affect the entirety of the images is decreased. While significantly improving the ASL signal SNR, BS is subject to two main limitations. The labelling efficiency is decreased by 5% for each inversion pulse, resulting in a signal loss that should be taken into account while estimating the cerebral blood flow. The longitudinal magnetization of static tissues is only canceled at a given time point, so that the method is well suited for 3D readout approaches, but not optimal for 2D multi-slice acquisitions.

### 2.4.4 Readout approaches

Because of the possibility to apply an efficient background suppression and their low sensitivity to off-resonance effects, segmented 3D readout approaches are the recommended ASL image acquisition techniques [Günther 2005, Fernández-Seara 2005].

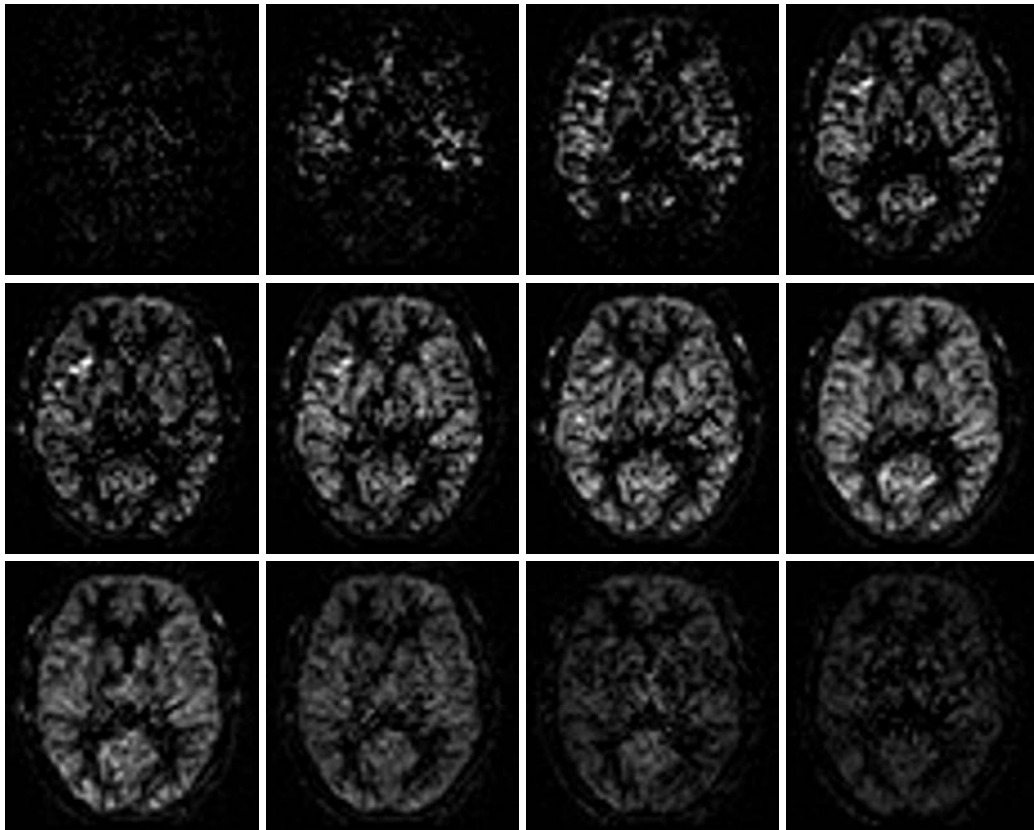


Figure 2.5: From upper left to bottom right: ASL signal evolution in an axial slice corresponding to a multi-TI ASL acquisition (12 TIs ranging from 500 ms to 4240 ms).

However, these sequences are not available on all scanners, and multi-slice single-shot 2D echo-planar imaging (EPI) or spiral readout approaches are more commonly used [Alsop 2015, Vidorreta 2013].

Parallel imaging with moderate acceleration factors can be used in order to reduce the imaging time and distortions [Pruessmann 1999, Griswold 2002, Wang 2005]. A good tradeoff between these advantages and a potential SNR decrease corresponds to the choice of the sensitivity encoding (SENSE) parallel imaging method with an acceleration factor of 2 [Ferré 2012].

Effort is also made to develop ASL multi-band imaging sequences, that allow to acquire multiple 2D slices at the same time [Kim 2013, Li 2015]. This method could be a good alternative to 3D readout approaches, by providing increased temporally and spatially resolved whole brain acquisitions. Early evaluations found to an improvement of high-resolution 2D EPI pCASL image SNR [Li 2015].

### 2.4.5 Vascular flow crushing gradients

Vascular flow crushing gradients consist in dephasing the spins of blood water protons flowing at a velocity superior to an encoding velocity (VENC) value, while maintaining the phase of protons circulating at a velocity inferior to this VENC, that remain visible on the ASL images. The objective is to avoid vascular artefacts, obtained when the PLD is too short and the labelled blood is still flowing through the arteries, generating hyperintense signals in these areas, sometimes masking useful information. Applying flow crushing gradients can therefore be of interest in order to retrieve this masked information, but in that case, acquiring a second ASL scan without applying the crushing gradients is advised if possible, providing indications about the true nature of the ASL signal that should have been obtained. While not recommended for usual ASL image acquisitions, particular applications such as the evaluation of brain tumours or studies implying group comparisons can benefit from the application of these gradients [Wang 2003, Alsop 2015].

## 2.5 ASL signal models

### 2.5.1 General kinetic model

The general kinetic model is based on the assumption that the ASL signal  $\Delta M(t)$ , which is the difference between control and label images acquired at a time  $t$  after the end of the labelling duration can be related to three main effects, represented by time depending functions [Buxton 1998]. The delivery function  $c(t)$  corresponds to the arterial concentration of tagged blood water molecules arriving in a given voxel at time  $t$ . The residue function,  $r(t - t')$ , represents the fraction of tagged molecules that have reached the voxel at time  $t'$  and are still present at time  $t$ . The magnetization relaxation function  $m(t - t')$  models the decrease in magnetization due to the longitudinal magnetization relaxation between times  $t'$  and  $t$ . The measured ASL signal at time  $t$  can therefore be written as follows:

$$\Delta M(t) = 2M_{0b}\alpha f \int_0^t c(t')r(t-t')m(t-t') dt', \quad (2.1)$$

with  $M_{0b}$  the blood equilibrium magnetization,  $\alpha$  the labelling efficiency and  $f$  the CBF.

### 2.5.2 Standard kinetic model

From this general kinetic model, the standard kinetic model has been proposed, that is largely adopted by the ASL community [Buxton 1998], and schematically described in figure 2.6. This model is based on three major assumptions regarding the  $c$ ,  $r$  and  $m$  functions:

1. the arrival of labelled blood water is supposed to be uniform, so that the  $c$  function can be expressed as:

$$c(t) = \begin{cases} 0, & 0 < t < \Delta t \\ e^{-t/T_{1b}}, & \Delta t < t < \Delta t + \tau \\ 0, & \Delta t + \tau < t, \end{cases} \quad (2.2)$$

with  $\tau$  the labelling duration or the bolus width,  $T_{1b}$  the blood longitudinal relaxation time and  $\Delta t$  the arterial transit time.

2. the kinetics is subject to the single compartment model, which means that labelled water exchanges rapidly between blood vessels and brain tissues. Therefore, tissue and arterial transit time can be considered as equal, and the ratio between venous and brain concentrations of labelled water is considered as constant, so that  $r$  can be written as:

$$r(t) = e^{-t/\lambda}, \quad (2.3)$$

with  $\lambda$  the brain-blood partition coefficient of water.

3. labelled blood water magnetization is supposed to decay initially with the blood water relaxation time, and immediately after reaching the imaged brain tissue voxel, with tissue  $T_1$ , so that:

$$m(t) = e^{-t/T_1}. \quad (2.4)$$

Formulating these assumptions, the expression of the ASL signal measured by means of PASL acquisitions follows an evolution expressed as:

$$\Delta M(t) = \begin{cases} 0, & 0 < t < \Delta t \\ 2M_{0b}f(t - \Delta t)\alpha e^{-t/T_{1b}}q_p(t), & \Delta t < t < \Delta t + \tau \\ 2M_{0b}f\tau\alpha e^{-t/T_{1b}}q_p(t), & \Delta t + \tau < t, \end{cases} \quad (2.5)$$

with

$$q_p(t) = \begin{cases} \frac{e^{kt}(e^{-k\Delta t} - e^{-kt})}{k(t-\Delta t)}, & \Delta t < t < \Delta t + \tau \\ \frac{e^{kt}(e^{-k\Delta t} - e^{-k(\tau+\Delta t)})}{k\tau}, & \Delta t + \tau < t, \end{cases}$$

$$k = \frac{1}{T_{1b}} - \frac{1}{T_{1'}},$$

$$\frac{1}{T_{1'}} = \frac{1}{T_1} + \frac{f}{\lambda}.$$

In the case of pCASL or CASL acquisitions, the ASL signal follows the following equation:

$$\Delta M(t) = \begin{cases} 0, & 0 < t < \Delta t \\ 2M_{0b}fT_{1'}\alpha e^{-\Delta t/T_{1b}}q_{ss}(t), & \Delta t < t < \Delta t + \tau \\ 2M_{0b}fT_{1'}\alpha e^{-\Delta t/T_{1b}}e^{-(t-\tau-\Delta t)/T_{1'}}q_{ss}(t), & \Delta t + \tau < t, \end{cases} \quad (2.6)$$

with

$$q_{ss}(t) = \begin{cases} 1 - e^{-(t-\Delta t)/T_{1'}}, & \Delta t < t < \Delta t + \tau \\ 1 - e^{-\tau/T_{1'}}, & \Delta t + \tau < t. \end{cases}$$

Given equations 2.5 and 2.6, the ASL signal follows an evolution similar to the curve displayed in figure 2.7.

While this standard model is the most commonly used in quantitative ASL CBF related studies, and is the one in use in the next sections of this document, a two-compartment model has been proposed, that is described in the following section.

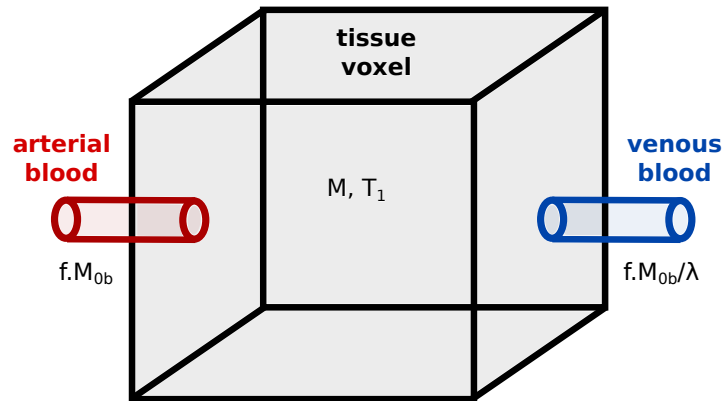


Figure 2.6: Schematic description of the standard model.

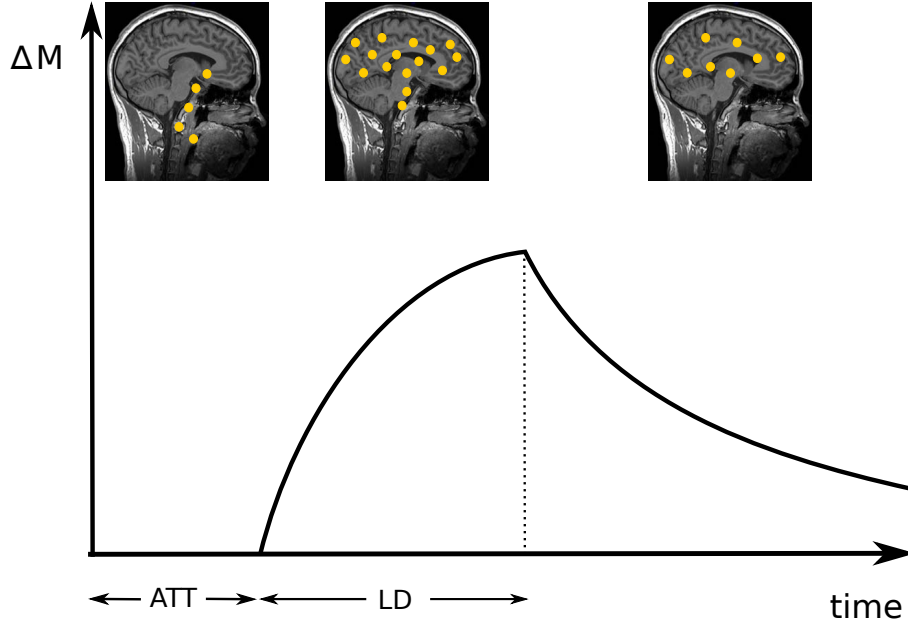


Figure 2.7: Signal evolution following the standard model.

### 2.5.3 Two compartment model

The two compartment model aims to include two major assumptions regarding brain blood microcirculation [Parkes 2002]. The first one, called the  $T_1$  effect, consists in considering that labelled blood water molecules are not directly exchanging with extravascular tissues, but flowing through blood vessels during some time before this exchange occurs. The second assumption, called the outflow effect, corresponds to the hypothesis that a certain amount of labelled blood water will not exchange with the extravascular space at all. Both assumptions lead to a new formulation of the ASL signal  $\Delta M(t)$ , as the sum of contributions from two compartments, the extravascular and the intravascular ones:

$$\Delta M(t) = v_{ev} \Delta m_e(t) + v_{iv} \Delta m_i(t), \quad (2.7)$$

with  $v_{ev}$  and  $v_{iv}$  the respective volume fractions of the extra and intravascular compartments, and  $m_e(t)$  and  $m_i(t)$  the corresponding water magnetizations. Introducing the permeability surface area product (PS), the following evolution for the intra and extravascular compartments is obtained [Parkes 2002]:

$$\frac{d(v_{iv} \Delta m_i(t))}{dt} = -\frac{v_{iv} \Delta m_i(t)}{T_{1b}} + f \Delta m_a(t) - f \Delta m_v(t) + PS(\Delta m_e(t) - \Delta m_i(t)), \quad (2.8)$$

$$\frac{d(v_{ev} \Delta m_e(t))}{dt} = -\frac{v_{ev} \Delta m_e(t)}{T_{1e}} + PS(\Delta m_i(t) - \Delta m_e(t)), \quad (2.9)$$

with  $m_a$  the incoming arterial magnetization and  $m_v$  the outgoing venous magnetization.

A schematic description of this two compartments model is provided in figure 2.8.

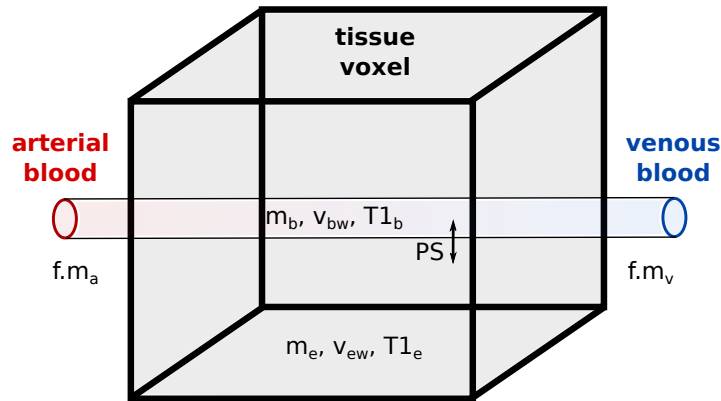


Figure 2.8: Schematic description of the two compartment model.

## 2.6 Processing pipelines

This section presents ASL image processing pipelines developed in the context of this thesis. The pipeline dedicated to single-TI acquisitions is described in the first subsection. The pipeline built to process multi-TI ASL data is presented in the second subsection. These inhouse ASL image processing pipelines have been developed using Python, Nipype [Gorgolewski 2011] and a standalone version of SPM8 [SPM 2006].

### 2.6.1 Single-TI ASL image processing pipeline

Figures 2.9 and 2.10 present the automated structural and ASL image processing pipeline dedicated to single-TI ASL acquisitions. Inputs of this pipeline are a structural image, usually consisting in a magnetization-prepared rapid gradient-echo (MPRAGE, [Mugler 1990]) or a magnetization-prepared 2 rapid gradient echo (MP2RAGE, [Marques 2010]) image, an equilibrium magnetization image ( $M_0$ ) and an ASL control and label image time series.

The structural image is first bias corrected and segmented into probability maps of gray matter, white matter, cerebro-spinal fluid, bone and soft tissues by means of the unified segmentation algorithm [Ashburner 2005].

A realignment of the ASL series is then performed by applying a six parameters rigid registration of all control and label volumes to the mean of these volumes. The control and label images are pairwise subtracted in order to generate a realigned ASL signal time series. The  $M_0$  and ASL series are then registered to the structural image



by applying a mutual information based rigid registration. The temporal mean of the ASL signal series is calculated, to which the  $M_0$  image is resliced, in order to quantitatively estimate the cerebral blood flow (CBF) by applying the standard kinetic model [Buxton 1998]. The temporal standard deviation of the realigned ASL signal series is also generated, because of its interesting contribution in the ASL acquisitions quality assessment. The mean CBF values are finally calculated within the brain, gray matter and white matter masks.

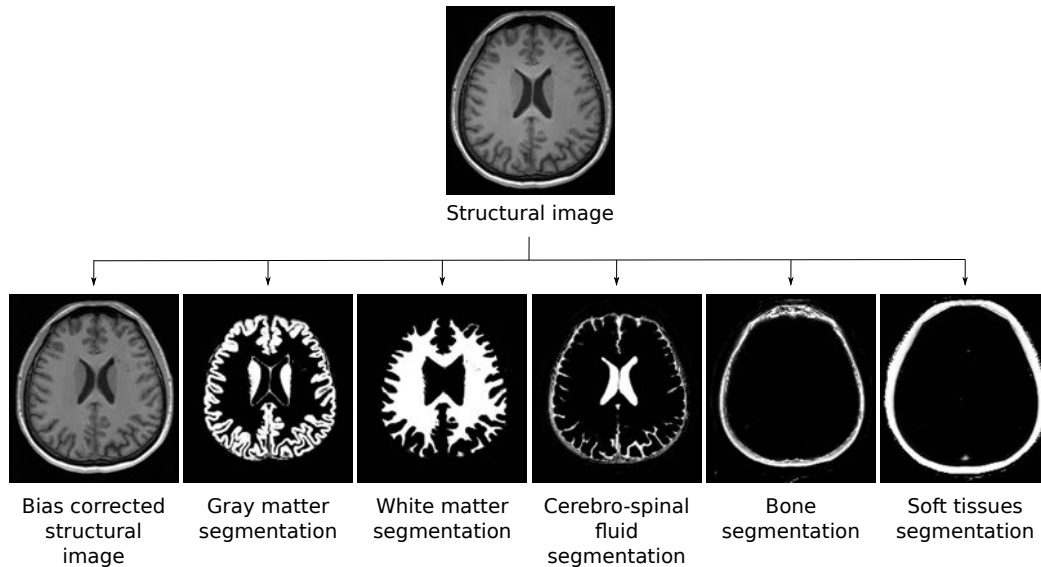


Figure 2.9: Structural image processing.

This pipeline has been adapted to the CATI database management system (CATIDB), as well as to a file organization similar to the brain imaging data structure (BIDS) standard [Gorgolewski 2016], only slightly different because of its earlier development.

### 2.6.2 Multi-TI image processing pipeline

A processing pipeline dedicated to multi-TI ASL acquisitions was also implemented in the context of this thesis. This pipeline is adapted to a files organization similar to the BIDS standard. Inputs to this pipeline are at least a structural image, and time series constituted of the control-label images acquired at each TI or PLD. External  $M_0$  and quantitative tissue  $T_1$  images can also be provided as inputs.

The whole original ASL time series is first registered to the mean of all control and label volumes by means of a rigid registration. The control-label pairs images are then subtracted in order to generate ASL series at each TI. The mean of each of these series is then calculated, in order to obtain a series of mean ASL images, containing a number of images equal to the number of TIs. The processing pipeline



then differs depending whether external  $M_0$  and quantitative tissue  $T_1$  images are available or not.

### 2.6.2.1 With external $M_0$ and tissue $T_1$ acquisitions

When external  $M_0$  and quantitative tissue  $T_1$  images have been acquired, the cerebral blood flow (CBF) and the arterial transit time (ATT) are voxelwise estimated from the ASL time series by applying a voxelwise non-linear least-squares fitting of the standard kinetic model, in which the  $M_0$  and tissue  $T_1$  values are provided by the available images (figure 2.11).

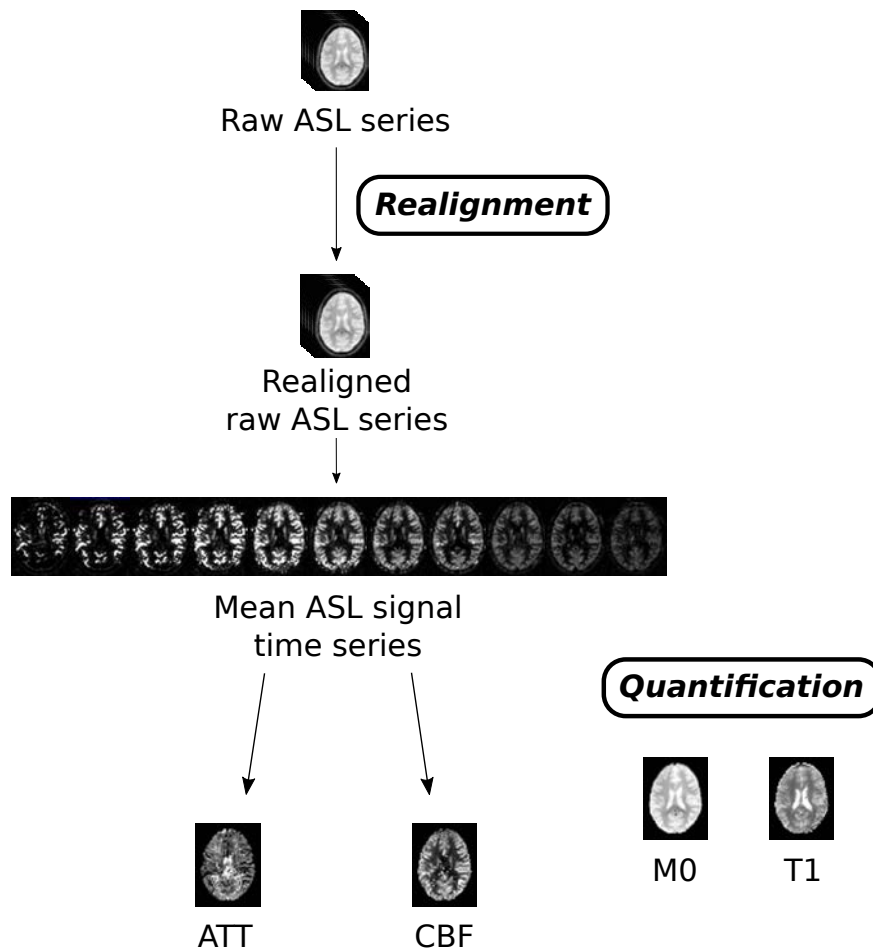


Figure 2.11: Multi-TI ASL image processing pipeline with external  $M_0$  and quantitative tissue  $T_1$  acquisitions.

### 2.6.2.2 Without external $M_0$ and tissue $T_1$ acquisitions

When no external  $M_0$  and tissue  $T_1$  scans are available, the pipeline allows their estimation from the original ASL control and label images time series, if a saturation

is applied to the imaged brain area directly at the end of each repetition time, and no background suppression is used [Johnston 2015]. All the control and label images acquired at a given TI are averaged, which creates a time series of images in which individual voxels follow a  $T_1$  recovery curve, as shown in figure 2.12. This  $T_1$  recovery can be formulated as follows:

$$M(t) = M_0(1 - m \cdot \exp(-t/T_1)) \quad (2.10)$$

with  $M$  the longitudinal magnetization measured at each TI, and  $m$  a scalar accounting for imperfect signal saturations.  $M_0$  and tissue  $T_1$  can therefore be estimated by means of a voxelwise least-squares fit of this curve on the averaged control and label images time series, as in figure ???. The maps estimated this way can then be used in order to estimate CBF and ATT in a similar manner to that presented in 2.6.2.1 (figure 2.14).

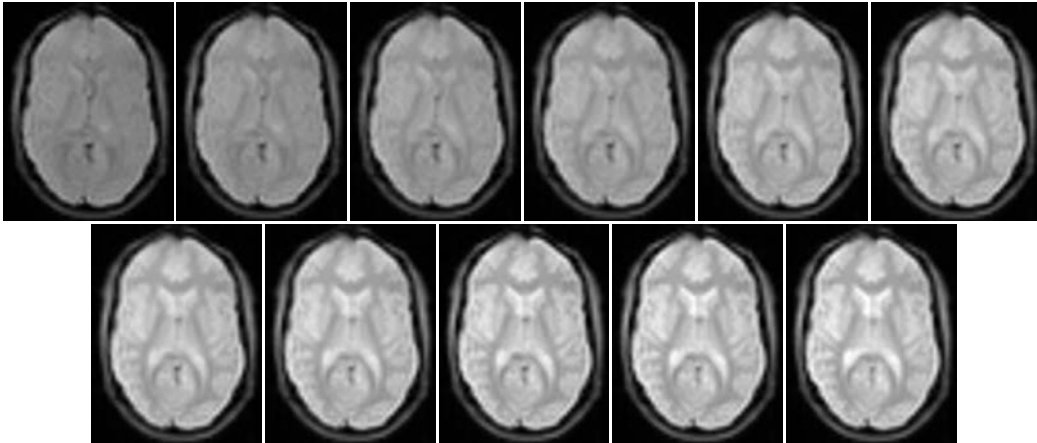


Figure 2.12: Upper left to bottom right: signal evolution in an axial slice of an averaged control and label time series.

## 2.7 Thesis objectives

This document presents studies conducted following a progressive way. First, in the context of the development of a French multicenter neuroimaging platform, the CATI, work has been performed in order to answer the need for ASL acquisitions standardization in studies involving different vendors and scanners. ASL sequences parameters had to be adapted to acquire large cohorts of subjects, mostly elderly patients diagnosed with a form of dementia or neurodegenerative disease. The definition of a semi-automated ASL images quality assessment procedure was associated to this standardization work, with the objective to allow clinical research assistants to evaluate the conformity of acquisitions coming from multiple centers, and the potential presence of artifacts in the images. These aspects are presented in part II.

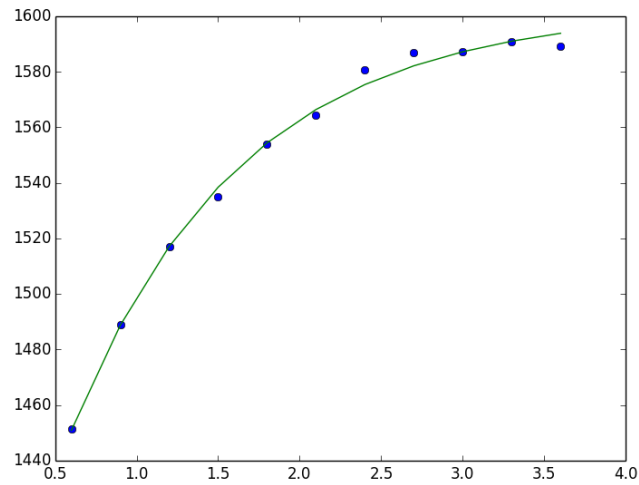


Figure 2.13: Fitting of the  $T_1$  recovery curve on the signal evolution of a voxel in an averaged control and label time series.

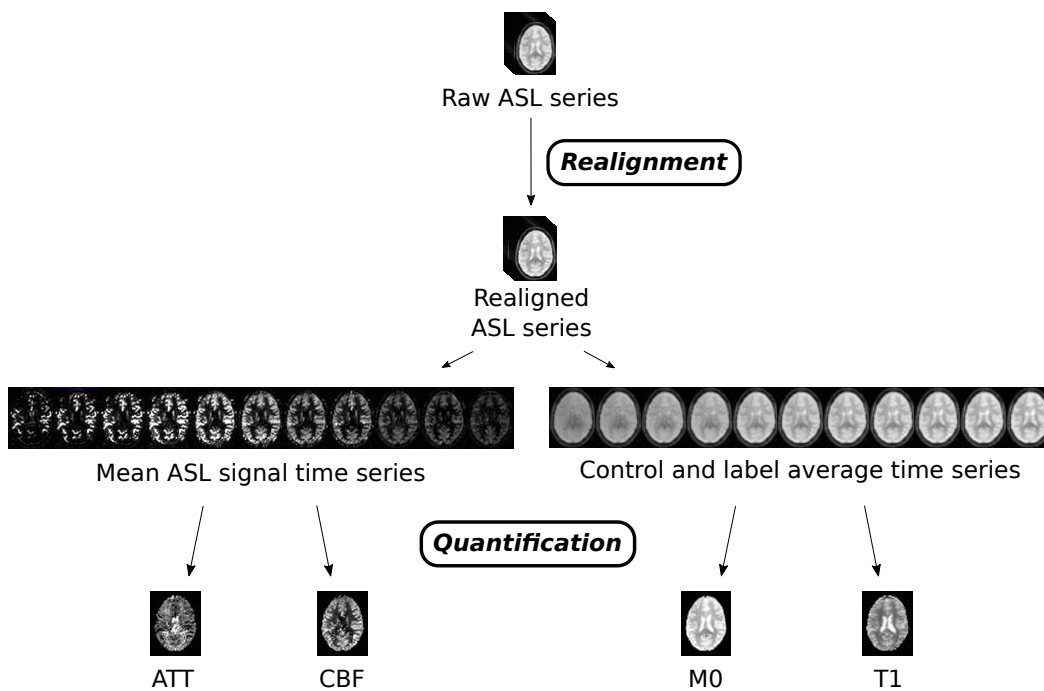


Figure 2.14: Multi-TI ASL image processing pipeline without external  $M_0$  and quantitative tissue  $T_1$  acquisitions.

---

In a second phase, an assessment of the possibility to apply existing distortion correction methods on ASL data is presented in chapter 4. These methods, developed to correct for susceptibility artifacts in MR images that are not specifically ASL data, have been evaluated on ASL scans acquired on healthy subjects.

Then, image processing methods have been developed in order to address certain limitations of ASL images. A super-resolution reconstruction method adapted to ASL data acquired in the context of common clinical imaging protocols is presented in chapter 5. Finally, an extension of this super-resolution method to multi-TI ASL acquisitions is presented in chapter 6.

Discussions of these contributions, as well as a presentation of perspectives are provided in part 6.4.



## Part II

# Image quality assessment





# Standardization and quality assessment of ASL scans in multicenter neuroimaging studies

---

## Contents

---

<b>3.1</b>	<b>Introduction</b> . . . . .	<b>38</b>
<b>3.2</b>	<b>Acquisition parameters standardization</b> . . . . .	<b>38</b>
3.2.1	Material and method . . . . .	40
3.2.2	Results . . . . .	42
3.2.3	Conclusion . . . . .	43
<b>3.3</b>	<b>Artifacts</b> . . . . .	<b>45</b>
3.3.1	Motion . . . . .	45
3.3.2	Vascular artifacts (hyperintense ASL signal) . . . . .	46
3.3.3	Signal inhomogeneities . . . . .	46
3.3.4	Parallel imaging . . . . .	46
3.3.5	Distortion . . . . .	48
3.3.6	Conclusion . . . . .	48
<b>3.4</b>	<b>Implemented quality assessment method</b> . . . . .	<b>48</b>
3.4.1	Acquisition parameters conformity assessment . . . . .	49
3.4.2	ASL images quality assessment . . . . .	49
<b>3.5</b>	<b>Discussion</b> . . . . .	<b>53</b>

---

### 3.1 Introduction

As ASL demonstrated its potential to outline abnormal perfusion patterns in patients affected by different kinds of pathologies, the center for images acquisition and processing (CATI), a French multicenter neuroimaging platform created to handle neurodegenerative disease and psychiatry related imaging studies, decided to include ASL sequences in some of the protocols to be deployed.

The CATI is a consortium of neuroimaging research laboratories: *NeuroSpin*, the French high-field MR imaging center of the central commission for nuclear and alternative energies (*CEA*), and four teams located in La Pitié-Salpêtrière Hospital: the neuroimaging analysis research team (*ARAMIS*) and the neuroimaging platform of the Brain and Spine Institute (*CENIR*), the Institute for Memory and Alzheimer’s disease (*IM2A*) and an INSERM-Sorbonne Université unit focusing on research on functional imaging (*LIB*). These teams have been collaborating since 2011, and are funded by a French Alzheimer’s disease initiative. More than 10000 subjects have been scanned at least once in the context of a study in which the CATI is involved, on a scanner located in one of the cities figuring in figure 3.1.

Key steps in the implementation of multicenter imaging studies are the standardization of the acquisition protocols and the quality assessment of the acquired images. The work presented in this chapter focuses on these two aspects. We first present a study conducted in order to standardize acquisition protocols from scanners of two different vendors. An overview of the main artifacts that can impair ASL acquisitions and images is provided in the second section. Finally, the proposed semi-automated ASL images quality assessment procedure is described in the third section.

The standardized protocols have been deployed in the centers participating in neuroimaging studies supervised by the CATI, and the quality assessment procedure and the associated software are currently used by the clinical research assistants working for the CATI. This work was presented at the European Cooperation in Science and Technology (eCOST) Action: ASL in dementia Workshops in March and October 2015.

### 3.2 Acquisition parameters standardization

The objective of this work was to propose standardized ASL images acquisition protocols to be included in some research studies apportioned to the CATI. This initiative was taken at a time when other studies were conducted, as [Mutsaerts 2015], investigating the possibility to include ASL acquisitions in multicenter imaging protocols. This particular study outlined that pooling multicenter or multivendor ASL results is only possible if near-identical sequences parameters are used in order to acquire the images. This aspect is even shown to be more important than hardware or software considerations.

We chose in our study to focus on the standardization of 2D EPI pCASL sequences. Indeed, even if 3D readout approaches correspond to the recommendation

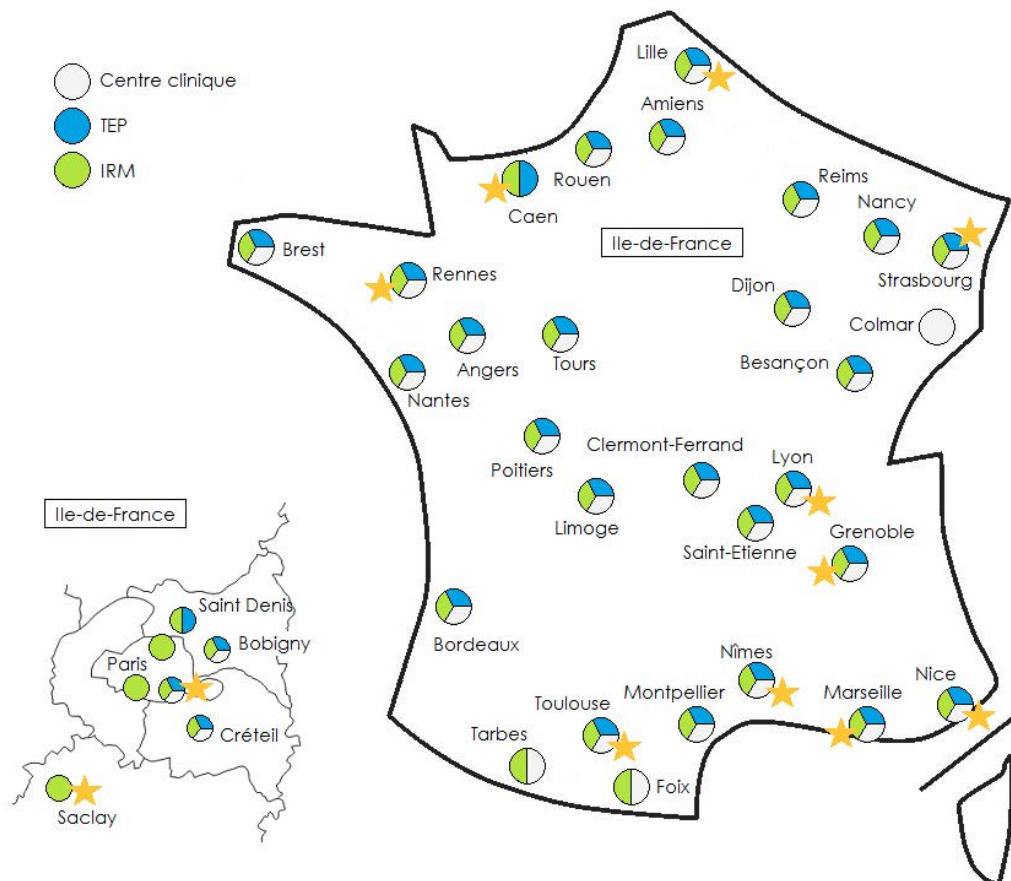


Figure 3.1: French sites participating in research studies in which the CATI is involved. Research teams are located in sites marked with a star. The other sites perform images acquisitions in a clinical context. (*i2bm.cea.fr*)

provided in the ASL white paper [Alsop 2015], most of the centers participating in images acquisitions were equipped with 2D EPI sequences at the time of this investigation. Acquisitions were performed on scanners of two different vendors: a 3T Siemens Verio (software version: VB17), Rennes, France, and a 3T Philips Achieva (software version: 3.2.3), Grenoble, France, both equipped with 32-channel head coils.

This work did not involve any direct participation of the vendors, and did not have as an objective to outline the superiority of a scanner against the other. Therefore, we chose to anonymise and refer to the scanners by means of A and B in this document.

### 3.2.1 Material and method

Data were acquired on 10 healthy subjects (6 females, 4 males,  $53 \pm 17$  years old) and a patient diagnosed with dementia (male, 69 years old). 7 healthy subjects and the patient were imaged on scanner A, and 3 healthy subjects on scanner B. The acquired images consisted in a MPRAGE structural image, a pCASL sequence (2D gradient-echo EPI readout, resolution:  $3.5 \times 3.5 \times 5$  mm<sup>3</sup>, 1 mm interslice gap, FOV:  $224 \times 224$  mm<sup>2</sup>, 20 slices, 30 control-label pairs), and five M<sub>0</sub> images (2D gradient-echo EPI readout, resolution:  $3.5 \times 3.5 \times 5$  mm<sup>3</sup>, 1 mm interslice gap, FOV:  $224 \times 224$  mm<sup>2</sup>, 20 slices, TR: 10000 ms) to be averaged in order to generate a single M<sub>0</sub> map used to quantify CBF. The acquisition box was placed parallel to the anterior-posterior commissure line (CA-CP). The labelling plane was located 90 mm under the lowest slice. The parallel imaging method was selected as SENSE by default [Pruessmann 1999]. Subjects were asked to remain their eyes closed, without sleeping and if possible thinking about nothing. Table 3.1 summarizes these fixed acquisition parameters. Due to low quality acquired ASL data, images from one of the subjects imaged on scanner A needed to be removed from the study.

Antenna	FOV (mm <sup>2</sup> )	Voxels size (mm <sup>3</sup> )	Slices	Repetitions
32ch	224 × 224	3.5 × 3.5 × 5	20	30

Slice thickness (mm)	Orientation	Phase encoding direction	Frequency encoding direction
5 (20% gap)	CA-CP	P>>A	R>>L

Table 3.1: Fixed parameters selected to perform the standardization study.

The imaging parameters to be optimized were the repetition time (TR), the echo time (TE), the labelling duration (LD) and the post-labelling delay (PLD). The tested TR values consisted in the minimal values that could be reached on the scanners, compared to TR=4560 ms, which was the value usually selected to perform ASL acquisitions in one of the centers. Similarly, the minimal TE values achievable on the scanners were compared to TE=12 ms, the value selected by default on the same scanner. The ranges taken under consideration for LD and PLD were largely inspired by the recommendations provided in the ASL white paper [Alsop 2015]. LD equal to 1650 ms and 1800 ms, and PLD ranging from 2020 ms to 2370 ms at the level of the central slice were evaluated. Indeed, PLD=2000 ms is recommended in the case of acquisitions performed on adult clinical patients or healthy subjects older than 70 years old. We wanted to investigate the possibility of an increase of the PLD, because of the fact that in the context of dementia or neurodegenerative disease, an important number of patients are actually older than 70 years old, and present a reduced or prolonged ATT in regions of interest. Furthermore, structures of interest in the case of dementia or neurodegenerative disease are most of the time located in the lower half of the imaged brain volume (hippocampus, ventricles), an area that can be subject to arterial ASL signal perturbations if the PLD is too short. The evaluated parameters combinations are summarized in table 3.2. All combinations could not be evaluated in all subjects because of the necessity to keep the total scan time within an acceptable duration. Therefore, the number of subjects imaged with each parameters combination is indicated in the table.

Data were processed by means of the pipeline presented in 2.6.1. In order to evaluate the influence of each parameter (TR, TE, LD and PLD), automated calculations were performed. The temporal signal-to-noise ratio (tSNR) was calculated on the pairwise subtracted control-label series, over the whole brain and on the segmented gray and white matter. CBF quantification completed the automated measurements. A visual analysis of the CBF maps was also conducted by a trained neuroradiologist. The reviewed criteria included the signal homogeneity, the tissue contrast, and the potential presence of vascular artifacts. Scores ranging from 0 (non satisfactory) to 3 (very satisfactory) were attributed to each scan. Figure 3.2 illustrates this quality review process.

After selecting the TR, TE, LD and PLD, an additional healthy subject was imaged on scanner A in order to evaluate the influence of the parallel imaging method on the quality of the ASL acquisitions. Indeed, while it has been shown that deactivating the largest number of options is recommended in order to facilitate comparability between sequences available on different scanners [Mutsaerts 2015], we believed that using a parallel imaging method, and thus reducing the acquisition time and risks of patient motion that could occur in the case of elderly subjects diagnosed with a form of dementia, was important. The objective was also to ensure that the results obtained in [Ferré 2012] from PASL scans, were still applicable to pCASL acquisitions. Two repetitions of acquisitions with both GRAPPA and SENSE parallel imaging methods were performed, with an acceleration factor of 2. The other parameters correspond to the ones selected by means of the TR, TE, LD

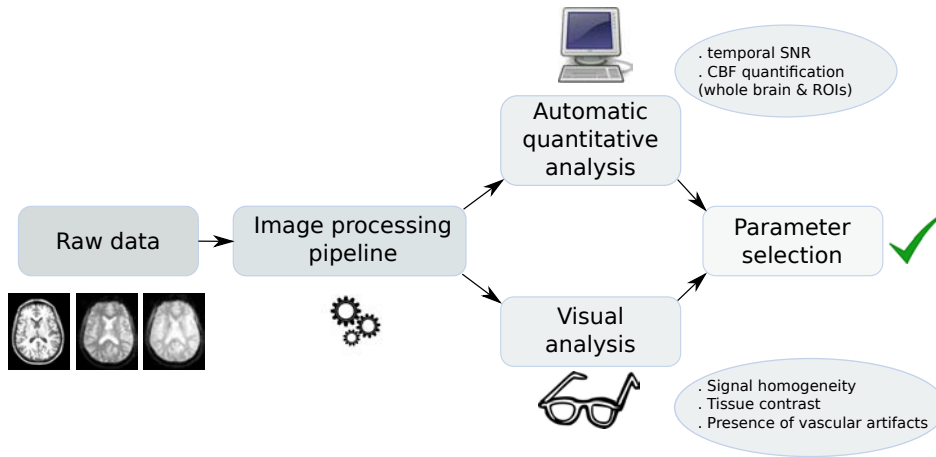


Figure 3.2: Images evaluation method adopted to perform the acquisition parameters standardization.

and PLD investigation.

### 3.2.2 Results

Table 3.2 presents the tSNR, brain CBF, and mean visual scores obtained from images acquired with the evaluated parameters combinations. tSNRs calculated on ASL series generated from acquisitions performed on scanner B were significantly higher than the ones measured on images originating from scanner A, which is the reason why both are separated in the table. Reasons for this difference may be related to different reconstruction methods, coil design, or the automatic application of a processing filter in scanner B.

While we could not provide an explanation for this aspect, the ASL images obtained from data acquired with LD=1650 ms were all associated with strong arterial signals, which explains the very low corresponding visual scores. These strong arterial signals can also explain the differences in CBF values.

No significant differences could be observed between images acquired with different TE values. Therefore, TE=12 ms appears as a good choice in the interest of sequences homogeneity accross scanners.

With LD=1800 ms, images acquired with PLD=2370 ms were less contrasted than the ones generated from acquisitions performed at lower PLD values, which explains the lower visual score attributed to the corresponding scans. This can be explained by the relaxation of the magnetization of the tagged blood water protons, and the venous outflow. tSNR and CBF measurements provided satisfactory values for datasets obtained with PLD=2020 ms and PLD=2170 ms. Nevertheless, the fact that 2 of the acquisitions performed with PLD=2020 ms presented enhanced arterial signals oriented our choice toward PLD=2170 ms for use in the neuroimaging studies. Higher tSNR and visual scores obtained with TR=4560 ms compared to

the minimal TR values led us to choose the following sequence as a result of this parameters optimization study: LD=1800 ms, PLD=2170 ms, TR=4560 ms and TE=12 ms.

Figure 3.3 presents the voxelwise measured temporal signal-to-noise ratio (tSNR) and the CBF values for the whole brain, gray matter and white matter in the context of the parallel imaging methods investigation. Compared to GRAPPA parallel imaging, the SENSE method shows increased tSNR and CBF values, and was therefore selected as the method to use in the context of neuroimaging studies supervised by the CATI. A summary of the selected parameters is presented in table 3.3.

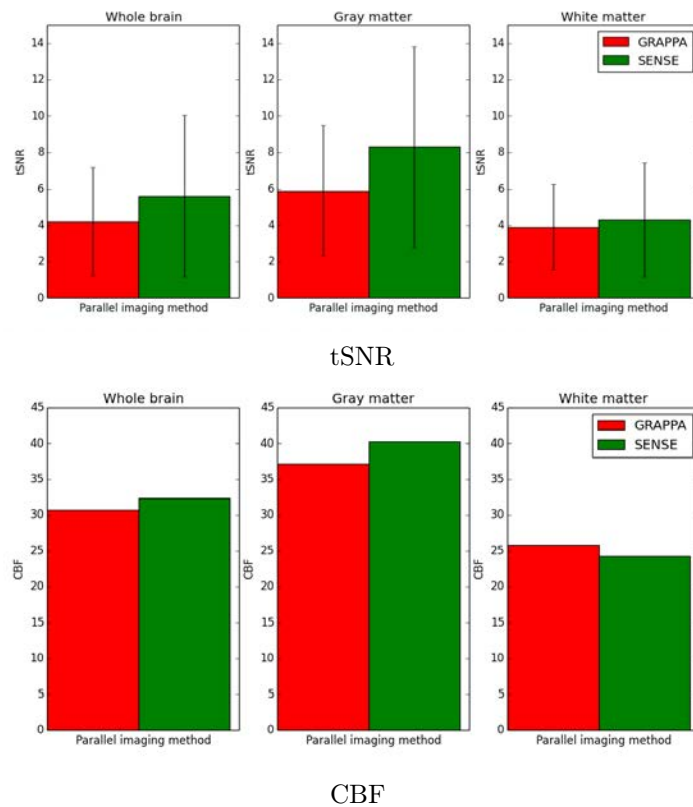


Figure 3.3: Data obtained in a healthy subject: tSNR and CBF calculated on the whole brain, gray matter and white matter for the GRAPPA and SENSE parallel imaging methods.

### 3.2.3 Conclusion

This study allowed to provide ASL images acquisition guidelines to centers participating in research studies. Visits on sites were organized in order to install the acquisition protocol directly on some scanners.

The first datasets received from the centers equipped with the chosen protocol allowed to study artifacts that can be encountered in ASL images, and to develop a



LD	PLD	TR	TE	Subjects	tSNR scanner A	tSNR scanner B	CBF	Visual score	
1650	2020	min	12	2		12.39		0*	
	2170	min	12	2	8.01		29.74	0*	
		4560	12	2	6.35		46.75	0*	
1800	2020	min	min	2		12.28		2.5	
		4560	12	7	8.19	13.82	31.92	2*	
	2170	min	12	7	7.06	11.41	28.64	2*	
		4560	12	4	5.53		32.71	2	
	2370	2170	4560	12	3	6.89		34.27	2.33
		2370	4560	12	4	6.71		29.79	1

Table 3.2: Number of subjects scanned, tSNR, brain CBF and visual evaluation score associated with each of the parameters combinations used to acquire ASL images in the context of the acquisition parameters standardization study. Asterisks indicate that at least one of the CBF maps generated from the parameters set presented arterial hyper-signal.

TR (ms)	TE (ms)	LD (ms)	PLD (ms) (central slice)	Parallel imaging
4560	12	1800	2170	SENSE

Table 3.3: Parameters selected following the acquisition parameters standardization study.

semi-automated quality assessment procedure.

### 3.3 Artifacts

This section proposes an overview of the main artifacts encountered in the first images provided by the acquisition centers, that impair the quality of ASL images.

#### 3.3.1 Motion

As the subtraction of a control and a label image generates an ASL signal map with a poor SNR, a number of repeated control and label images are usually acquired (usually around 30 control-label images pairs for single-TI acquisitions). This makes ASL sensitive to motion artifacts. Periodic motion affects images in the form of border duplication, while random motion induces hypo-perfusion signal or image blurring, as shown in figure 3.4.

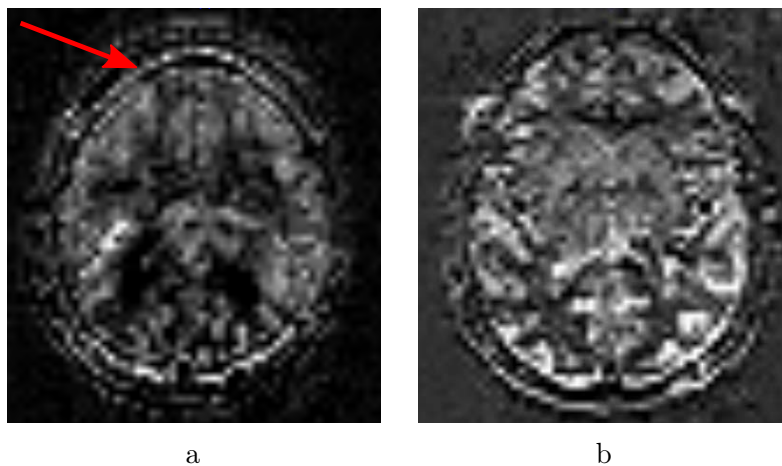


Figure 3.4: Motion artifact in the form of a) border duplication, b) image blurring.

### 3.3.2 Vascular artifacts (hyperintense ASL signal)

Vascular artifacts can appear in two different forms on ASL images. Bright spots can correspond to situations where the TI or PLD is too long and not adapted to the subject's blood velocity. Labelled water molecules having already flown out of brain tissues concentrate in veins and sinuses, that appear as bright points.

If the TI or PLD is too short, labelled water is still in large vessels and has not been provided a sufficient duration to enter the microvasculature. This results in higher intensities in brain regions that are early supplied by blood flowing from the arteries, and a much lower ASL signal in other brain areas. Figure 3.5 presents examples of both forms of vascular artifacts.

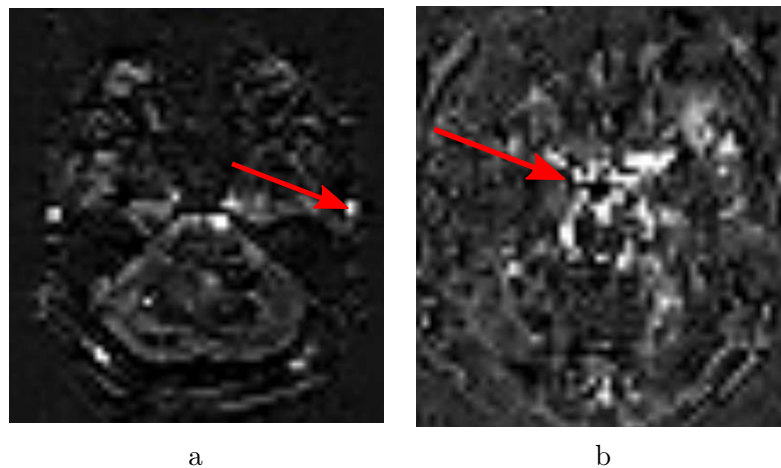


Figure 3.5: Vascular artifact in the form of a) venous hyperintensities, b) arterial hyperintensities.

### 3.3.3 Signal inhomogeneities

Signal drop can be observed in more or less widespread areas. It can be associated with motion or susceptibility artifacts, but can also be caused by labelling issues due to tortuous arteries at the level of the labelling plane (left image in figure 3.6), or patient perfusion abnormalities. Signal inhomogeneities can also correspond to coil sensitivity artifacts, that appear as hypo and/or hyper-perfusion areas (right image in figure 3.6), and can be assessed by looking at the raw control and label images. Low frequency signal variations affecting these raw images allow to conclude that images are affected by a coil sensitivity artifact.

### 3.3.4 Parallel imaging

Parallel imaging artifacts depend on the method chosen to accelerate images acquisition. When SENSE is selected [Pruessmann 1999], a curved line of higher intensity voxels can sometimes be observed on ASL images. This curve is even more visible

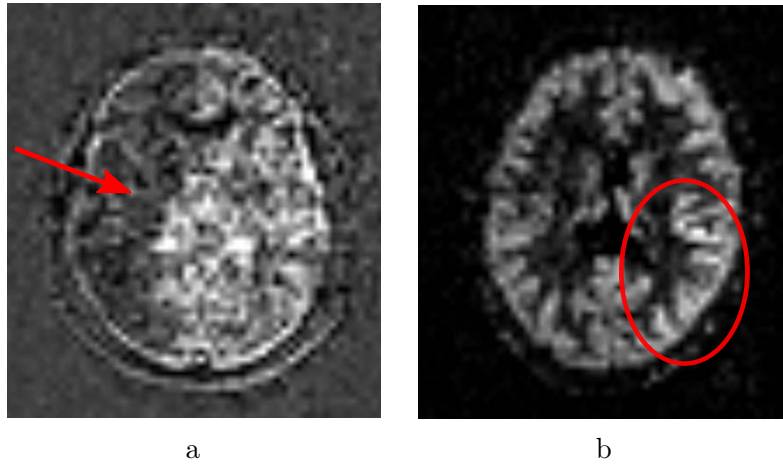


Figure 3.6: Signal drop caused by a) a labelling issue due to a tortuous artery in the labelling plane, b) a susceptibility artifact.

on temporal standard deviation maps, obtained from the temporal ASL series generated by the successive control-label images subtractions, as shown in figure 3.7. This artifact is related to the SENSE algorithm, reconstructing images from signals acquired by each individual reception coil in the image domain.

On the contrary, GRAPPA parallel imaging [Griswold 2002], consisting in a reconstruction of the images in the spectral domain, sometimes conducts to the presence of blur in the images.

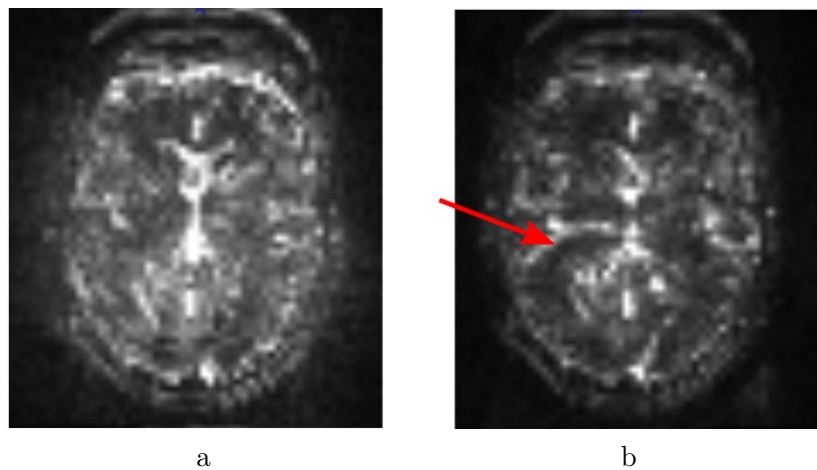


Figure 3.7: Temporal standard deviation maps of ASL series acquired on the same subject with the a) GRAPPA and b) SENSE parallel imaging techniques.

### 3.3.5 Distortion

Distortion can be observed in ASL images (figure 3.8). These artifacts are related to the echo train length (3D readout approaches, such as 3D RARE or 3D GRASE) or the echo time (2D EPI), and result in image deformations in the phase-encoding direction. In the case of axial acquisitions, the encoding direction is therefore advised to be chosen as antero-posterior ( $A \gg P$ ) or postero-anterior ( $P \gg A$ ), depending on the brain structures that are of particular interest and have to be at most preserved in the context of the imaging protocol.

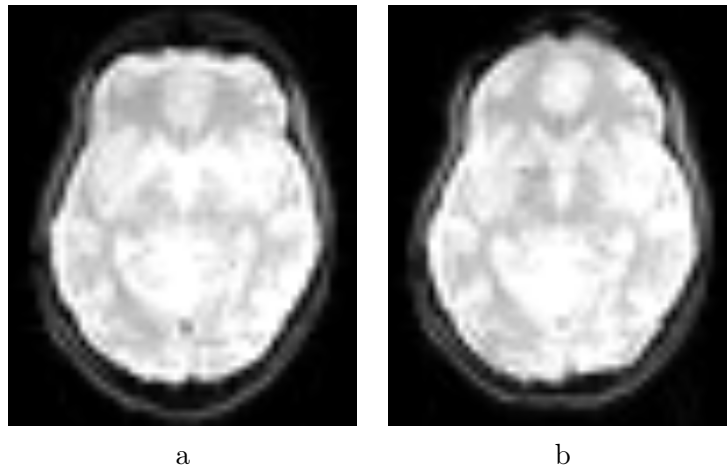


Figure 3.8: Difference between images of the same subject acquired following the a)  $A \gg P$  and b)  $P \gg A$  phase encoding directions.

### 3.3.6 Conclusion

Various kinds of ASL images perturbations were encountered in the first images acquired in the context of this standardization and quality assessment study. We have shown in this section that they can have different origins, related to aspects to generally take into account when dealing with MR acquisitions, as well as perturbations more specific to ASL acquisitions. These aspects have been considered in order to develop the ASL images quality evaluation tool described in the following section.

## 3.4 Implemented quality assessment method

This section presents the quality assessment tools developed and implemented in order to evaluate the conformity of the images received by the clinical research assistants, and the potential presence of artifacts in the ASL images. We will first describe the procedure to verify the acquisition parameters conformity, and then

present the semi-automated software that allows to provide information on the images quality.

### 3.4.1 Acquisition parameters conformity assessment

The quality assessment procedure proposed in the context of this work is largely based on the processing pipeline presented in 2.6.1, therefore requiring the use of a structural image, an equilibrium magnetization image ( $M_0$ ) and an ASL series as DICOM inputs. The DICOM format allows to access information about parameters used to perform the acquisitions. The parameters of interest are, for the  $M_0$  image and ASL series: coil name, field of view, acquisition matrix, slice thickness, spacing between slices, acquisition orientation, phase encoding direction, pixel spacing, repetition time, flip angle, bandwidth, number of acquired volumes,  $B_1$  correction, partial Fourier acquisition fraction, parallel imaging method, parallel reduction factor, oversampling phase and echo time.

Other important parameters such as the post labelling delay or the labelling duration are often indexed as hidden parameters, and cannot be controlled in the context of this verification. Part of the work consisted in installing the acquisition protocols on sites participating in research studies, in order to limit risks of mistakes.

The result of this acquisition parameters review appears as a table on the graphical interface of the quality control software, as shown in figure 3.9.

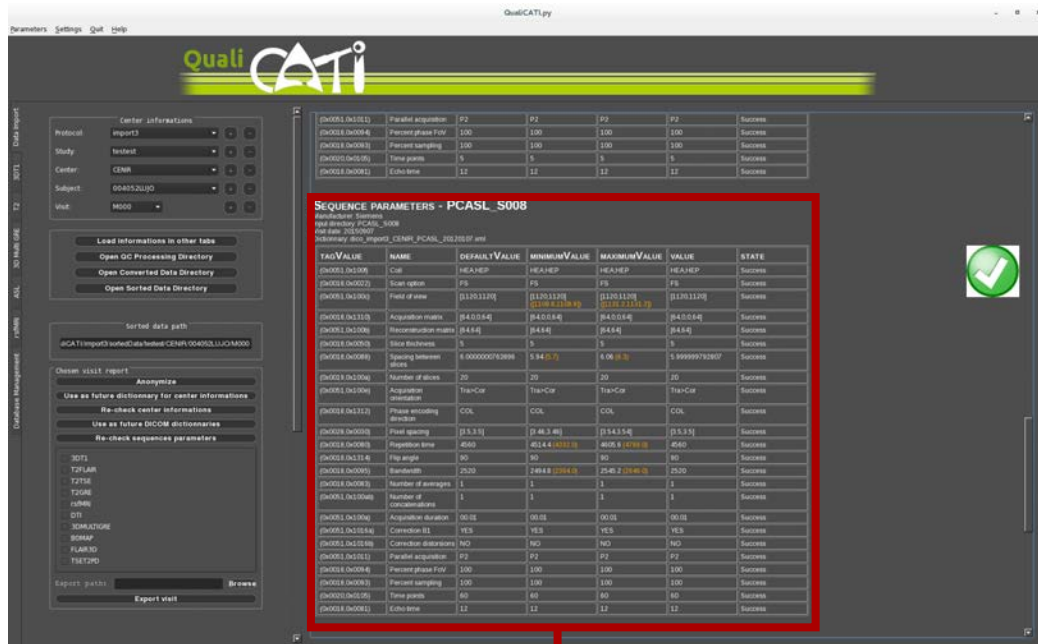
If the parameters match the requirements, the processing pipeline described in 2.6.1 is applied to the raw ASL series.

### 3.4.2 ASL images quality assessment

Images generated at different steps of this processing pipeline are saved and presented to clinical research assistants on a graphical user interface presented in figure 3.10. These images are the raw ASL series, the raw  $M_0$  map (or a series of  $M_0$  maps to be averaged in order to generate an image of higher SNR), the subtracted ASL image, the quantitative CBF map, the map that corresponds to the temporal standard deviation calculated on the ASL time series, and the gray matter partial volume image. A graph that presents the translations calculated to perform the realignment of the raw ASL series is also displayed.

Once all data are available, following the application of the processing pipeline, a panel allows the clinical research assistant to fill different quality criteria. This panel consists of three sections (figure 3.11). The first is related to the evaluation of general criteria concerning the raw and generated images: positioning, head coverage, signal homogeneity and gray/white matter differentiation. A score ranging from 1 to 3 is affected to each category, 1 meaning that an aspect is non satisfactory, 2 acceptable and 3 conform to requirements.

The second section concerns artifacts, such as motion artifacts, distortion, signal drop, bright spots and parallel imaging artifacts. Scores are affected to each artifact, 0 corresponding to an absence of artifact, and 2 a strong artifact.



**SEQUENCE PARAMETERS - PCASL\_S008**

manufacturer: Siemens  
 input directory: PCASL\_S008  
 /sit date: 20150907  
 dictionary: dico\_import3\_CENIR\_PCASL\_20120107.xml

TAGVALUE	NAME	DEFAULTVALUE	MINIMUMVALUE	MAXIMUMVALUE	VALUE	STATE
(0x0051,0x100f)	Coil	HEA,HEP	HEA,HEP	HEA,HEP	HEA,HEP	Success
(0x0018,0x0022)	Scan option	FS	FS	FS	FS	Success
(0x0051,0x100c)	Field of view	[1120,1120]	[1120,1120] ([1108,8,1108,8])	[1120,1120] ([1131,2,1131,2])	[1120,1120]	Success
(0x0018,0x1310)	Acquisition matrix	[64,0,0,64]	[64,0,0,64]	[64,0,0,64]	[64,0,0,64]	Success
(0x0051,0x100b)	Reconstruction matrix	[64,64]	[64,64]	[64,64]	[64,64]	Success
(0x0018,0x005D)	Slice thickness	5	5	5	5	Success
(0x0018,0x0088)	Spacing between slices	6.0000000763896	5.94 (5.7)	6.06 (6.3)	5.999999792807	Success
(0x0019,0x100a)	Number of slices	20	20	20	20	Success
(0x0051,0x100e)	Acquisition orientation	Tra>Cor	Tra>Cor	Tra>Cor	Tra>Cor	Success
(0x0018,0x1312)	Phase encoding direction	COL	COL	COL	COL	Success
(0x0028,0x0030)	Pixel spacing	[3,5,3,5]	[3,46,3,46]	[3,54,3,54]	[3,5,3,5]	Success
(0x0018,0x0080)	Repetition time	4560	4514.4 (4332.0)	4605.6 (4788.0)	4560	Success
(0x0018,0x1314)	Flip angle	90	90	90	90	Success
(0x0018,0x0095)	Bandwidth	2520	2494.8 (2394.0)	2545.2 (2646.0)	2520	Success
(0x0018,0x0083)	Number of averages	1	1	1	1	Success
(0x0051,0x100ab)	Number of concatenations	1	1	1	1	Success
(0x0051,0x100a)	Acquisition duration	00:01	00:01	00:01	00:01	Success
(0x0051,0x1016a)	Correction B1	YES	YES	YES	YES	Success
(0x0051,0x1016b)	Correction distortions	NO	NO	NO	NO	Success
(0x0051,0x1011)	Parallel acquisition	P2	P2	P2	P2	Success
(0x0018,0x0094)	Percent phase FoV	100	100	100	100	Success
(0x0018,0x0093)	Percent sampling	100	100	100	100	Success
(0x0020,0x0105)	Time points	60	60	60	60	Success
(0x0018,0x0081)	Echo time	12	12	12	12	Success

**SEQUENCE PARAMETERS - PCASL\_S008**

manufacturer: Siemens  
 input directory: PCASL\_S008  
 /sit date: 20150907  
 dictionary: dico\_import3\_CENIR\_PCASL\_20120107.xml

TAGVALUE	NAME	DEFAULTVALUE	MINIMUMVALUE	MAXIMUMVALUE	VALUE	STATE
(0x0051,0x100f)	Coil	HEA,HEP	HEA,HEP	HEA,HEP	HEA,HEP	Success
(0x0018,0x0022)	Scan option	FS	FS	FS	FS	Success
(0x0051,0x100c)	Field of view	[1120,1120]	[1120,1120] ([1108,8,1108,8])	[1120,1120] ([1131,2,1131,2])	[1120,1120]	Success
(0x0018,0x1310)	Acquisition matrix	[64,0,0,64]	[64,0,0,64]	[64,0,0,64]	[64,0,0,64]	Success
(0x0051,0x100b)	Reconstruction matrix	[64,64]	[64,64]	[64,64]	[64,64]	Success
(0x0018,0x005D)	Slice thickness	5	5	5	5	Success
(0x0018,0x0088)	Spacing between slices	6.0000000763896	5.94 (5.7)	6.06 (6.3)	5.999999792807	Success
(0x0019,0x100a)	Number of slices	20	20	20	20	Success
(0x0051,0x100e)	Acquisition orientation	Tra>Cor	Tra>Cor	Tra>Cor	Tra>Cor	Success
(0x0018,0x1312)	Phase encoding direction	COL	COL	COL	COL	Success
(0x0028,0x0030)	Pixel spacing	[3,5,3,5]	[3,46,3,46]	[3,54,3,54]	[3,5,3,5]	Success
(0x0018,0x0080)	Repetition time	4560	4514.4 (4332.0)	4605.6 (4788.0)	4560	Success
(0x0018,0x1314)	Flip angle	90	90	90	90	Success
(0x0018,0x0095)	Bandwidth	2520	2494.8 (2394.0)	2545.2 (2646.0)	2520	Success
(0x0018,0x0083)	Number of averages	1	1	1	1	Success
(0x0051,0x100ab)	Number of concatenations	1	1	1	1	Success
(0x0051,0x100a)	Acquisition duration	00:01	00:01	00:01	00:01	Success
(0x0051,0x1016a)	Correction B1	YES	YES	YES	YES	Success
(0x0051,0x1016b)	Correction distortions	NO	NO	NO	NO	Success
(0x0051,0x1011)	Parallel acquisition	P2	P2	P2	P2	Success
(0x0018,0x0094)	Percent phase FoV	100	100	100	100	Success
(0x0018,0x0093)	Percent sampling	100	100	100	100	Success
(0x0020,0x0105)	Time points	60	60	60	60	Success
(0x0018,0x0081)	Echo time	12	12	12	12	Success

Figure 3.9: Graphical interface (*qualiCATI*) on which the review of the acquisition parameters is displayed.

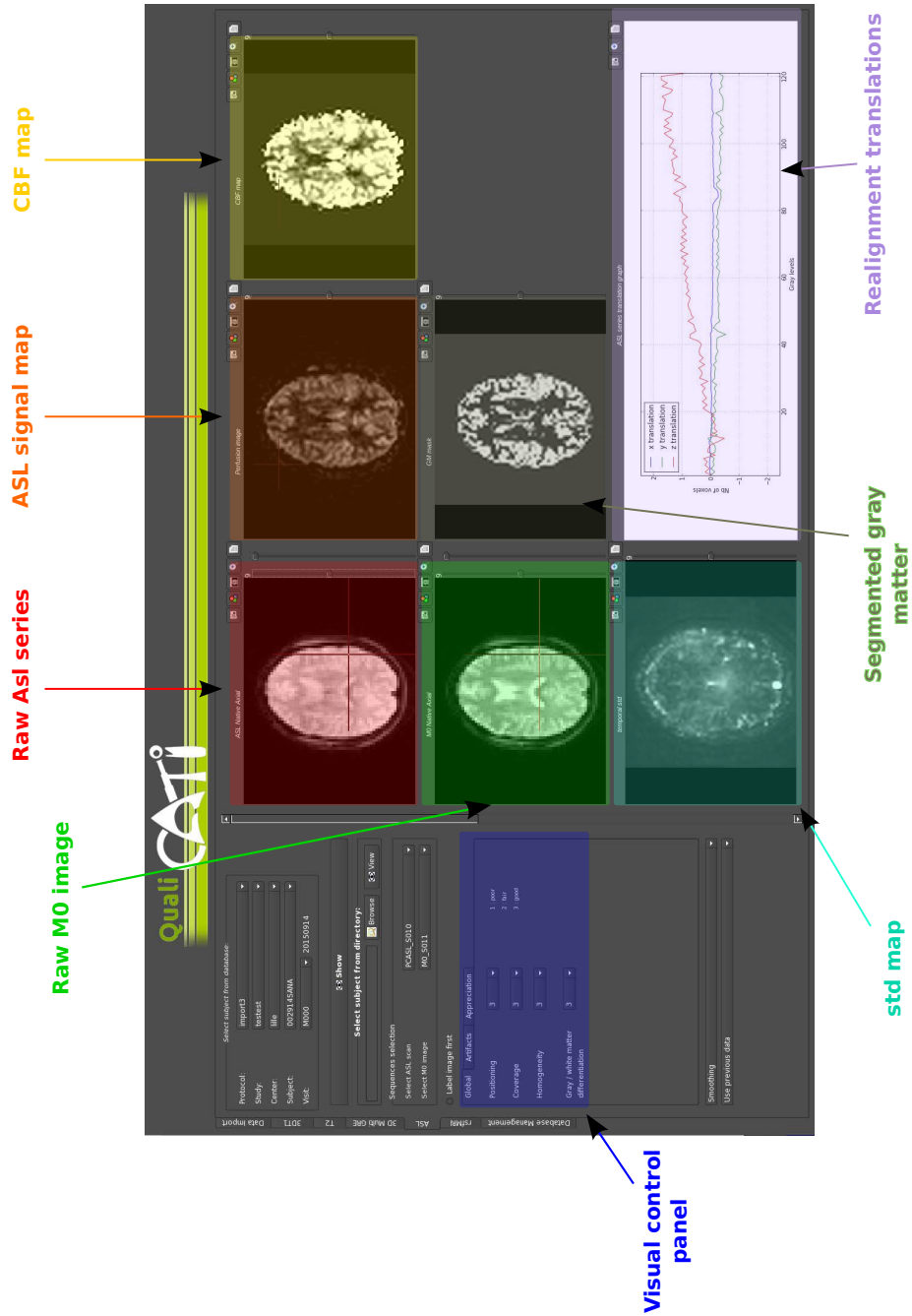


Figure 3.10: Graphical interface (*qualiCATI*) on which images necessary for the quality assessment are displayed.



On the third panel, global concerns about the ASL images quality are addressed. A global appreciation has to be provided, ranging from 1 (poor quality) to 4 (very good quality). A conclusion following the quality assessment procedure is also to formulate. The associated notes correspond to 0: reject scan (important problem concerning image acquisition in the emitting center), 1: ask the emitting center for a rescan, 2: mitigated evaluation (more information concerning quality problems should be provided as comments by the clinical research assistant), 3: scan acceptable for inclusion in the study and 4: scan of good quality to include in the study. A space dedicated to comments is also provided in this panel section.

These different criteria usually have to be filled by the clinical research assistant. Exceptions have been added in the case of strong artifacts, resulting in an automated filling of some criteria. If translations superior to 0.5 mm have been estimated during the realignment (and visible on the displayed graph), "Motion" is printed into the comments space, and the motion criterion automatically changed to 1. For translations superior to 2 mm, the motion criterion is changed to 2 and "Excessive motion" entered as a comment. In the case of very noisy ASL acquisitions, the normal classification consisting in gray matter CBF superior to brain CBF, superior to the white matter CBF can be affected. In that case, the mention "Wrong ROIs CBF order" appears in the comments space, ROI standing for region of interest.



Figure 3.11: Graphical interface (*qualiCATI*): sections constituting the visual quality control panel.

A document compiling the ranks affected to each criterion and the corresponding images is generated when the totality of the required fields are filled. A final score is calculated as the difference between the sum of the scores provided to the first section of the panel and the sum of the section concerning the artifacts. The objective of these document and score is to facilitate comparison between acquisitions. Such comparisons can occur when images are acquired on different scanners or between different exams of a same subject for example.

### 3.5 Discussion

The ASL sequences standardization work presented in this chapter allowed to include ASL acquisitions in the neuroimaging protocol of a study investigating relations between vascular risks factors and dementia. Since the beginning of inclusions, 191 patients have been scanned in 6 different centres, from which 7 could not be imaged by means of the ASL sequence. Table 3.4 presents the results of the scans quality evaluation performed by the clinical research assistants, using the quality assessment tool detailed in 3.4.2. From the 184 ASL acquisitions, 104 were considered as fully satisfactory, 59 of an acceptable quality to be integrated into the study, and 21 were rejected (11%). Since very few studies are sharing their rate of scans inclusion, it appears difficult to estimate if the rate that we obtain is satisfactory. But as a matter of comparison, and while these rates have been obtained on pediatric populations, under specific imaging conditions, studies reported rejection rates of about 25% after ASL images quality evaluations in [Tortora 2017] and [Boudes 2014].

Scanner	parameters ok	Very good	OK	Rejected
<i>Total</i>	<i>184</i>	<i>104</i>	<i>59</i>	<i>21</i>
Philips Achieva 3T	42	29	10	2
Siemens Verio 3T	28	13	13	2
Siemens Prisma 3T	31	14	11	6
Siemens Skyra 3T	33	13	16	5
Siemens Verio 3T	19	14	4	1
Philips Ingenia 3T	31	21	5	5

Table 3.4: Summary of the quality control performed on the ASL scans acquired in the context of a neuroimaging study.

Following this work on ASL acquisitions quality assessment and the idea of improving the reliability of ASL images analysis and quantitative evaluations, we chose to address some limitations specific to ASL acquisitions. A post-processing approach was developed, which is presented in the following parts of this document.



# Distortion correction

---

## Contents

---

<b>4.1</b>	<b>Introduction</b>	<b>56</b>
<b>4.2</b>	<b>Material and methods</b>	<b>57</b>
4.2.1	Healthy subjects dataset	57
4.2.2	Methods	57
<b>4.3</b>	<b>Results</b>	<b>58</b>
<b>4.4</b>	<b>Discussion</b>	<b>60</b>

---

## 4.1 Introduction

The aim of the work presented in this chapter is to quantitatively investigate the capability of different existing distortion correction methods to correct for susceptibility artifacts in ASL images. Indeed, as stated in 3.3.5, the use of fast readout approaches, such as echo planar imaging (EPI), results in the introduction of distortions in areas of important magnetic susceptibility differences, typically at tissue/air or tissue/bone interfaces. These distortions correspond to geometric deformations (compressions and dilations) and hypo/hyper-intensities introduced in the phase-encoding direction (PED).

In the case of EPI acquisitions, distortions are echo time (TE) dependent, and reducing this parameter to the minimal value achievable on the scanner can limit the impact of the artifacts. Partial Fourier acquisitions allow to reduce the TE, but at the cost of signal-to-noise ratio and spatial resolution. Multi-shot EPI is an other alternative, but associated with an increase of the acquisition time.

Several post-processing methods have thus been proposed in the literature to perform distortion corrections. Field maps can be used to calculate estimations of the voxel's displacement to apply in order to unwrap the distorted images [Jezzard 1995]. These maps are obtained by calculating the phase differences between two gradient echo images acquired with different TEs. The main disadvantage of this method is the important time needed to acquire the additional field maps. An other approach consists in acquiring an image with a reversed PED compared to the data to be corrected [Chang 1992, Morgan 2004, Andersson 2003, Ruthotto 2012, Ruthotto 2013, Voss 2006, Hedouin 2017]. Such methods are based on the assumption that images acquired with opposite PEDs contain artifacts in opposition in terms of spatial deformations and intensities modifications. Acquiring an additional EPI image is usually less time consuming than generating a field map, which is the principal advantage of this kind of techniques. This reversed-phase approach has been demonstrated in diffusion imaging [Ruthotto 2012, Voss 2006, Hedouin 2017], functional MRI [Embleton 2010], and dynamic susceptibility contrast [Vardal 2013]. It has also been applied to arterial spin labelling images [Madai 2016], for images acquired with a multi-TI PASL sequence associated with a 3D-GRASE readout approach. This study revealed that correcting the CBF and arterial arrival time (ATT) maps estimated from the acquired ASL data improved the comparability with reference images estimated from dynamic susceptibility contrast acquisitions, in the case of patients affected by steno-occlusive disease.

In this work, we focus on reversed-phase based distortion correction methods, that have shown to provide more reliable artifacts reduction than field maps based techniques [Hong 2015]. We propose to compare the method applied in [Madai 2016] to other methods available as parts of free neuroimage processing software packages, on a set of 2D multi-slice EPI pCASL images acquired in healthy subjects.

## 4.2 Material and methods

### 4.2.1 Healthy subjects dataset

Images were acquired in 5 healthy subjects (2 females, 3 male,  $22 \pm 1.58$  years old), by means of a 3T Siemens Verio scanner and a 32-channel head coil. Acquisitions consisted in a MPRAGE structural image (resolution:  $1 \times 1 \times 1 \text{ mm}^3$ ) [Mugler 1990], pCASL series (resolution:  $3.5 \times 3.5 \times 5 \text{ mm}^3$ , interslice gap: 1 mm, 30 control-label pairs, PLD: 1800 ms, LD: 1800ms, 20 slices, TE=12 ms), and equilibrium magnetization ( $M_0$ ) images (resolution:  $1 \times 1 \times 1 \text{ mm}^3$ , interslice gap: 1 mm, 5 repetitions, 20 slices, TE=12 ms). The pCASL series and  $M_0$  maps were acquired with an identical positioning of the acquisition box, and four phase encoding directions: A>>P, P>>A, R>>L and L>>R.

### 4.2.2 Methods

Three reversed-phase based distortion correction methods were applied to the data presented in the previous section. The TOPUP method [Andersson 2003], implemented in the FMRIB software library (FSL, [Smith 2004]), which is the method applied to ASL images in [Madai 2016], is compared to the hyperelastic susceptibility artefact correction (HySCO, [Ruthotto 2012, Ruthotto 2013]) method, available as a part of the statistical parametric mapping (SPM) toolbox [SPM 2006]. The third technique evaluated in the context of this study is the one proposed in [Hedouin 2017], which we will refer to as the block-matching (BM) distortion correction method, which is implemented in the Anima medical image processing open-source software.

All pCASL series were corrected by means of each of these three algorithms. The  $M_0$  maps acquired with the same and reversed PED were used in each case to estimate the voxels displacements to apply to correct for distortions. The estimated transformations were then applied to the raw ASL series and the  $M_0$  maps, before processing them by means of the pipeline described in 2.6.1 to obtain quantified CBF maps. We chose to apply the distortion correction methods on the raw data, and not on subtracted ASL or CBF images, following the assumption that distortions only appear along the PED. Therefore, we consider that these perturbations should be corrected before performing any motion correction, as it is the case in our ASL images processing pipeline.

The capability of each method to correct for distortions was then quantitatively estimated, by comparing the CBF maps obtained after correcting pCASL series acquired with reversed PED, following the idea that corrected images should be closer to each other than uncorrected distorted images. The correlation and the structural similarity index (SSIM) were calculated to this end. The corrected A>>P and L>>R acquired series were also compared, as done in [Hedouin 2017], in order to evaluate the capability of the algorithms to provide corrected images close to each other, even if acquired with perpendicular PED.

### 4.3 Results

Figures 4.1 and 4.2 present the correlation and SSIM values measured between CBF maps quantified from ASL series acquired with reversed phase encoding directions, and compared while uncorrected for distortions, corrected by means of the block-matching algorithm, and corrected by application of the TOPUP and HySCO methods. Graphs showing the measures calculated from the A>>P and L>>R acquired series are displayed in Figure 4.3.

These figures provide information about the fact that the HySCO method seems to perform more irregularly than the other distortion correction methods on ASL images. Indeed, increased correlations between CBF images estimated from HySCO corrected ASL series acquired following the A>>P / P>>A and A>>P / L>>R PED can be observed, compared to the values obtained after applying the other methods. But SSIM values inferior to those calculated from the uncorrected images are measured between CBF maps generated from the HySCO corrected A>>P / L>>R and R>>L / L>>R ASL series.

On the contrary, TOPUP and BM show to provide corrected images closer to each other in terms of correlation and SSIM in all tested cases. BM appears to perform slightly better than TOPUP, ANOVA and Tukey statistical analysis concluding to significant differences between both methods when comparing the CBF maps produced from the R>>L / L>>R and A>>P / L>>R corrected series ( $p < 0.05$ ).

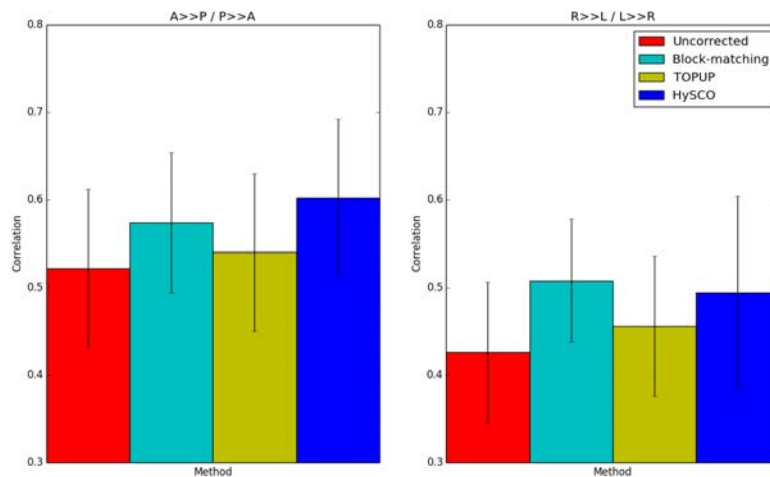


Figure 4.1: Healthy subjects: correlations measured between quantified CBF maps obtained from ASL series acquired with reversed phase encoding directions, and compared while uncorrected for distortions, corrected with the block-matching algorithm, TOPUP or HySCO (left: A>>P and P>>A, right: L>>R and R>>L).

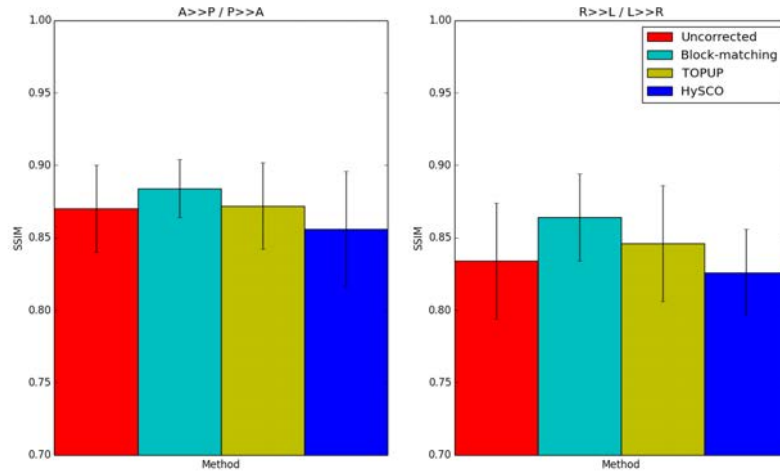


Figure 4.2: Healthy subjects: structural similarity index measured between quantified CBF maps obtained from ASL series acquired with reversed phase encoding directions, and compared while uncorrected for distortions, corrected with the block-matching algorithm, TOPUP or HySCO (left: A>>P and P>>A, right: L>>R and R>>L).

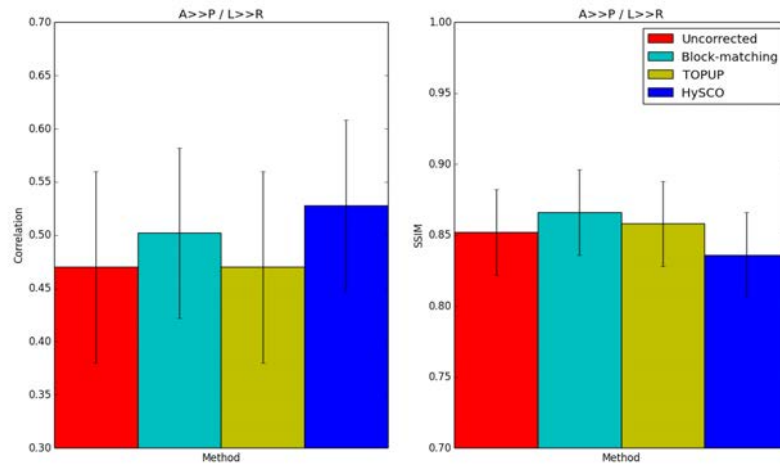


Figure 4.3: Healthy subjects: correlations (left) and structural similarity index (right) measured on quantified CBF maps obtained from ASL series acquired following the A>>P and L>>R phase encoding directions.



In figure 4.4, mean ASL signal maps images that correspond to scans acquired with both the A>>P and P>>A PED, as well as the A>>P images corrected by means of the three evaluated methods, are displayed. Figure 4.5 shows similar images, but corresponding to acquired L>>R, R>>L, and L>>R distortion corrected series. These images show slight performance differences between the evaluated methods regarding reconstructions of distorted areas. Differences can be observed between the borders obtained after reconstructing the A>>P PED acquired series, and appear to be a bit more important following the L>>R series distortion correction. Sharper structures can be seen on the ASL images generated after applying the BM method, which explains the higher SSIM obtained in figures 4.1, 4.2 and 4.3. In the contrary, the images corrected by means of the HySCO method appear slightly smoother than the other ones, which could give an explanation to the higher correlation and lower SSIM values identified in the graphs.

## 4.4 Discussion

Following the work of [Madai 2016], in which the TOPUP distortion correction method was the only one evaluated, we provided a comparison between three methods applied on 2D pCASL ASL series. This study outlines difficulties of the HySCO method to provide good reconstructions from ASL series acquired following each of the tested PED. TOPUP and the block-matching algorithm show to generate CBF maps estimated from reversed-phase ASL series closer to each other in each case, as well as when comparing data acquired with perpendicular PED. These aspects confirm the possibility to apply these methods to ASL data. In addition, the BM algorithm appears to perform slightly better than TOPUP in the context of this study.

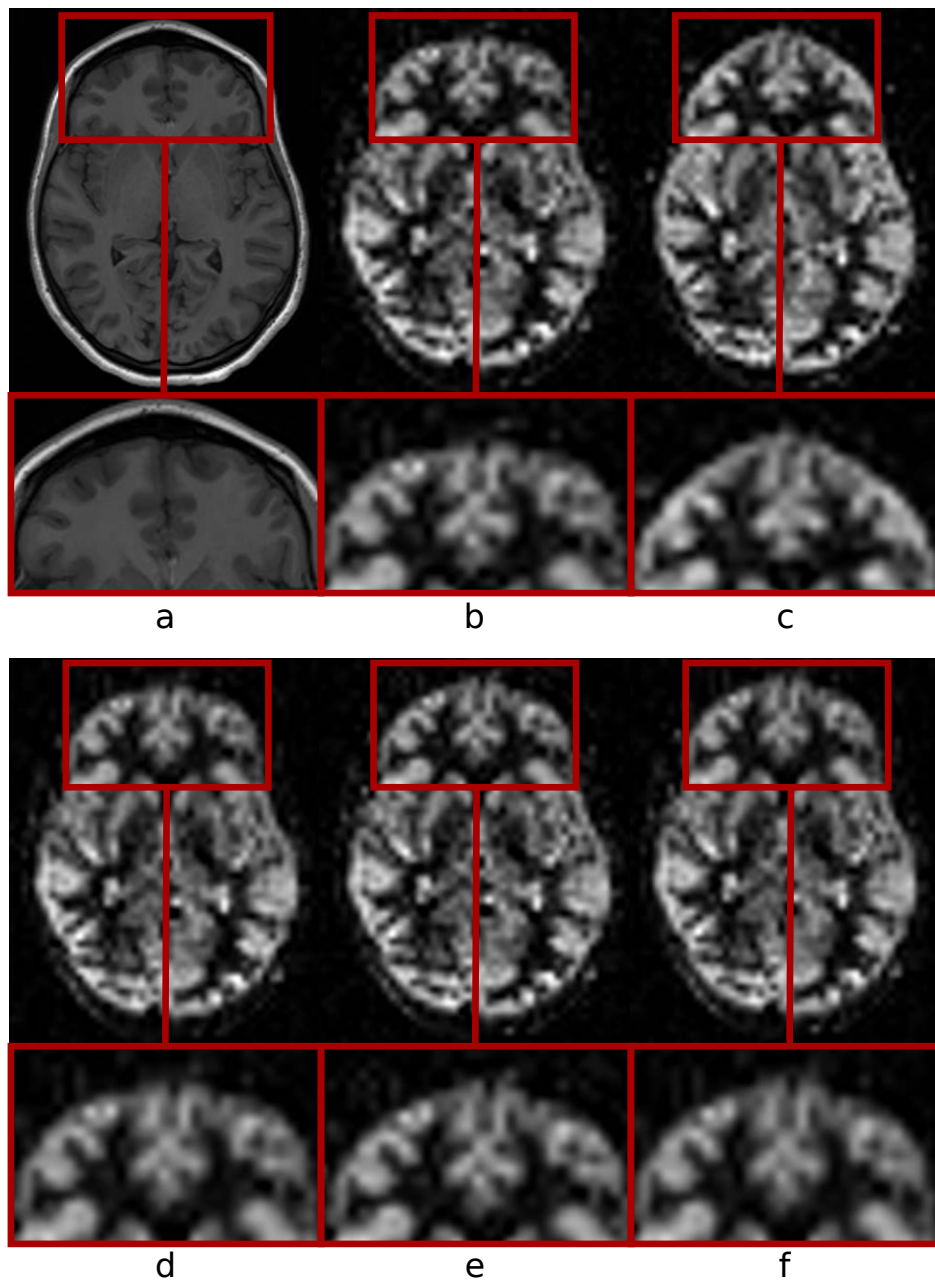


Figure 4.4: Images acquired on a healthy subject: a) structural images, b) mean ASL signal maps obtained from the ASL series acquired following the A>>P phase encoding direction, c) following the P>>A PED, d) after applying the block-matching distortion correction algorithm, e) after correction with the TOPUP method and f) after correction with the HySCO method.

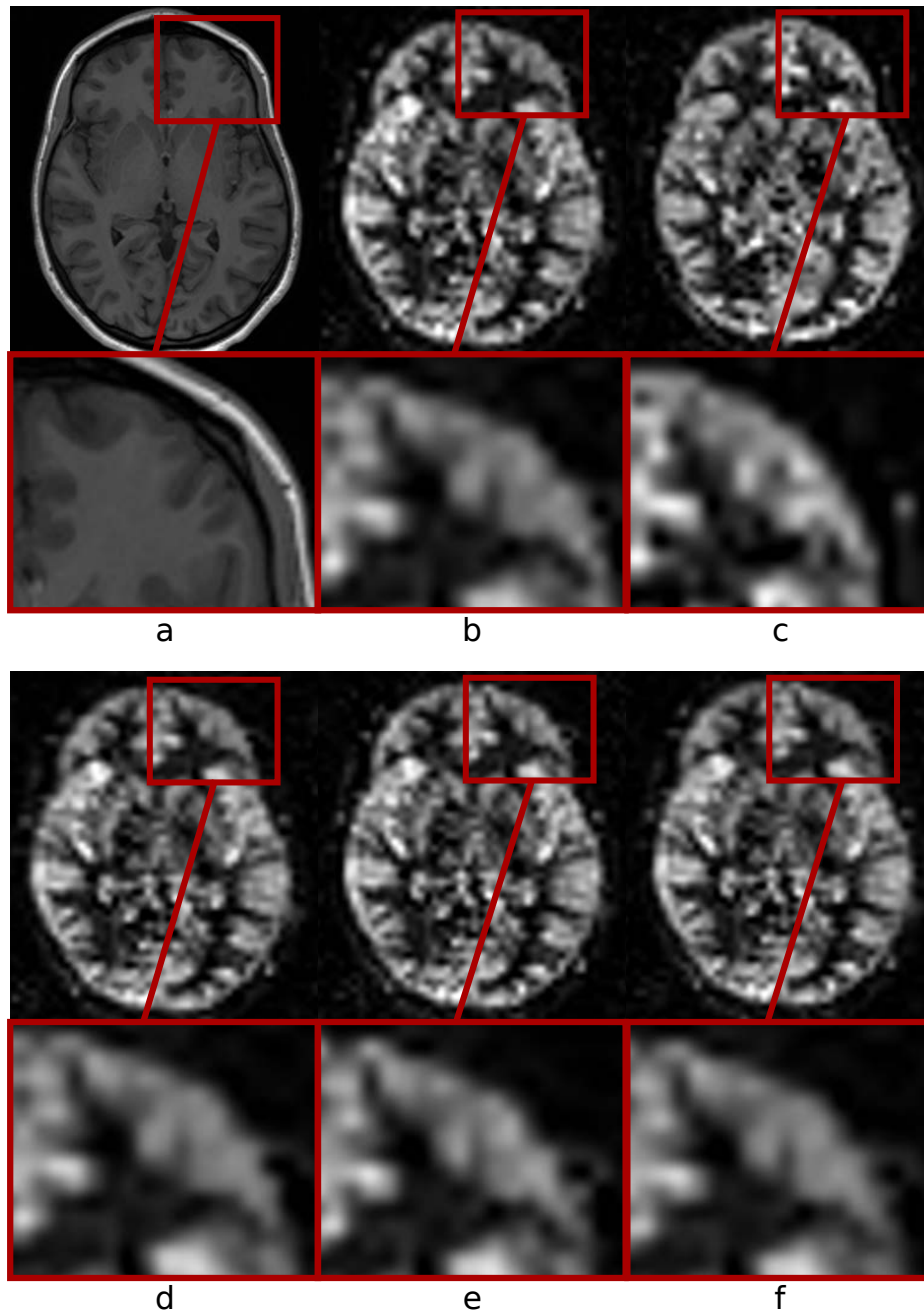


Figure 4.5: Images acquired on a healthy subject: a) structural images, b) mean ASL signal maps obtained from the ASL series acquired following the L>>R phase encoding direction, c) following the R>>L PED, d) after applying the block-matching distortion correction algorithm, e) after correction with the TOPUP method and f) after correction with the HySCO method.

## Part III

# Post-processing methods



# CBF maps super-resolution

---

## Contents

---

<b>5.1</b>	<b>Introduction</b>	<b>66</b>
<b>5.2</b>	<b>Materials and Methods</b>	<b>67</b>
5.2.1	Summary of existing similarity-based SR methods	67
5.2.2	A new SR method for ASL images	68
5.2.3	Validation framework	70
5.2.4	Implementation details	73
<b>5.3</b>	<b>Results</b>	<b>73</b>
5.3.1	Simulated dataset	73
5.3.2	Healthy controls	74
5.3.3	Comparison with DSC	75
<b>5.4</b>	<b>Comparison with Partial Volume Correction methods</b>	<b>76</b>
5.4.1	Method	76
5.4.2	Results	79
<b>5.5</b>	<b>Discussion</b>	<b>81</b>

---

## 5.1 Introduction

This part presents post-processing methods that have been developed and validated on different datasets in the context of this thesis.

Indeed, in addition to improvements provided in the field of hardware and image acquisition sequences, several post-processing algorithms have been proposed in the literature to address some limitations of ASL data. Particularly, denoising methods have been successfully applied to deal with artifacts and outliers in ASL images [Maumet 2014, Petr 2010b, Owen 2018]. Algorithms have also been proposed to correct for the low resolution of ASL images, and the fact that perfusion of different tissues contribute to the ASL signal observed in a single image voxel, which is commonly referred to as partial volume effects (PVE) [Asllani 2008, Chappell 2011, Petr 2010a]. These methods have in common to be applied at the resolution of the acquired images. While attenuating the effect of these corruptions, they do not allow to increase the level of details in images. However, this aspect could be of great interest, the thickness of gray matter (GM) being often inferior to the size of the ASL images voxel size. PVE can lead to diagnosis uncertainties, as for example in a voxel associated with a reduced ASL signal that can be explained by a real perfusion decrease or a structural gray matter atrophy. In clinical conditions, acquiring ASL images at higher resolutions is a challenging task, since this would imply a decrease in SNR, or increase the acquisition time.

Various methods have been proposed in order to increase the resolution of MR images facing similar low resolution properties, such as structural images [Manjón 2010, Rousseau 2010b, Rueda 2013, Shi 2015], quantitative  $T_1$  maps [Steenkiste 2016], diffusion MRI [Scherrer 2012, Coupé 2013] or spectroscopy [Jain 2017], as a post-processing step. Interpolation methods can be applied to MR data (trilinear interpolation, B-spline), unfortunately resulting in blurred images. To overcome this problem, super-resolution (SR) approaches allow to reconstruct high frequency information from low resolution data. Most of these methods are based on cost functions minimizations, that contain a term modeling the relation between the low resolution acquired images and the high resolution ones to reconstruct, and a regularization term, that constraints this ill-posed problem. Different forms of regularization terms are encountered in the literature, such as low rank and total variation constraints [Shi 2015], sparsity [Rueda 2013], and non-local patch-based similarity evaluations [Manjón 2010, Rousseau 2010b, Coupé 2013, Jain 2017]. Some of these methods are based on multiple low resolution acquisitions, therefore requiring specific acquisition protocols, which can be time consuming [Rousseau 2006, Rousseau 2010a, Scherrer 2012, Jia 2017]. Other methods rely on regularization terms that imply strong assumptions concerning properties of the high resolution reconstructed images. For example, methods based on total variation can generate reconstructed images smoother than realistic corresponding images.

Recent developments also led to the development of supervised super-resolution methods, based on overcomplete dictionaries [Rueda 2013] or deep learning approaches [Pham 2017, Chen 2018a, Chen 2018b]. While providing very promising

results on structural images, the lack of reference high resolution images makes such methods difficult to apply in the context of ASL acquisitions.

Regarding these aspects, the development of non-local patch-based SR approaches that are independent of the data acquisition process, and their adaptation to data commonly acquired in clinical conditions, such as T2-weighted, diffusion weighted or spectroscopy images, appears to be a solution that could be adapted to ASL images. The main idea consists in using self similarities in the images to perform reconstructions at higher resolutions [Protter 2009, Rousseau 2010b, Manjón 2010, Coupé 2013, Jain 2017]. Moreover, this approach prevents any increase in the acquisition time. The main limitation of these methods is that they require clean low resolution data as inputs, which means that denoising algorithms must first carefully be applied to the images prior to SR reconstruction.

In this chapter, we propose a novel method to increase the resolution of ASL images, which deals with the presence of noise. This non-local patch-based SR reconstruction approach is based on the assumption of appearing similarities between neighborhoods in the image that is reconstructed and a high resolution (HR) structural image, generally acquired in imaging protocols. This assumption of shared anatomical properties between structural and ASL images comes from the fact that gray matter and white matter are the two tissues that contribute to the brain ASL signal, with their own perfusion characteristics (e.g. CBF and arterial arrival time) [Asllani 2008, Chappell 2011, Petr 2010a]. This proposition allows to increase the resolution of ASL images without extending the acquisition time. The method is evaluated on a simulated dataset and images of healthy subjects in order to investigate its capacity to reconstruct images close to HR ASL references. As DSC is commonly considered to be a reference perfusion imaging technique, we investigate the ability of our method to generate images closer to the DSC quantitative maps from images acquired on subjects scanned for brain tumours. In addition, we investigate the influence of a recovery of HR details on PVE.

The material and methods are presented in section 5.2, results regarding comparisons between generated images and reference HR ASL or DSC maps in section 5.3, an evaluation of the influence of the SR reconstruction on PVE in section 5.4 and a discussion of these aspects in section 5.5.

## 5.2 Materials and Methods

### 5.2.1 Summary of existing similarity-based SR methods

The objective of super-resolution methods is to recover an unknown high resolution (HR) image  $x$  from a low resolution acquired one  $y$ . The following model explicits the relation between both images :

$$y = Mx + \eta, \quad (5.1)$$

with  $M$  a matrix representing subsampling, blurring and geometric transformations, and  $\eta$  representing some additive noise [Protter 2009, Rousseau 2010b,



[Manjón 2010, Coupé 2013, Jain 2017]. An optimization problem of the following form would correspond to a common approach to recover the unknown image  $x$ :

$$\tilde{X} = \arg \min_x \{ \|y - Mx\|_2^2 + \gamma \Phi(x) \}, \quad (5.2)$$

where  $\Phi$  is a regularization term necessary to solve this ill-posed minimization problem and  $\gamma$  a positive parameter.

As shown in [Manjón 2010], [Coupé 2013] and [Jain 2017], an iterative reconstruction-correction procedure can be adopted in order to reconstruct  $x$ , which allows to avoid problems such as local minima or parameters initialization linked to this ill-posed optimization problem. This procedure consists of two steps, corresponding to a reconstruction and a subsampling consistency constraint.

The reconstruction is based on the assumption that locations in a HR acquired structural image and the SR reconstructed one should share anatomical properties, and that the structural image could therefore be used to drive the reconstruction process. This assumption leads to the choice of non-local regularization approaches.

The subsampling consistency imposes the constraint of a strict equality between the downsampled version of the SR reconstructed image and the original low resolution image  $y$ , which is made possible by formulating strong assumptions about the  $M$  matrix composition. However, this constraint implies the need for well denoised low resolution images for the method to be consistent. Therefore, [Coupé 2013] proposed to apply a Rician-adapted denoising filter on diffusion images before solving the optimization problem.

In the case of low signal-to-noise ratio ASL images, different noise patterns can be introduced depending on the scanners, sequences or settings chosen to perform the acquisition. The use of parameters that could not be the most appropriate ones in the filtering step, potentially has important consequences regarding the quality of the final reconstructed image. This is the reason why we introduce a reconstruction driven by a HR structural image, while denoising the SR reconstructed image at the same time.

### 5.2.2 A new SR method for ASL images

The main objective of this work is to assess the relevance of using a HR anatomical image to increase the resolution of ASL images. Following a similar idea as [Rousseau 2010b], [Manjón 2010], [Coupé 2013] and [Jain 2017], we propose a non-local patch-based method, while introducing a novel denoising strategy.

Because of the use of non-local patch-based approaches, both in the denoising and SR methods previously described [Coupé 2013], we propose to combine them in a unique SR image reconstruction process. A third order B-spline interpolation is first applied to the low resolution image in order to increase its dimension to the desired one. This initialization is followed by iterations between a non-local patch-based regularization and a fidelity term assuring the global intensities mean consistency between the initial low resolution image and the reconstructed one.

This fidelity term differs from the one in use in the works presented in the previous section, in the sense that it involves a global image mean consistency, and not a subsampling consistency at the voxel level, therefore allowing a denoising of the reconstructed image.

The reconstruction term can be written as:

$$X_i^{n+1} = \frac{1}{Z_i} \sum_{j \in V_i} X_j^n w_{i,j}^n, \quad (5.3)$$

with  $X_i^n$  the intensity of voxel  $i$  in  $X^n$ , the reconstructed image at iteration  $n$ ,  $V_i$  a correspondence search volume around voxel  $i$ ,  $Z_i$  a scaling parameter, and  $w_{i,j}^n$  a weight accounting for the influence of the intensity of voxel  $j$  in this reconstruction step.

The correspondences between voxels' neighborhoods are assessed both in the reconstructed image and the structural one:

$$w_{i,j}^n = \exp - \left( \frac{\|N(X_{i,S}) - N(X_{j,S})\|_2^2}{\beta_{struct} \sigma_{i,S}^2} + \frac{\|N(X_i^n) - N(X_j^n)\|_2^2}{\beta_{asl} \sigma_i^2} \right), \quad (5.4)$$

$X_S$  represents the structural image,  $N(X_i)$  and  $N(X_{i,S})$  patches selected around voxel  $i$  in the ASL and structural images respectively,  $\sigma_i^2$  and  $\sigma_{i,S}^2$  are the empirical local variances, and  $\beta_{asl}$  and  $\beta_{struct}$  are two scalars adjusting the importance of the terms related to the ASL and structural images. The exponential weights, including an evaluation of the simultaneous similarity between voxel neighborhoods in the structural HR and reconstructed images, enable an increase in the level of details in the ASL image, while preserving features that are only visible in this image. Indeed, if neighborhoods are similar on two voxel locations in both images, the contribution in the regularization will be important. On the contrary, if a feature is only visible in one of the images, the weight will have a lower value, and have a reduced contribution in this process.

The global low resolution mean value consistency corresponds to an additive offset equal to the difference between the mean image value of  $X^n$  and the mean of the low resolution image  $Y$ , respectively  $\mu(X)$  and  $\mu(Y)$ :

$$X^{n'} = X^n + (\mu(Y) - \mu(X^n)). \quad (5.5)$$

Iterations between these two steps are performed until no significant difference between consecutive reconstructed images can be observed, which can be written as follows:

$$\frac{|X^{n-1} - X^{n-2}|}{|X^n - X^{n-1}|} < \tau. \quad (5.6)$$

As in [Coupé 2013], a coarse to fine approach is proposed where the weights  $\beta_{asl}$  and  $\beta_{struct}$  are decreased at each iteration of the process, leading to  $[\beta_{asl}, \beta_{asl}/2, \beta_{asl}/4, \dots]$  and  $[\beta_{struct}, \beta_{struct}/2, \beta_{struct}/4, \dots]$  respectively.

### 5.2.3 Validation framework

#### 5.2.3.1 Simulated dataset

In order to evaluate the proposed method in a controlled environment, we constructed a simulated set of 9 CBF maps. This dataset was built from structural (MP2RAGE UNI, [Marques 2010]) images acquired at a resolution of  $1 \times 1 \times 1 \text{ mm}^3$  with a 3T Siemens Verio scanner and a 32-channel head-coil. Fixed CBF values were considered for gray matter (GM) and white matter (WM), equal to 70 and 25 ml/100g/min respectively [Parkes 2004]. These values were affected to the probability maps obtained by means of the SPM12 segmentation algorithm [SPM 2006], leading to the application of the following equation:

$$\text{cbf}_i = p_{GM,i} \cdot 70 + p_{WM,i} \cdot 25, \quad (5.7)$$

with  $\text{cbf}_i$  the simulated CBF value at voxel  $i$ , and  $p_{GM,i}$  and  $p_{WM,i}$  the respective partial volume probability values for GM and WM provided by the segmentation at the same voxel location.

These HR simulated CBF maps were then downsampled to a resolution of  $2 \times 2 \times 2 \text{ mm}^3$  by applying a gaussian blurring before downscaling by a factor of 2 in the 3 directions. The downsampled images were then reconstructed at the original resolution using the proposed SR reconstruction method. In order to assess the influence of the ASL and structural related terms on the proposed reconstruction, implementations with different  $\beta_{asl}$  and  $\beta_{struct}$  values were evaluated. Images reconstructed by only taking the ASL or the structural related term into account were generated.  $\beta_{asl}$  and  $\beta_{struct}$  pairs equal to [0.25; 0.75], [0.5; 0.5] and [0.75; 0.25] were also evaluated.

Images reconstructed by means of nearest neighbor interpolation, trilinear interpolation and 3rd order B-spline interpolation were then generated and compared to the CBF maps reconstructed by means of the proposed method performed with the selected  $\beta_{asl}$  and  $\beta_{struct}$ .

The root mean square errors (RMSE) between the original HR simulated CBF maps and the reconstructed images were calculated in order to evaluate the ability of each method to provide reconstructed images close to this reference.

As ASL images acquired in clinical conditions are usually affected by noise, commonly considered as gaussian in CBF maps due to the averaging of multiple label-control pairs, we also studied the behavior of each of these methods as a function of the amount of noise. Downsampled images affected by gaussian noise with standard errors corresponding to 3 to 14% of the GM CBF value were reconstructed at the original resolution in order to evaluate this behavior. Figure 5.1 illustrates these image generation and processing steps.

#### 5.2.3.2 Healthy controls

The SR reconstruction method was also evaluated on images acquired on 4 healthy subjects (3 females, 1 male, age =  $34 \pm 6$  years). For each of these volunteers, images

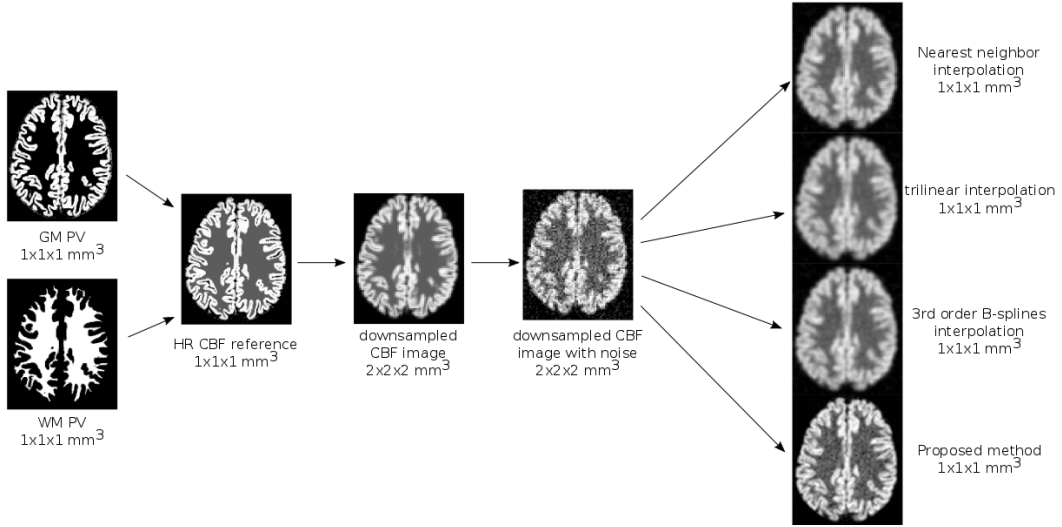


Figure 5.1: Pipeline describing the generation of the simulated dataset and the different reconstruction methods to be compared, applied to the downscaled and noise corrupted images.

were acquired on a 3T Siemens Verio scanner with a 32-channel head-coil. The structural image was a MP2RAGE UNI (resolution:  $1 \times 1 \times 1 \text{ mm}^3$ ). pCASL (resolution:  $3.5 \times 3.5 \times 5 \text{ mm}^3$ , interslice gap: 1 mm, 30 control-label pairs, PLD: 1800 ms, labeling duration (LD): 1800 ms, 20 slices [Wu 2007]) and  $M_0$  (resolution:  $3.5 \times 3.5 \times 5 \text{ mm}^3$ , interslice gap: 1 mm, 5 repetitions, 20 slices) images were acquired as the low resolution data used to generate the CBF maps to be reconstructed by increasing their dimensions by a factor of 2 in each direction. HR pCASL images were also acquired for the evaluation purpose (resolution:  $1.75 \times 1.75 \times 2.5 \text{ mm}^3$ , interslice gap: 0.5 mm, 100 control-label pairs, PLD: 1800 ms, LD: 1800 ms, 20 slices), as well as HR  $M_0$  (resolution:  $1.75 \times 1.75 \times 2.5 \text{ mm}^3$ , interslice gap: 0.5 mm, 10 repetitions, 20 slices). While not allowing to cover the entire brain, a number of 20 slices was selected for these HR acquisitions as a matter of acquisition time. Image SNR being proportional to voxel volume, 100 repetitions were acquired in order to generate the HR pCASL images. While not entirely compensating for the SNR decrease in comparison with the 30 repetitions low resolution acquisitions, this repetition number was chosen as a compromise between scan time (10 minutes), risk of subjects motion and SNR.

CBF maps were obtained by applying the general kinetic model for pCASL acquisitions [Buxton 1998]:

$$CBF = \frac{6000 \cdot \lambda \cdot \Delta M \cdot \exp\left(\frac{PLD}{T_{1,blood}}\right)}{2 \cdot \alpha \cdot T_{1,blood} \cdot M_0 \cdot \left(1 - \exp\left(-\frac{LD}{T_{1,blood}}\right)\right)}, \quad (5.8)$$

with  $\lambda$  the blood/brain partition coefficient of water ( $\lambda = 0.9$ ),  $\alpha$  the labeling

efficiency ( $\alpha = 0.85$ ),  $\Delta M$  the control-label signal difference, and  $T_{1,blood}$  the blood  $T_1$  relaxation time ( $T_{1,blood} : 1650$  ms).

As in the case of the simulated data, RMSE values between the reconstructed images generated by the different methods and the HR pCASL CBF map, considered as the reference, were calculated.

### 5.2.3.3 Correlation with DSC

As mentioned in the introduction, Dynamic Susceptibility Contrast (DSC) imaging is often considered as a standard perfusion MR imaging technique. A contrast agent, usually gadolinium-based, is injected to the subject and the induced susceptibility effects are imaged via T2\*-weighted acquisitions. In clinical conditions, this technique enables acquisitions at a higher resolution than ASL scans. Therefore, we studied the correlation between low resolution CBF maps obtained from pulsed ASL (PASL) images, the same images after an increase of the dimensions by a factor of 2 in each direction with different interpolation methods and the HR DSC CBF images.

The dataset contains images of 10 patients imaged for brain tumors (3 females, 7 males, age =  $63 \pm 13$  years, 5 grade IV tumors, 1 grade III, and 3 patients not showing hyper-perfusion signals after evaluation by an experienced neuroradiologist). Images were acquired on a 3T Siemens Verio scanner with a 32-channel head-coil. A 3D T1w sequence (resolution:  $1 \times 1 \times 1$  mm<sup>3</sup>) was acquired, as well as a PICORE Q2TIPS PASL sequence with flow crusher gradients (EPI readout, TR: 3000 ms, TE: 18 ms, FOV:  $192 \times 192$  mm<sup>2</sup>, flip angle:  $90^\circ$ , in plane resolution:  $3 \times 3$  mm<sup>2</sup>, slice thickness: 7 mm, interslice gap: 0.7 mm, inversion time ( $TI$ ): 1700 ms, bolus width ( $TI_1$ ): 700 ms, 30 control-label repetitions) and a DSC sequence (GRE EPI readout, TR: 1500 ms, TE: 300 ms, FOV:  $230 \times 230$  mm<sup>2</sup>, flip angle:  $90^\circ$ , in plane resolution:  $1.8 \times 1.8$  mm<sup>2</sup>, slice thickness: 4 mm, interslice gap: 1.2 mm, 100 measures).

CBF maps were generated from the DSC images by use of the MR manufacturer software. An arterial input function was manually chosen to calculate the DSC relative CBF on a voxel basis. The method in use is based on a singular value decomposition deconvolution, as described in [Østergaard 1996]. The general kinetic model for PASL acquisitions was applied to the ASL scans [Buxton 1998]:

$$CBF = \frac{6000 \cdot \lambda \cdot \Delta M \cdot \exp\left(\frac{TI}{T_{1,blood}}\right)}{2 \cdot \alpha \cdot TI_1 \cdot M_0}, \quad (5.9)$$

The other parameters are the same as in (5.8), except  $\alpha = 0.98$ .

Although linear correlation between ASL and DSC relative CBF has not been strictly demonstrated, in a first approximation as shown in [Warmuth 2003, Ma 2017, Knutsson 2010], we assume that positive correlations should be obtained between both estimations. Therefore, the Pearson correlation coefficients were calculated between the low resolution ASL CBF and the registered HR DSC CBF maps, and the SR reconstructed ASL CBF and DSC CBF maps.

### 5.2.4 Implementation details

An in-house image processing pipeline based on Python, Cython, Numpy [Gorgolewski 2011] and SPM12 functions was used to conduct the experiments. Considering results presented in [Coupé 2013] and our own experiments, the patch size was chosen equal to  $3 \times 3 \times 3$  voxels in the non-local patched-based regularization, and the search volume to  $7 \times 7 \times 7$  voxels.

## 5.3 Results

### 5.3.1 Simulated dataset

Figure 5.2 presents the mean RMSE values obtained between the high resolution simulated references and the images reconstructed by means of the proposed SR reconstruction method for noise levels equal to 3%, 6% and 9% of the GM CBF value. One can first notice that referring to only one of the ASL or structural images provides less satisfactory reconstructions. Indeed, taking only the ASL image into account does not allow to recover details absent from the downsampled CBF maps. In the contrary, a reconstruction only based on the structural image will not allow to consider and preserve CBF patterns only visible in the ASL image. One can then notice that the balance between  $\beta_{asl}$  and  $\beta_{struct}$  does not lead to significant differences when a low level of noise is added to the simulated CBF maps. However, differences in this balance have a higher influence on the quality of the reconstruction when dealing with images corrupted by a higher noise level. In the case of  $[\beta_{asl}; \beta_{struct}] = [0.25; 0.75]$ , the weights generated to perform the reconstruction are more governed by the ASL related term, which can explain the higher RMSE values obtained when the level of noise increases.  $[\beta_{asl}; \beta_{struct}] = [0.5; 0.5]$  and  $[0.75; 0.25]$  provide lower RMSE values when a realistic noise level is added to the images, and no significant difference between their RMSE distributions can be noted. Therefore, in the context of this work, we propose to keep an equal contribution of the ASL and structural related terms, meaning  $[\beta_{asl}; \beta_{struct}] = [0.5; 0.5]$ .

Images corresponding to reconstructions of a low resolution CBF map corrupted by gaussian noise with a standard deviation equal to 9% of the GM CBF value, which we qualitatively suppose being a close example to effective low resolution acquired images, are displayed in Figure 5.3. The images generated by use of interpolation techniques (nearest neighbor, trilinear and 3rd order B-spline interpolations) appear flattened, compared to the SR reconstructed map, which enables to recover sharp structures and edges. Table 5.1 confirms these observations, with lower mean RMSE values (in bold) calculated between the simulated reference images and the SR reconstructed ones than between the references and the interpolated images. In addition, the evolution of these RMSE values indicates that the more the standard deviation of noise increases, the closer to the reference the reconstructed image is in comparison with the interpolated images. This result is associated with the capability of the proposed method to denoise the images. Significant RMSE distribution

differences between the proposed reconstruction method and all interpolation techniques are found for levels of noise superior to 9% of the GM CBF value ( $p < 0.00111$  after Bonferroni correction for an  $\alpha$  level equal to 0.01), and are marked by asterisks in table 5.1.

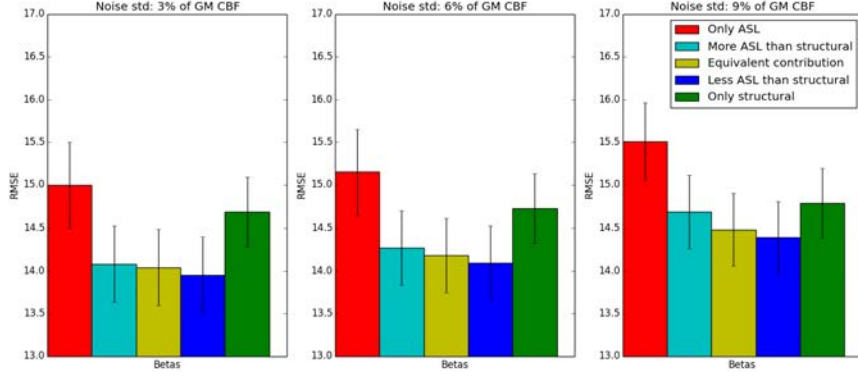


Figure 5.2: Graphs showing the RMSE values calculated between the reference HR image and images reconstructed with the proposed high resolution reconstruction method, by taking only the ASL,  $[\beta_{asl}; \beta_{struct}]$  equal to  $[0.25; 0.75]$  (more ASL than structural),  $[0.5; 0.5]$  (equivalent contribution),  $[0.75; 0.25]$  (less ASL than structural), or only the structural image into account. The displayed noise levels correspond to 3%, 6% and 9% of the GM CBF value.

Noise std	3	6	9	11	14
Nearest neighbor	14.82 ± 0.82*	15.3 ± 0.78*	16.31 ± 0.80*	17.72 ± 0.97*	19.98 ± 1.43*
Trilinear	14.80 ± 0.91*	14.93 ± 0.90*	15.22 ± 0.89*	15.66 ± 0.86*	16.38 ± 0.94*
B-spline	14.01 ± 0.89	14.35 ± 0.86	15.08 ± 0.83*	16.12 ± 0.85*	17.78 ± 1.19*
Proposed method	<b>13.92 ± 1.05</b>	<b>14.05 ± 1.04</b>	<b>14.34 ± 1.01</b>	<b>14.79 ± 0.99</b>	<b>15.56 ± 1.08</b>

Table 5.1: Means and standard deviations of the 9 RMSE values calculated between the reference HR image and the images reconstructed with nearest neighbor interpolation, trilinear interpolation, 3rd order B-spline interpolation and the proposed SR reconstruction method, with increasing levels of noise. Standard deviations of noise are expressed as percentage of the GM CBF value. Asterisks are joined to RMSE values corresponding to significant differences compared to the values obtained by application of the proposed method.

### 5.3.2 Healthy controls

Figures 5.4, and 5.5 present the images obtained from one of the 4 volunteers. Sagittal slices are shown, notably to insist on the influence of the methods on the

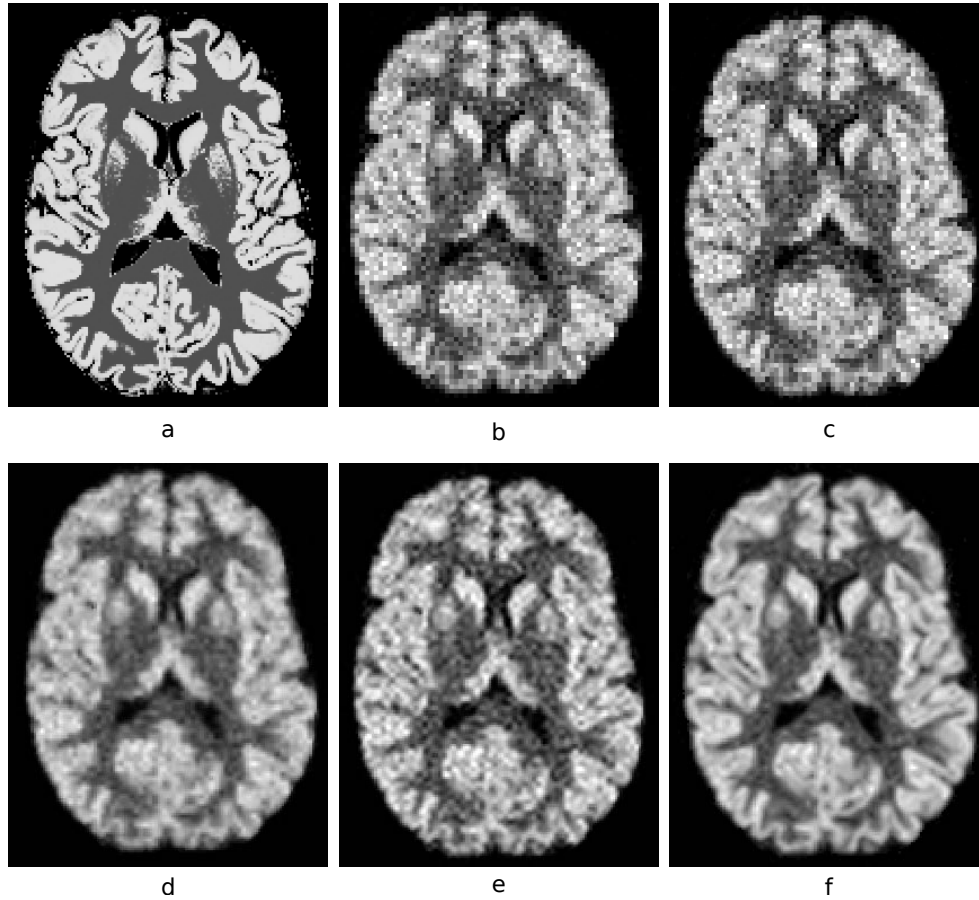


Figure 5.3: Simulated dataset: comparison of a) a HR reference image and b) the corresponding low resolution downsampled image corrupted by noise with  $\text{std}=9\%$  of the GM CBF value, c) nearest neighbor interpolation, d) trilinear interpolation, e) 3rd order B-spline interpolation, and f) proposed SR reconstruction.

staircase effect related to the particularly low initial resolution in the slice acquisition direction (5mm + 1mm gap). This effect is strongly corrected by the proposed SR reconstruction method. The RMSE values are reported in table 5.2, the proposed method providing images closer to the HR references than common interpolation techniques for three of the four subjects.

### 5.3.3 Comparison with DSC

Figure 5.6 reports, for each of the subjects, the values of the Pearson correlation coefficients obtained between the reference DSC CBF images and the low resolution acquired ASL CBF maps, their interpolations by trilinear and 3rd order B-spline and the images generated with the proposed SR reconstruction method. For each subject, the SR reconstructed image was more correlated to the DSC reference than the others. The significance of the differences was assessed by applying a



Method	Subject 1	Subject 2	Subject 3	Subject 4
Nearest neighbor	28.16	26.83	32.19	24.23
Trilinear	26.93	24.80	30.15	22.58
3rd order B-spline	<b>26.34</b>	25.04	29.68	22.49
Proposed method	26.44	<b>24.49</b>	<b>29.12</b>	<b>22.20</b>

Table 5.2: RMSE values calculated between the HR acquired reference image and the images generated by nearest neighbor interpolation, trilinear interpolation, 3rd order B-spline interpolation and the proposed SR reconstruction method, for each of the 4 healthy subjects (lowest RMSE value in bold for each subject).

Fisher transformation to the correlation coefficients. The p-values obtained after this transformation indicate a significant difference between the correlation coefficients distributions. Indeed, a paired t-test between the correlation values obtained for the proposed reconstructions and the low resolution acquisitions provided a p-value equal to  $1.4 \times 10^{-4}$ ,  $p = 8 \times 10^{-5}$  in comparison to the trilinear interpolation, and  $p = 3.33 \times 10^{-4}$  in comparison to the 3rd order B-spline. Figure 5.7 displays the DSC CBF images, low resolution ASL CBF maps and CBF maps reconstructed with our method for two of the patients.

## 5.4 Comparison with Partial Volume Correction methods

### 5.4.1 Method

Typical low resolution ASL acquisitions lead to well known PVE in ASL images, sometimes unfortunately preventing clinicians to interpret MRI observations such as reduced CBF values in regions of interest. Indeed, they could be the consequences of an effective reduced perfusion, a thinner GM or small subject motion. Because of the fact that the method described in this chapter enables the recovery of high frequency details that are not visible in low resolution acquisitions, we propose to evaluate the influence of this recovery on a potential reduction of PVE. This is of particular interest, since the PVE correction methods that are currently the most commonly applied to ASL images correct CBF values at the voxel level, thus not providing better detailed images. Moreover, the method that we present in this work is only dependent on the registration of a HR structural image to an interpolated ASL map, while classical PVE correction methods require the use of tissue partial volume estimates. These partial volume estimate maps are provided by segmentation algorithms, and are therefore subject to potential additional errors.

In order to compare the impact of these algorithms on PVE, a simulation was conducted from the same 9 structural images as presented in 5.2.3.1, in which we aimed at having the most possible information about intensity values. In order to construct these 9 HR ASL images in which we knew the exact voxel constitution and associated values, images containing 100% GM or WM voxels were created, by

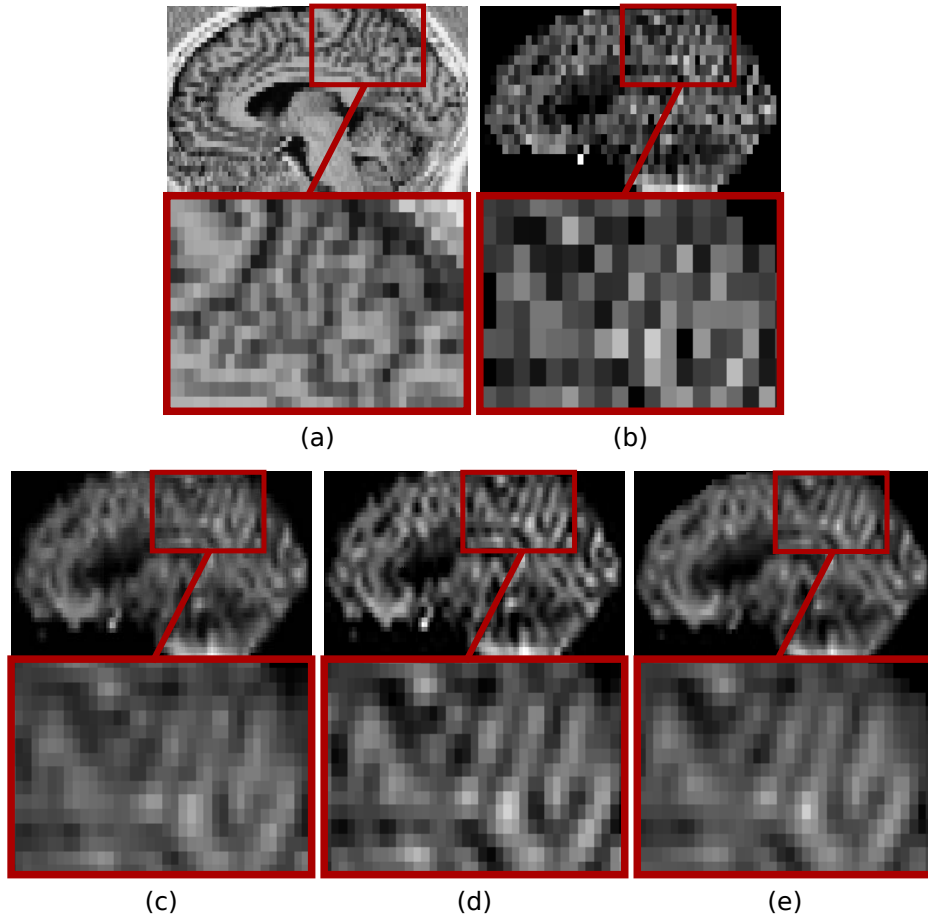


Figure 5.4: Healthy subject: sagittal slices of a) a structural image, b) the corresponding CBF map from the acquired low resolution pCASL, c) after trilinear interpolation, d) after 3rd order B-spline interpolation, and e) the proposed SR reconstructed CBF image. Upper lines: sagittal slices, bottom lines: zoom on the same slices.

thresholding the partial volume estimates generated by the SPM12 segmentation algorithm. Synthetic ASL signal maps were generated by affecting  $\Delta M$  values of 10 for GM and 1.5 for WM, with additional sinusoidal variations of 20% amplitude to make them more realistic, and evaluate the capability of the tested algorithms to preserve spatial variations and details [Zhao 2017]. The same process was used to create  $M_0$  images, with values of 1350 and 1000 in GM and WM respectively. These HR ASL signal and  $M_0$  maps were downsampled by averaging  $2 \times 2 \times 2$  voxel cubes, therefore reducing the size of the images and adding PVE, while knowing the exact brain tissue mixture of these new low resolution voxels. Different amount of gaussian noise (SNR=5,10) were added to these images in order to evaluate the influence of noise on PVE correction. The general kinetic model for pCASL acquisitions was then applied to obtain the corresponding CBF maps ( $\lambda = 0.9$ ,  $\alpha = 0.85$ ,  $T_{1,blood}=1650$  ms,

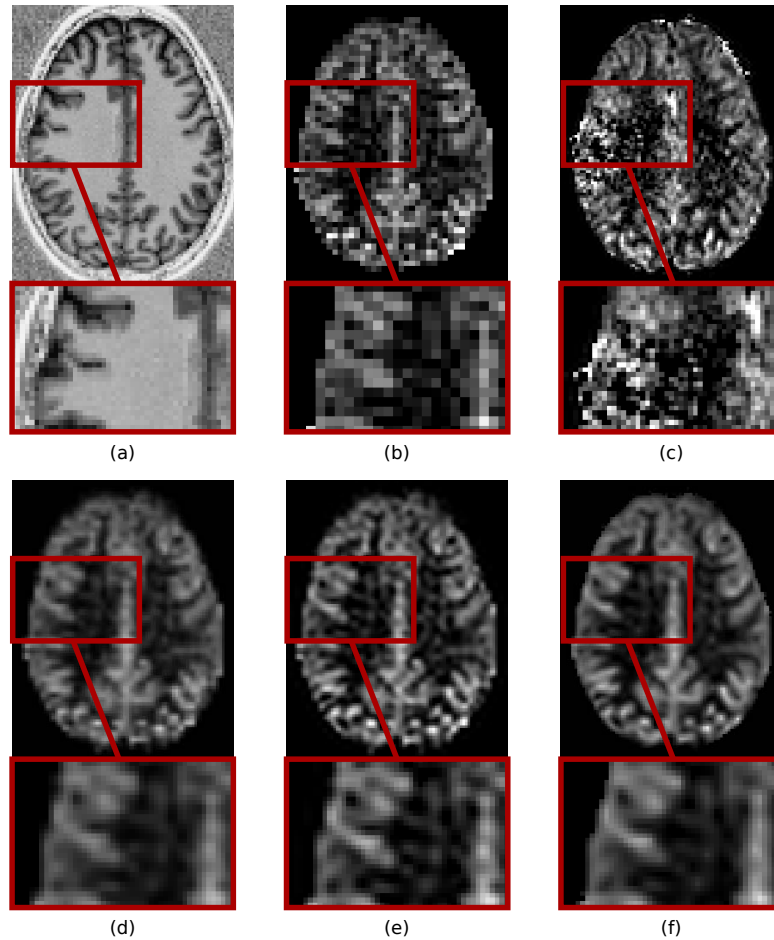


Figure 5.5: Healthy subject: axial slices of a) a structural image, b) the corresponding CBF map from the low resolution pCASL acquisition, c) the HR acquisition, d) after trilinear interpolation, e) after 3rd order B-spline interpolation, and f) the proposed SR reconstructed CBF image. Upper lines: sagittal slices, bottom lines: zoom on the same slices.

LD=1800 ms, PLD=1800 ms).

The effect of the proposed algorithm on PVE was evaluated by analyzing its ability to recover the effective GM contribution in the CBF values observed in each voxel, in comparison with the linear regression method, which is one of the standard PVE correction technique applied to ASL images [Asllani 2008].

Our proposed SR method provides high resolution CBF maps unlike the linear regression method, which produces two partial volume maps at the initial resolution. This is the reason why our SR CBF maps have been downsampled, in order to be able to compare the two results. The GM contributions in the CBF maps obtained by applying the general kinetic model to the HR ASL and M0 images, without noise, were considered as the references to which the generated images had to be compared. Figure 5.8 illustrates the pipeline that corresponds to the above-

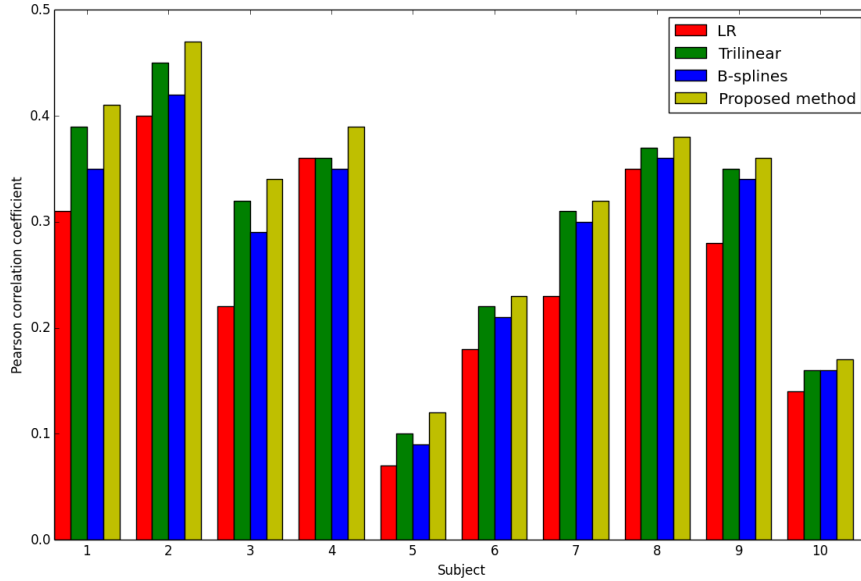


Figure 5.6: Pearson correlation coefficient between the reference DSC CBF maps and low resolution CBF images, the same images after trilinear interpolation, 3rd order B-spline interpolation and the proposed SR reconstruction method. These coefficients are presented for each of the 10 subjects.

mentioned operations.

### 5.4.2 Results

Contrary to differences in the produced GM contribution maps reported in [Zhao 2017], between an application of the linear regression to the calculated CBF map and to ASL and  $M_0$  images before the CBF calculation, our method did not show such significant differences while testing for the influence of this effect. Figure 5.9 presents the GM contributions to the CBF values in a reference image, their recovery by application of the linear regression method to the low resolution CBF map, by applying the same method to ASL and  $M_0$  images before CBF calculation, and after increasing the CBF image dimensions with our method. Figure 5.10 shows the difference images obtained after the subtraction of each of the produced images listed above and the corresponding reference. An important aspect illustrated in these difference images is the fact, already stated in [Asllani 2008, Chappell 2011, Petr 2010a, Zhao 2017], that the linear regression method implies a smoothing of the GM contributions. On the contrary, the sinusoidal variations are retained in the image originating from the proposed algorithm.

Table 5.3 presents the evolution of the mean RMSE values calculated between

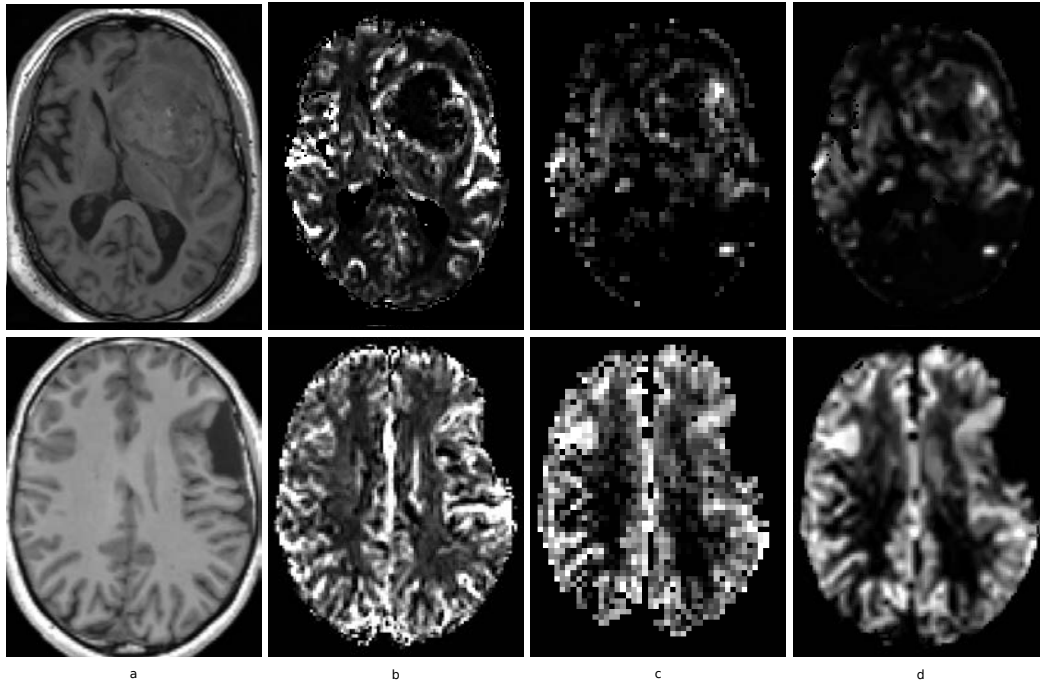


Figure 5.7: a) structural image, b) DSC CBF image, c) low resolution ASL CBF image and d) SR reconstructed ASL CBF map. The two lines correspond to images of two different subjects.

the generated GM contribution images and their references as a function of noise (SNR= $\infty$ , 10, 5). In practice, both applications of the linear regression method to the CBF maps or to the ASL and  $M_0$  images are commonly accepted [Zhao 2017]. Since the mean RMSE values obtained by applying our method to CBF maps are bounded by the mean RMSE provided by these two linear regressions, we can presume that our method reduces the influence of PVE.

Moreover, the linear regression method is based on the use of information provided by partial volume estimates, which makes it dependent upon the chosen segmentation algorithm and sensitive to potential segmentation errors. On the contrary, our SR reconstruction method is independent of any segmentation algorithm. In order to investigate the influence of these segmentation corruptions on the GM contribution maps resulting from the application of the linear regression, we simulated variations in the segmented partial volume estimates by introducing gaussian noise or by applying an opening and closing morphological operation to these partial volume maps. Tables 5.4 and 5.5 show a significant increase in the mean RMSE values when the partial volume estimates are modified. These results indicate that the property of the SR reconstruction to be independent of the use of partial volume estimates could be of great interest to avoid potential errors due to segmentation corruption.

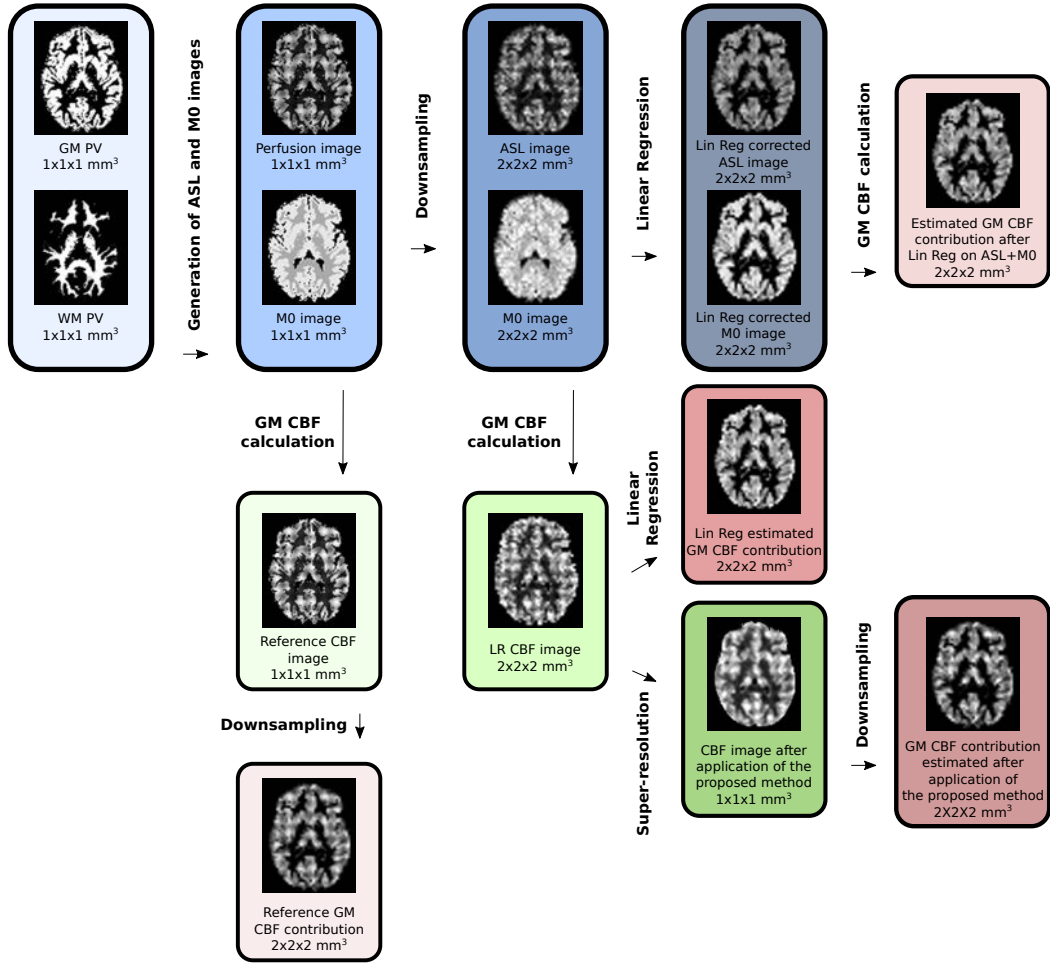


Figure 5.8: Pipeline describing the operations applied to each of the 9 images of the simulated dataset and the GM contribution assessment maps to be compared.

Method	SNR= $\infty$	SNR=10	SNR=5
Lin Reg on CBF	$6.41 \pm 0.74$	$6.54 \pm 0.75$	$7.05 \pm 0.75$
Lin Reg on Perf & M0	$4.39 \pm 0.17$	$4.52 \pm 0.17$	$4.90 \pm 0.17$
SR on CBF	$5.66 \pm 0.11$	$5.94 \pm 0.13$	$6.77 \pm 0.14$

Table 5.3: Mean RMSE values between the reference GM CBF contribution images and the images obtained after linear regression (Lin Reg) on the low resolution (LR) CBF image, Lin Reg on the ASL and M<sub>0</sub> images, and the proposed SR method applied to the LR CBF images.

## 5.5 Discussion

In this work, we have presented and investigated different properties of a SR reconstruction method dedicated to ASL images. This method enables to increase

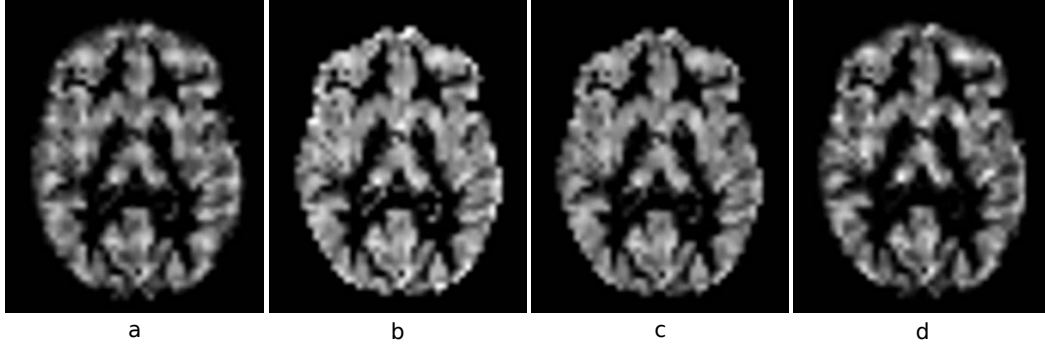


Figure 5.9: Comparison of gray matter cerebral blood flow contribution maps: a) GM contribution maps from the reference image, b) linear regression applied to the low resolution CBF image, c) linear regression applied to the low resolution ASL and  $M_0$  images, and d) proposed SR method applied to the LR CBF image (SNR=5).

Method	SNR= $\infty$	SNR=10	SNR=5
Lin Reg on CBF	$7.46 \pm 0.60$	$7.65 \pm 0.59$	$8.09 \pm 0.62$
Lin Reg on Perf & $M_0$	$5.84 \pm 0.23$	$5.97 \pm 0.24$	$6.24 \pm 0.22$
SR on CBF	$5.66 \pm 0.11$	$5.94 \pm 0.13$	$6.77 \pm 0.14$

Table 5.4: Mean RMSE values between the reference GM CBF contribution images and the images obtained after linear regression (Lin Reg) on the low resolution(LR) CBF image and on the ASL and  $M_0$  images, with noise added to the partial volume estimates needed by the Lin Reg method, and the proposed SR method applied to the LR CBF images.

Method	SNR= $\infty$	SNR=10	SNR=5
Lin Reg on CBF	$11.68 \pm 0.70$	$11.78 \pm 0.70$	$12.10 \pm 0.75$
Lin Reg on Perf & $M_0$	$11.19 \pm 0.50$	$11.23 \pm 0.49$	$11.42 \pm 0.51$
SR on CBF	$5.66 \pm 0.11$	$5.94 \pm 0.13$	$6.77 \pm 0.14$

Table 5.5: Mean RMSE values between the reference GM CBF contribution images and the images obtained after linear regression (Lin Reg) on the low resolution (LR) CBF image and on the ASL and  $M_0$  images, with an opening+closing operation added to the partial volume estimates needed by the Lin Reg method, and the proposed SR method applied to the LR CBF images.

the level of details, while providing a denoising of the reconstructed images. It is based on the assumptions of an appearing accordance between neighborhoods in the image to be reconstructed and a classically acquired HR anatomical image, and that distant neighborhoods could serve as a learning database in the reconstruction process.

On a simulated dataset, we have shown that the contributions of the ASL and

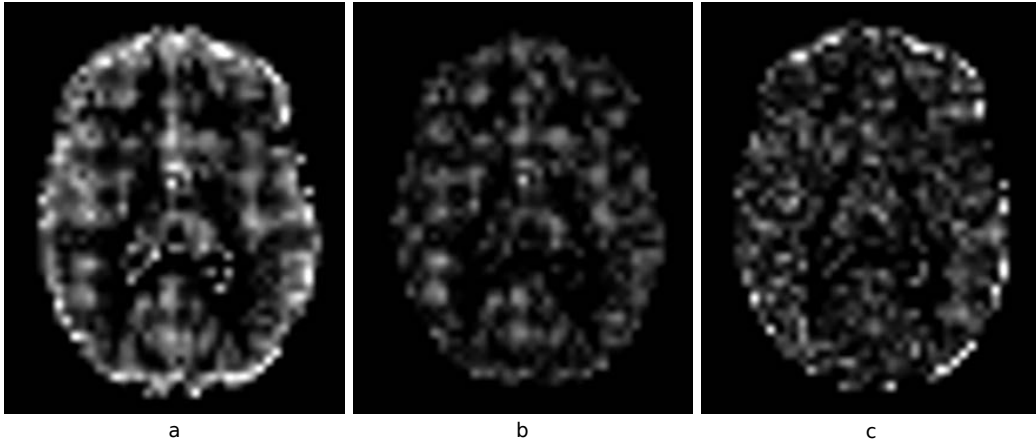


Figure 5.10: Comparison of gray matter cerebral blood flow contribution maps: a) difference images obtained by subtraction of the reference GM contribution map from the images obtained by applying the linear regression (Lin Reg) to the low resolution (LR) CBF image, b) the linear regression to the LR ASL and  $M_0$  images, and c) the proposed SR method to the LR CBF image (SNR=5).

structural related terms can be considered as equivalent in the reconstruction process, by selecting  $[\beta_{asl}; \beta_{struct}] = [0.5; 0.5]$ . Our method is also shown to provide images closer to references than common interpolation techniques. The fact that this result could be obtained with different levels of noise added to the images to be reconstructed is an indication of the ability of the proposed method to denoise the reconstructed images.

Experiments on low resolution data acquired on healthy subjects confirmed these findings in 3 out of 4 subjects. The main limitation of this study is nonetheless the relevance of the definition of the HR ASL images as references, because of their low SNR. In order to maintain the scan time reasonable and avoid subject motions that would almost certainly happen after 10 minutes of continuous scanning, 100 control-label repetitions have been acquired to generate the high resolution ASL images. This number is certainly still not sufficient to obtain an appropriate image quality, which could explain the fact that a better RMSE value was obtained by applying a 3<sup>rd</sup> order B-spline interpolation for the first subject. This limitation is precisely the reason why we chose to conduct the two other studies, meaning with a simulated dataset and the comparison with DSC images.

The study based on images of patients with brain tumors revealed a significantly increased correlation between DSC and images reconstructed with our method, supporting the capability of the proposed method to recover details by driving the reconstruction of ASL images with a high resolution structural one. The  $TI$  value chosen to acquire these PASL data was possibly a little short for subjects 5, 6 and 10, associated with intense ASL signals in their macrovasculature, which could explain



the reduced correlation values obtained for these three subjects.

We showed that our method associates an increase in the level of details with a reduction of the partial volume effect in ASL images. The main advantage of this SR reconstruction in comparison with the linear regression partial volume correction method is to preserve spatial signal fluctuations, which are smoothed by the latter.

Despite the three validation approaches that were addressed in the context of this work, we did not evaluate the method on pathologies implying subtle and localized perfusion changes. Investigating the capability of the method to preserve CBF modifications appearing prior to structural changes, as it is the case for early stages of neurodegenerative disease for example, would be of interest as a future work.

The method proposed in this chapter only depends on the accurate registration of a HR structural image to the initially interpolated ASL image to be reconstructed. Indeed, experiments revealed that the initial interpolation method selected in order to increase the dimension of the image to reconstruct does not have a significant influence on the generated image, and denoising is performed jointly with the increase in the level of details.

This aspect makes our method an appropriate tool to increase the quality and the fidelity of ASL images, and particularly CBF maps, with respect to effective physiological processes. Another promising aspect is its capability to recover well detailed ASL images from standard clinical acquisition protocols, therefore not increasing the acquisition time and patient discomfort. We believe that such a post-processing procedure could help clinicians to establish even more accurate diagnosis, by reducing interrogations concerning the reasons of reduced ASL signal and being able to distinguish GM thickness reduction or an effective ASL signal reduction for example.

This work is published in the form of a Neuroimage article [Meurée 2019].

A stay of one month within the Siemens Healthineers neuro applications development team, located in Erlangen, Germany, led to the inclusion of an ASL image super-resolution module in the *MR Arterial Spin Labeling Perfusion Analysis prototype*, as a *syngo.via* Frontier application ([www.siemens.com/syngo.via-frontier](http://www.siemens.com/syngo.via-frontier)).

# Multi-TI ASL super-resolution

---

## Contents

---

<b>6.1</b>	<b>Introduction</b>	<b>86</b>
<b>6.2</b>	<b>Material and methods</b>	<b>86</b>
6.2.1	Non-local spatio-temporal super-resolution method	86
6.2.2	Method evaluation	87
6.2.3	Implementation details	91
<b>6.3</b>	<b>Results</b>	<b>91</b>
6.3.1	Simulated dataset	91
6.3.2	Healthy subjects	92
<b>6.4</b>	<b>Discussion</b>	<b>99</b>

---

## 6.1 Introduction

As single-TI ASL images, multi-TI ASL data are subject to noise and partial volume effects. We present in this section a method, whose object is to address these limitations in a manner more appropriate to such acquisitions than the one proposed in chapter 5. An increase of the resolution of multi-TI ASL parameters estimation maps is achieved, while increasing the reliability of these estimations. This method is based on non-local similarities evaluations, performed by considering the temporal evolution of the ASL signal at neighboring locations, and driven by a high resolution structural image, as acquired in a majority of imaging protocols. The main difference between this method and the one proposed in chapter 5 is that the similarity between voxels in the ASL image series is assessed by means of their temporal evolution, instead of spatial similarities. The method and material are described in section 6.2, results obtained on a simulated dataset, as well as on data acquired on healthy subjects in section 6.3, and a discussion is provided in section 6.4.

## 6.2 Material and methods

### 6.2.1 Non-local spatio-temporal super-resolution method

In the context of this work, we propose to adapt the CBF maps reconstruction method presented in chapter 5 to the case of multi-TI ASL acquisitions. The objective is to recover an unknown ASL signal series,  $x_{t,t \in [0, \text{number of PLD}]}$  from a low resolution acquired one  $y_{t,t \in [0, \text{number of PLD}]}$ . The relation between images of both series can be written as:

$$y_t = Mx_t + \eta_t, \quad (6.1)$$

with  $M$  a matrix corresponding to blurring, subsampling and geometric transformations, and  $\eta$  additive gaussian noise. As previously shown, the ill-posed problem corresponding to recover the  $x_t$  from the  $y_t$  can be solved by iterating between reconstruction and correction operations of each ASL signal map,  $y_t$ , of the time series.

The dimension of each ASL signal map of the time series is first increased by applying a 3rd order B-spline interpolation. The work concentrating on CBF maps reconstructions only considered spatial information in the implementation of the super-resolution algorithm, based on the assumption of shared anatomical properties between a high resolution structural image and the ASL image to be reconstructed. We propose to extend this approach, and to add a non-local evaluation of temporal evolution similarities between neighboring voxels, based on the idea that voxels located close to each other should share similar temporal ASL signal evolutions.

Therefore, the reconstruction term can be written as:

$$X_{t,i}^{n+1} = \frac{1}{Z_i} \sum_{j \in V_i} X_{t,j}^n w_{i,j}^n, \quad (6.2)$$

with  $X_{t,i}^n$  the intensity of voxel  $i$  in the ASL signal map  $X_t^n$  corresponding to a given ASL image at iteration  $n$ ,  $V_i$  a correspondence search volume around voxel  $i$ ,  $Z_i$  a scaling parameter, and  $w_{i,j}^n$  a weight accounting for the influence of the intensity of voxel  $j$  in this reconstruction step:

$$w_{i,j}^n = \exp - \left( \frac{\|T_i^n - T_j^n\|_2^2}{\beta \sigma^2} + \frac{\|N_{i,S} - N_{j,S}\|_2^2}{\sigma_{i,S}^2} \right). \quad (6.3)$$

$T_i^n$  is a vector containing the intensities of voxel  $i$  at each acquired PLD,  $N_{i,S}$  a patch selected around voxel  $i$  in the structural image,  $\sigma^2$  the empirical variance calculated on the whole ASL signal time series,  $\sigma_{i,S}$  the empirical local variance calculated on the patch  $N_{i,S}$ , and  $\beta$  a scalar adjusting the influence of the ASL and structural related terms.

This expression is similar to the one presented in 5.4, but a term taking the temporal evolution of the ASL signal series into account substitutes for the spatial similarities evaluation. This weight enables to recover spatial details from the structural image in the ASL images, while preserving features that would only be visible in the ASL images and shared by voxels presenting similar temporal evolutions. In addition, taking these temporal evolutions into account allows to perform a denoising of the reconstructed temporal time series, outlier ASL signals being corrected to follow an evolution similar to that of neighboring voxels. A schematic description of this reconstruction process is provided in figure 6.1.

The correction term consists in ensuring that the global mean value of the ASL signal time series,  $\mu(\cdot)$ , remains constant:

$$X^{n+1} = X^n + (\mu(Y) - \mu(X^n)), \quad (6.4)$$

with  $X$  the high resolution time series being reconstructed and  $Y$  the acquired low resolution time series.

Reconstruction and correction are performed until convergence, and the weight  $\beta$  is divided at each reconstruction iteration, leading to  $[\beta, \beta/2, \beta/4, \dots]$ , as proposed in the previous method.

## 6.2.2 Method evaluation

### 6.2.2.1 Simulated dataset

A simulated dataset was constructed in order to evaluate the method. A structural image (MP2RAGE UNI, resolution:  $1.33 \times 1.33 \times 1.33 \text{ mm}^3$ ) was acquired on a Siemens Verio scanner with a 32-channel head coil. 70 and 25 ml/100g/min CBF values were attributed to gray and white matter partial volume maps obtained by segmenting the structural image using SPM12 respectively [SPM 2006], adding 8%

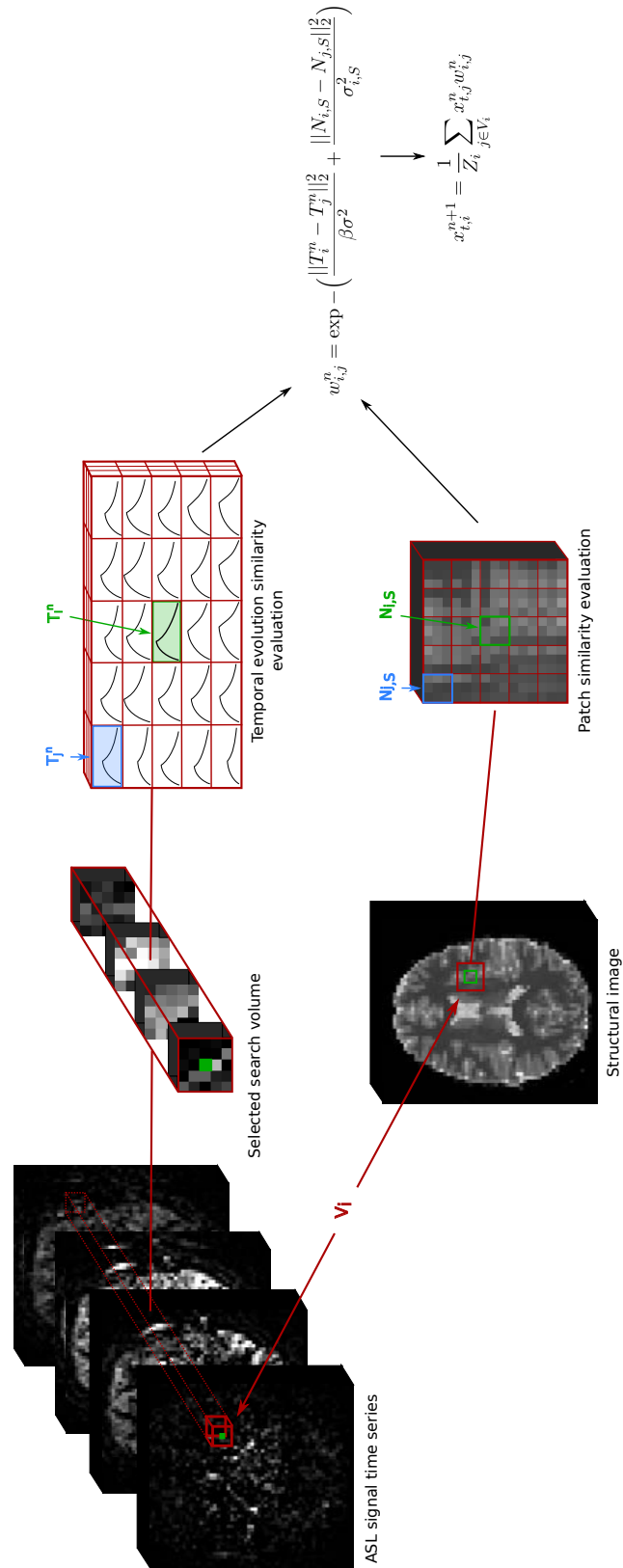


Figure 6.1: Schematic representation of the reconstruction performed in the proposed SR4D method.

amplitude sinusoidal variations in order to simulate a CBF map. An ATT map was obtained by applying a gaussian filter ( $\sigma = 2$ ) to an image from a multi-TI ASL acquisition performed on the same subject. These two maps were used to simulate an ideal ASL signal time series corresponding to ASL images that should have been acquired following the single compartment model at 12 different PLDs (500 ms to 4240 ms) [Buxton 1998]. Tissue  $T_1$  and equilibrium magnetization were fixed equal to 1300 ms and 1700 ms respectively as a matter of simplification. Each of the ASL images was downsampled by applying a gaussian blurring before downscaling by a factor of 2 in each direction. Noise with a standard deviation equal to the third of each low ASL signal map mean intensity value was added to 20 generated time series, simulating low resolution acquisitions.

In order to select the best  $\beta$  parameter, the 20 low resolution ASL time series were reconstructed by applying the proposed method (SR4D) with  $\beta = 1/2, 1/2^2, 1/2^3$ , and  $1/2^4$ . CBF and ATT maps were estimated from these reconstructed ASL time series, and compared to the original CBF and ATT maps by calculation of the peak signal-to-noise ratios (PSNR). The maps obtained by means of the  $\beta$  providing the highest PSNRs were compared to estimations generated by applying the three following methods in order to assess the proposed method contribution to the quality of reconstructions and estimations:

- (Splines) the CBF and ATT values were voxelwise estimated from the low resolution ASL series using non-linear least-squares fitting of the single compartment model. The estimated parameter maps were interpolated by means of  $3^{\text{rd}}$  order B-spline interpolations.
- (SR3D) the parameter maps are voxelwise estimated and reconstructed to higher dimensions by means of the algorithm presented in chapter 5, with  $\beta_{asl}$  and  $\beta_{struct}$  equal to 0.5.
- (SR3D MULTI) each of the ASL signal maps of each time series was reconstructed to the original dimension using the method presented in chapter 5, with  $\beta_{asl}$  and  $\beta_{struct}$  equal to 0.5. The CBF and ATT maps were voxelwise estimated from these reconstructed ASL images (cf figure 6.2).

### 6.2.2.2 Healthy subjects

The method was also evaluated on images acquired on 8 healthy subjects (6 females, 2 males,  $33 \pm 9$  years old). A structural image (MP2RAGE, resolution:  $1 \times 1 \times 1 \text{ mm}^3$ ), a prototype multi-TI pseudo-continuous ASL (pCASL) (3D GRASE readout, resolutions:  $3 \times 3 \times 3 \text{ mm}^3$  and  $6 \times 6 \times 6 \text{ mm}^3$ , 12 equally separated PLDs (500 ms to 4240 ms), labelling duration: 1800 ms), and 2 equilibrium magnetization  $M_0$  images (3D GRASE readout, resolutions:  $3 \times 3 \times 3 \text{ mm}^3$  and  $6 \times 6 \times 6 \text{ mm}^3$ ) were acquired. CBF and ATT maps were reconstructed at the high resolution from the lower resolution acquisition by means of the four methods described in 6.2.2.1.

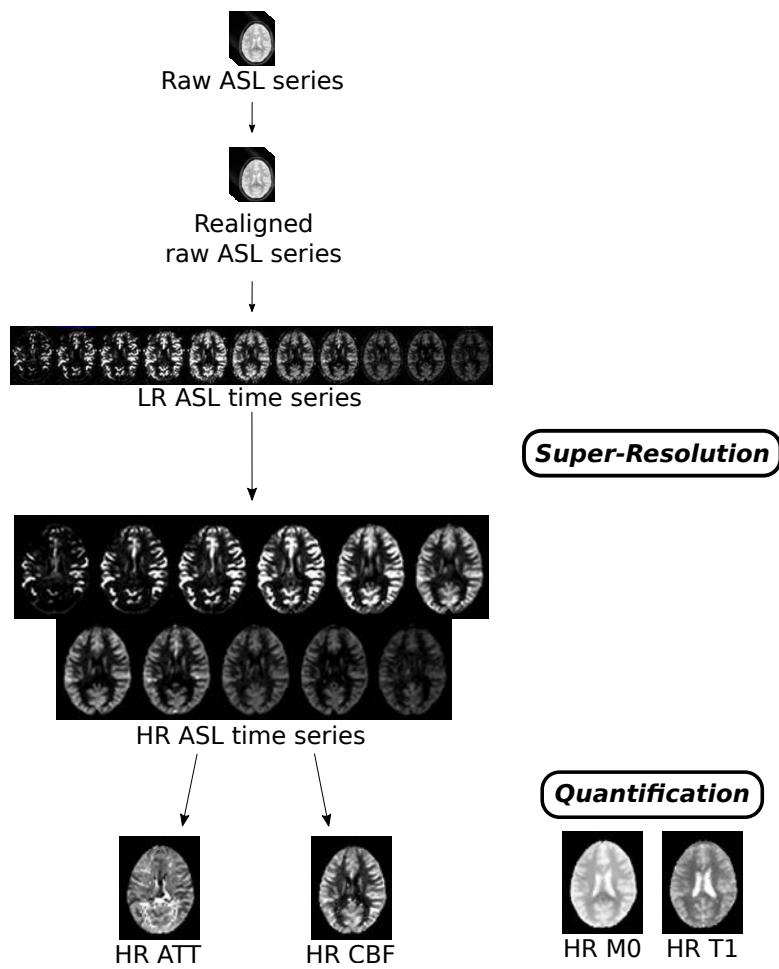


Figure 6.2: Schematic description of the SR3D MULTI method.

Tissue  $T_1$  and  $M_0$  maps were provided by the separate  $M_0$  and MP2RAGE  $T_1$  acquisitions in order to fit the single compartment model to the ASL series.

CBF and ATT could therefore be estimated from each of the ASL time series: the LR acquisitions, the HR acquisitions, the SR3D MULTI reconstructions and the proposed SR4D method. From these estimations, voxelwise theoretical ASL signal evolution curves were generated from these estimated CBF and ATT maps, that strictly match the single compartment model. The voxelwise correlation between these theoretical curves and the ASL signal evolutions of each of the evaluated time series was calculated on gray matter as a quantitative evaluation.

### 6.2.3 Implementation details

Similarly to chapter 5, the  $N_{i,S}$  patch size was chosen equal to  $3 \times 3 \times 3$  voxels, and the correspondence search volume to  $7 \times 7 \times 7$  voxels.

## 6.3 Results

### 6.3.1 Simulated dataset

The graph presented in figure 6.3 presents the PSNR values obtained with different  $\beta$  parameter values applied to the ASL related term during the reconstruction process.  $\beta = 1/2^2$  provides CBF and ATT maps closer to the original images (higher mean PSNR), and is therefore selected.

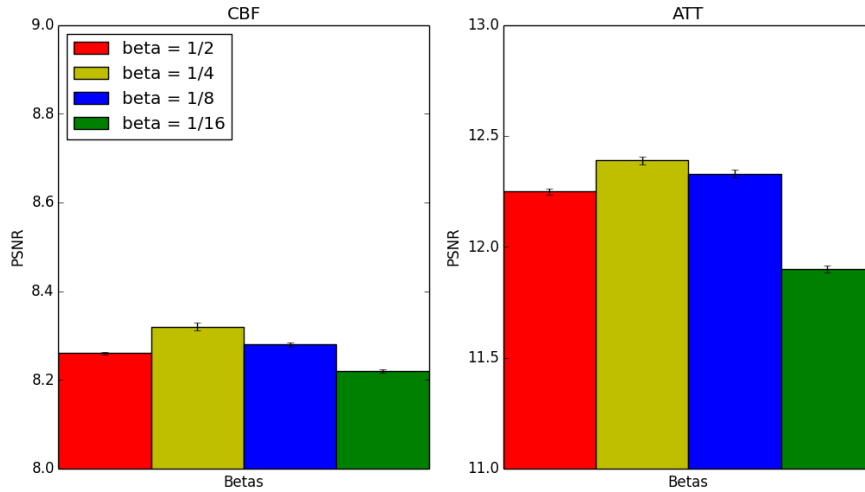


Figure 6.3: Simulated dataset: PSNR obtained by comparing reference CBF and ATT maps with the SR4D reconstructions obtained with different  $\beta$  parameter values.



Figure 6.4 reports higher mean PSNRs (in bold) in the case of the proposed SR4D method, than by performing the splines, the SR3D or the SR3D MULTI reconstructions. P-values following paired t-tests between the values calculated from the 20 corrupted downsampled ASL time series indicate a significant difference between the PSNR distributions ( $p < 10^{-22}$ ). Figures 6.5 and 6.6 present images from this simulated dataset. Of particular note is the noise pattern resulting from the corruption of the downsampled ASL time series, resulting in the introduction of outliers in the estimated maps. This noise is reduced in the image generated after applying the SR4D method, which can be explained by the faculty of this method to correct the reconstructed ASL series in the temporal domain. This aspect is visible on figure 6.7, showing the signal evolution of a voxel in the reference, 2 noisy low resolution and the 2 corresponding SR3D MULTI and SR4D reconstructed time series. Taking temporal similarities between neighboring voxels into account in the reconstruction step allows to recover an evolution closer to the one of the reference time series.

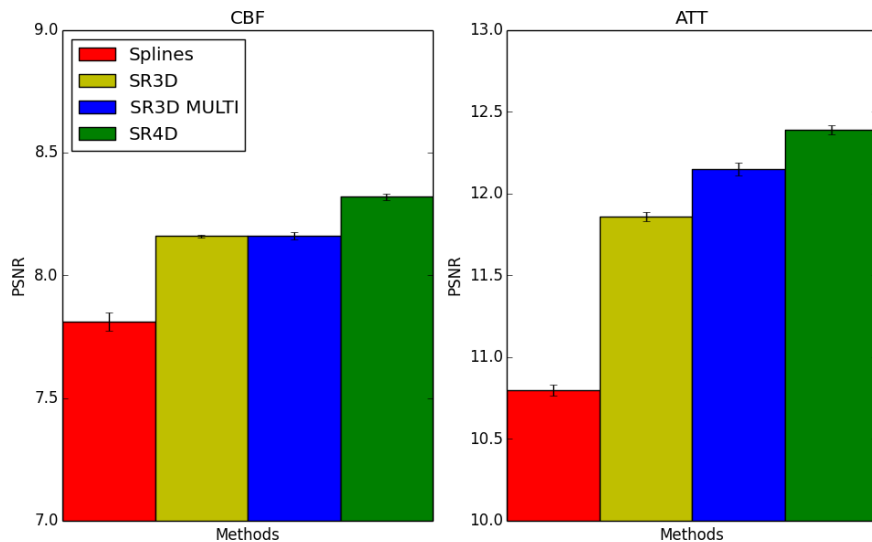


Figure 6.4: Simulated dataset: PSNR obtained by comparing reference CBF and ATT maps with the splines, SR3D, SR3D MULTI and SR4D reconstructions.

### 6.3.2 Healthy subjects

In figure 6.8, correlations between the theoretical curves matching the single compartment model and the low resolution, high resolution, SR3D MULTI and SR4D reconstructed ASL time series are reported. The series reconstructed by means of the proposed method are more correlated to the model than the others. This image

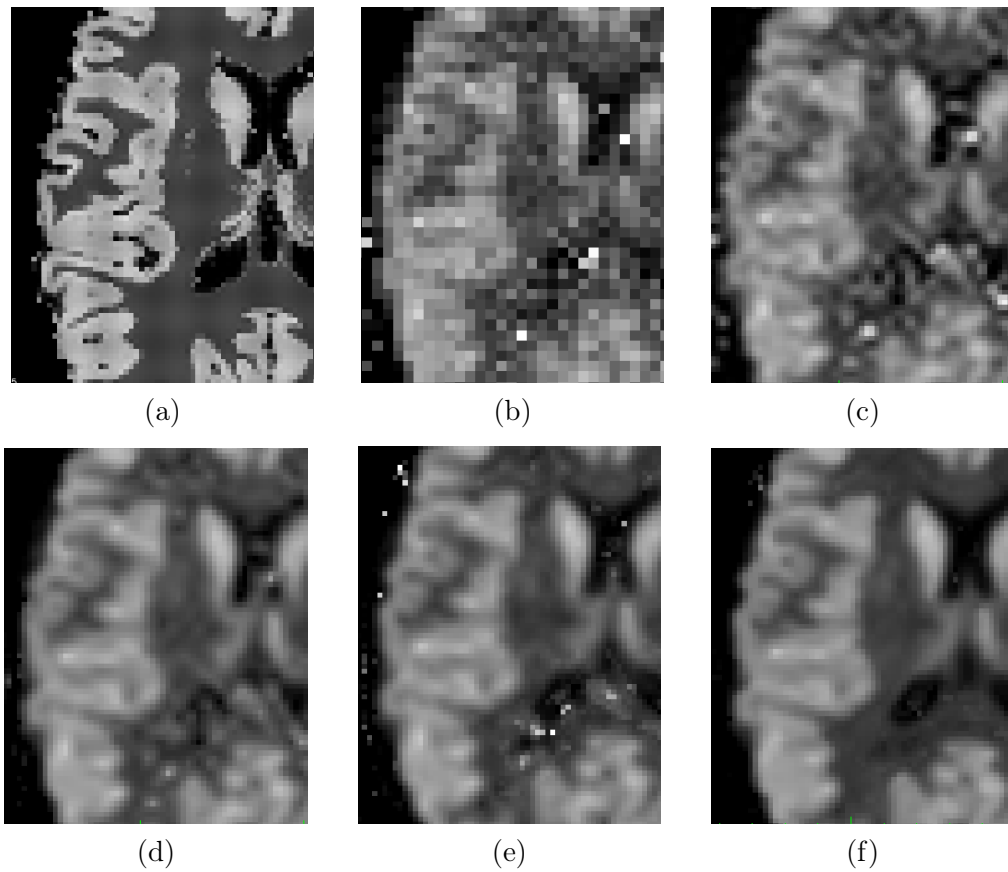


Figure 6.5: Simulated dataset: CBF maps from : a) the reference image, b) the CBF estimation from the noise corrupted downsampled series, c) the splines interpolation, d) the SR3D reconstruction, e) estimations from the SR3D MULTI and f) SR4D reconstructed ASL time series.

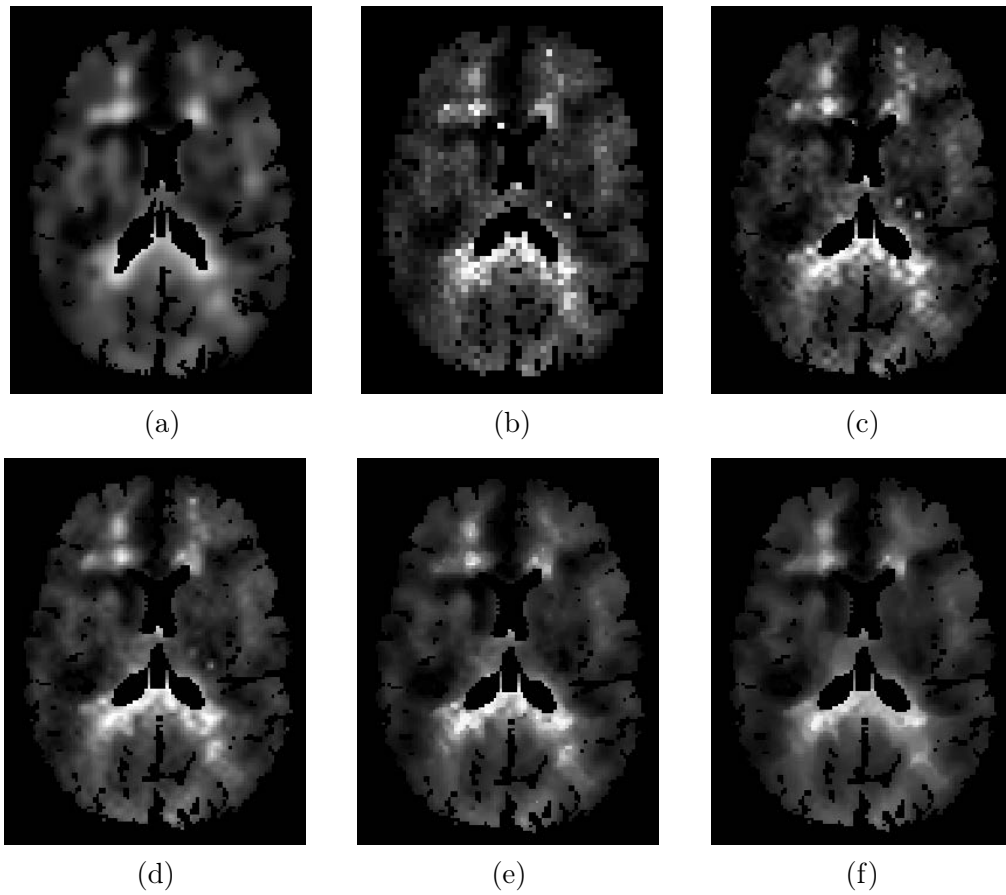


Figure 6.6: Simulated dataset: ATT maps from: a) the reference image, b) the ATT estimation from the noise corrupted downsampled series, c) the splines interpolation, d) the SR3D reconstruction, e) estimations from the SR3D MULTI and f) SR4D reconstructed ASL time series.

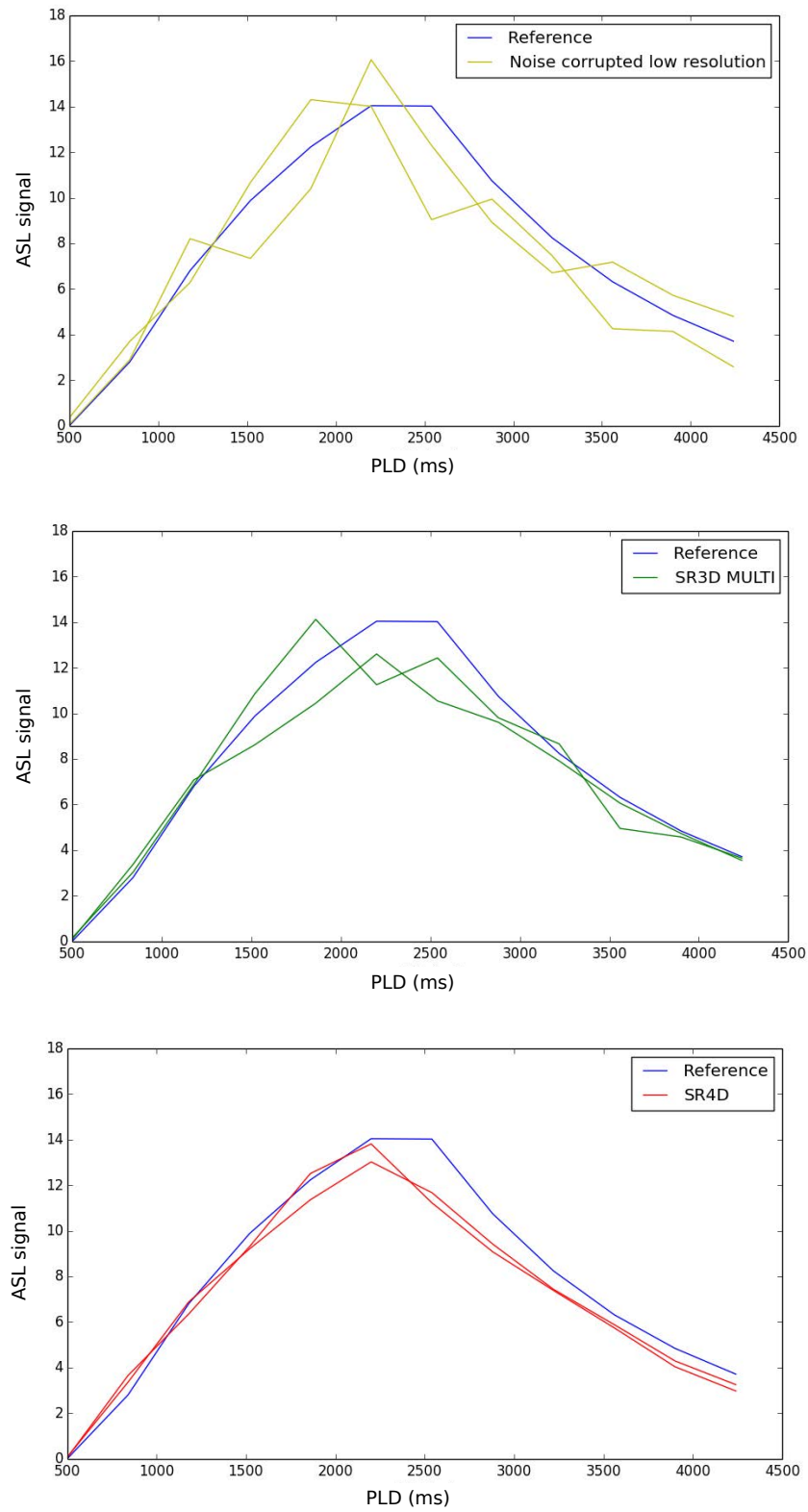


Figure 6.7: Simulated dataset: ASL signal temporal evolution of a voxel in the reference, 2 noisy low resolution and the 2 corresponding SR3D MULTI and SR4D reconstructed time series.

also outlines the fact that ASL signal time series associated with HR acquisitions are less correlated with the theoretical ASL signal evolution. The SNR reduction caused by the higher acquisition resolution can explain this result. The correlations obtained with the SR4D reconstruction are significantly higher than the ones calculated from the HR and the SR3D MULTI reconstructed ASL time series ( $p < 0.01$ ). The SR4D reconstruction is also associated with a significantly higher number of voxels that correspond to correlations with the theoretical curves superior to 0.5 ( $p < 10^{-4}$ ).

Figures 6.9, 6.10, 6.11 and 6.12 present examples of axial and sagittal slices of CBF and ATT maps obtained from the low resolution and high resolution acquisitions, the SR3D reconstructed maps, and the maps estimated after SR3D MULTI and SR4D ASL signal series reconstructions. The CBF slices that correspond to the SR4D reconstruction in figures 6.9 and 6.11 provide sharper details than the SR3D reconstructed map, and fewer outlier values, notably in white matter, than the image originating from the SR3D MULTI reconstruction. The SR4D method also reveals its capability to reduce the number of bright appearing points in the ATT images (figures 6.10 and 6.12). ATT patterns closer to the aspect of perfusion territories can be observed in the SR4D ATT map, associated with shorter ATT in areas close to arteries, and longer ATT in posterior and anterior areas. This result is in agreement with the assumption of ATT maps containing little high spatial resolution information, as formulated in [Dai 2011].

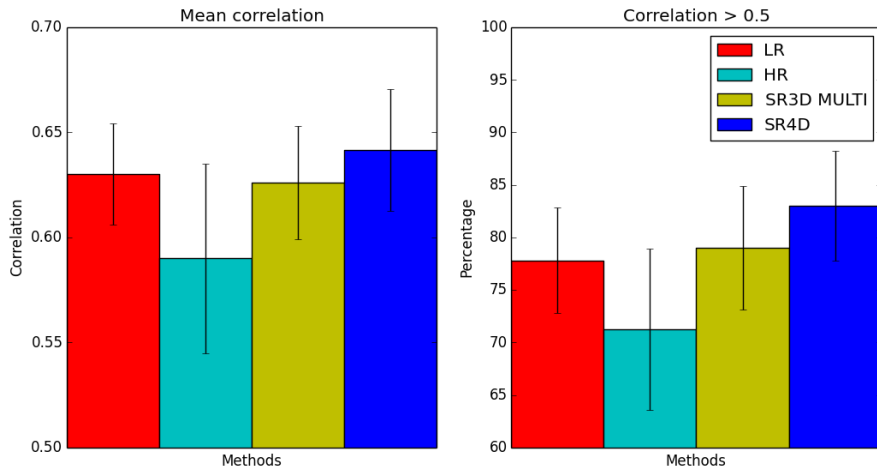


Figure 6.8: Healthy subjects: mean  $\pm$  standard deviation (std) and percentage of brain voxels with correlations to the single compartment model superior to 0.5 for the low resolution (LR), high resolution (HR), SR3D MULTI and proposed SR4D reconstructed ASL signal time series.

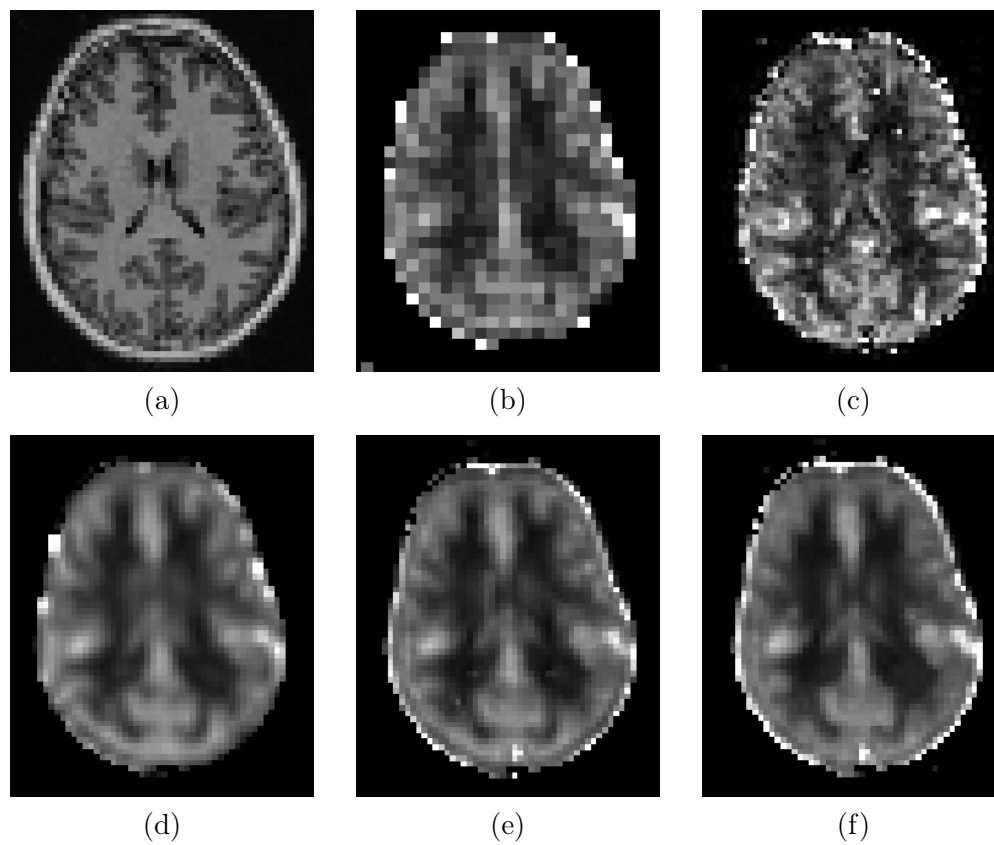


Figure 6.9: Images from one healthy subject: axial slices of a structural image (a), low resolution CBF map (b), high resolution CBF map (c), SR3D CBF map reconstruction (d), and CBF estimations from the SR3D MULTI (e) and SR4D (f) reconstructions.

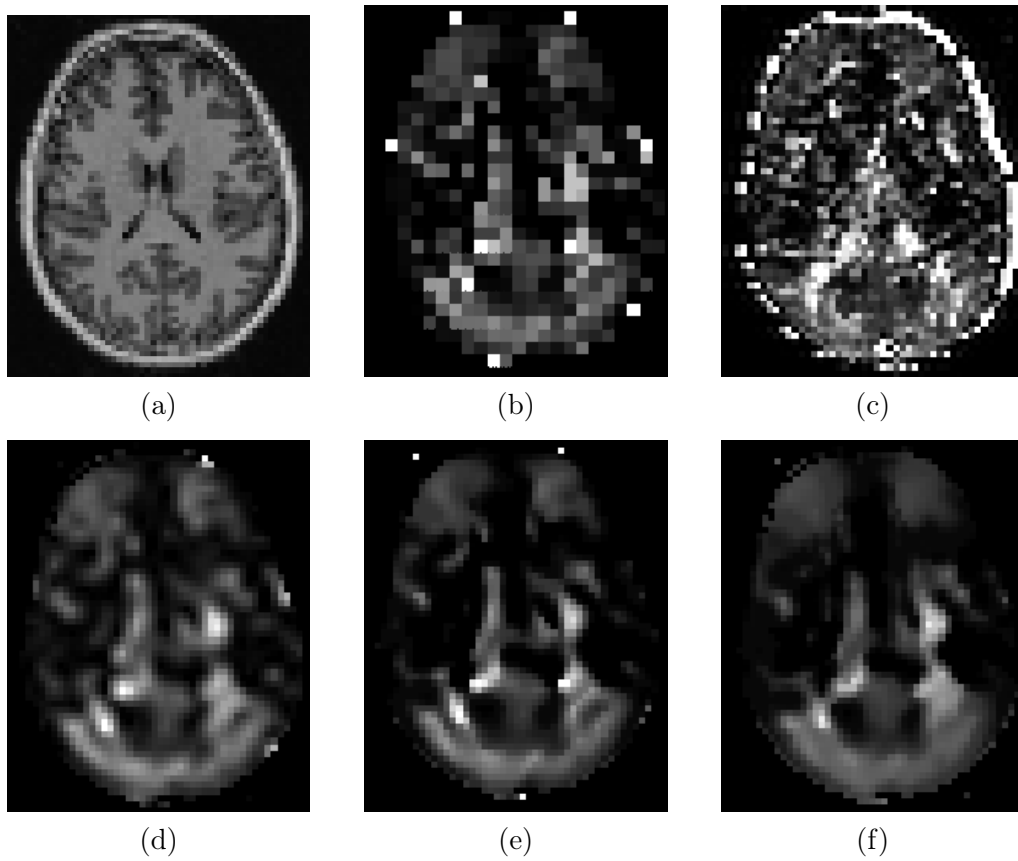


Figure 6.10: Images from one healthy subject: axial slices of a structural image (a), low resolution ATT map (b), high resolution ATT map (c), SR3D ATT map reconstruction (d), and ATT estimations from the SR3D MULTI (e) and SR4D (f) reconstructions.

## 6.4 Discussion

In this chapter, we have presented a new method extending the application of super-resolution to multi-TI ASL sequences. This non-local method based on the evaluation of similarities in the temporal evolution of neighboring voxel intensities, and driven by a high resolution structural image, shows to improve the reliability of images reconstruction and the estimation of parameters at increased resolutions, compared to the application of super-resolution methods only taking spatial similarities into account.

This aspect has been evaluated on a simulated dataset and on images acquired on healthy subjects. A difficult aspect of this work is the lack of high resolution reference in the case of the healthy subject study. Indeed, SNR being proportional to voxel volume, increasing the acquisition resolution considerably decreases images SNR, as shown in figures 6.9, 6.10, 6.11 and 6.12. Therefore, considering a high resolution CBF image as a reliable reference to which generated images could be compared is difficult.

Similarly to chapter 5, an evaluation of the method on data acquired on patients presenting slight CBF modifications, and no visible abnormalities in the structural image, such as in the case of an early stage of a neurodegenerative disease, would be interesting.



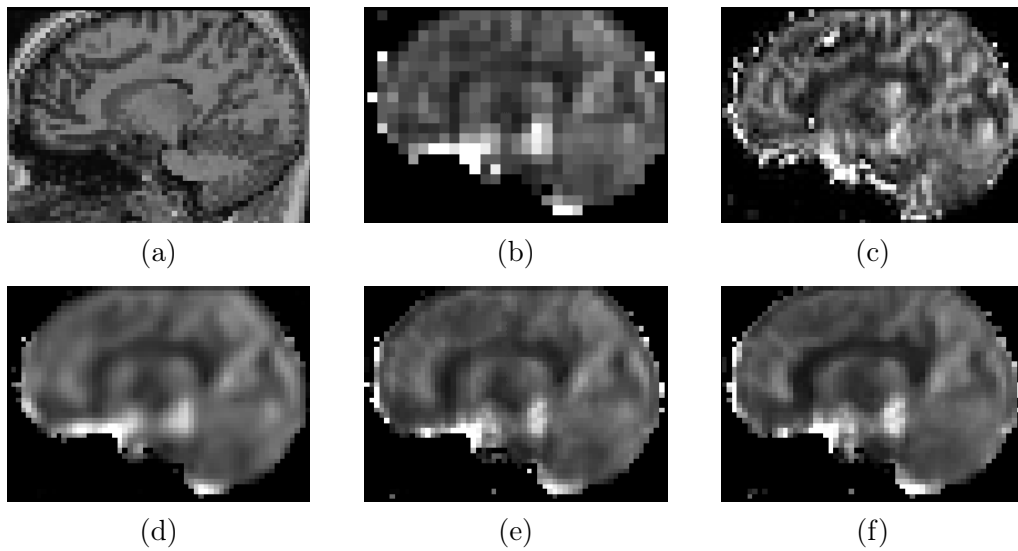


Figure 6.11: Healthy subject: sagittal slices of a structural image (a), low resolution CBF map (b), high resolution CBF map (c), SR3D CBF map reconstruction (d), and CBF estimations from the SR3D MULTI (e) and SR4D (f) reconstructions.

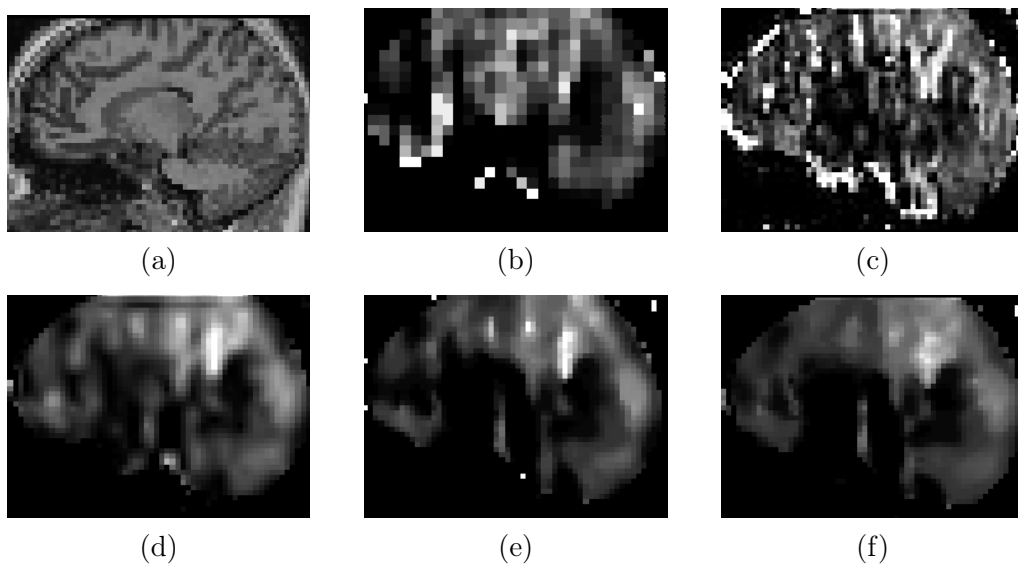


Figure 6.12: Healthy subject: sagittal slices of a structural image (a), low resolution ATT map (b), high resolution ATT map (c), SR3D ATT map reconstruction (d), and ATT estimations from the SR3D MULTI (e) and SR4D (f) reconstructions.

# Conclusion

---

## Standardization and quality control:

The ASL sequence parameters selected following the standardization study presented in chapter 3 led to the acquisitions of 184 ASL scans as part of a large-scale study, whose purpose is to assess interactions between vascular risk factors or markers, and cognitive deficit and decline. To this aim, ASL and MR angiography acquisitions are correlated with data coming from pulse wave velocity assessments, ophthalmological data such as spectral-domain coherence tomography examinations and fundus images, neuropsychological tests based on behavioral and mood scales, and urinary albumin excretion measurements.

The standardization work presented in this document is based on acquisitions performed on a few healthy volunteers. This limited subject number is related to the goal to begin the patients' inclusions as early as possible. Nevertheless, the relatively good quality of the 184 recorded acquisitions, associated with a rejection rate equal to 11%, indicates that the chosen sequence is adapted to the requirements of this study.

Beside the choice of the SENSE parallel imaging method, the selected sequence is as simple as possible, in order to obtain acquisitions that could be similar between multiple centers. Efforts made to develop new sequences (increase of the acquired images resolution, of the temporal resolution, of the SNR), and post-processing methods reducing the influence of artifacts, are proposed by vendors and should allow to obtain even more reliable and reproducible ASL acquisitions. However, including such options as acquisition parameters in multicenter neuroimaging studies does not appear feasible yet, because of the disparity of the performances achieved by these techniques on different scanners.

[Fallatah 2018] recently proposed a visual control scale to perform visual quality assessments dedicated to QUASAR CBF,  $T_1$  relaxation rate, arterial blood volume and ATT maps. While slightly differing in the criteria's grades attribution, especially because of the different parameter maps to be evaluated, very similar aspects are taken into account. This study concludes to the robustness of the proposed procedure within and between different raters, on images acquired on both patients and healthy subjects. One particularly interesting aspect of this work is the definition of several thresholds, that allow to determine with good sensitivity and specificity whether ASL acquisitions are of acceptable quality or not. A combination of such thresholds and automated calculations, as described in this thesis, may further improve the robustness of multiple ASL parameter maps quality assessments in the context of future work.

The standardization study and the quality assessment tool presented in chapter 3

are adapted to 2D EPI ASL acquisitions, which is a limitation of this work. The democratization of 3D readout approaches, as recommended in [Alsop 2015], may necessitate providing adjustments to the proposed solutions, in order to be included in multicenter neuroimaging studies. Indeed, lower contrasts between gray and white matter are usually expected on images acquired by means of 3D readout approaches, which may imply a reduction of the post-labelling delay or an adjustment of the acceptable contrast. However, 3D acquisitions are also associated with reductions of geometric artifacts, such as distortions.

The issue of data variability in large-scale studies can be addressed as it is in this work, focusing on the acquisition aspect. But it is also shown that processing pipelines do have a great influence on this data variability, sometimes making generated data difficult to compare or to include into studies compiling results obtained from different processing approaches. As an example, studies performed by [Carp 2012] and [Bowring 2018] highlighted the influence of strategies adopted in papers or software packages dedicated to the analysis of functional MRI data, resulting in different qualitative and quantitative outcomes. In chapter 4, we also concluded to different behaviors resulting from the application of three different distortion correction methods. Different free software packages providing ASL processing pipelines being available, evaluating the influence of a conjunction of each of the methods proposed to perform the steps required by a pipeline specifically dedicated to ASL images would be of great interest. Indeed, while the use of post-processing methods (motion correction, partial volume correction, temporal and spatial denoising) are shown to increase the reproducibility of analysis performed on a single scanner [Fazlollahi 2015], pooling data obtained from different machines and processing pipelines could be affected by variabilities emanating from both aspects. Transparency about the way data are acquired and processed is an important aspect that is really important to account for in neuroimaging studies.

## Super-resolution for arterial spin labelling images:

The processing methods presented in this document showed to improve the quality and the reliability of ASL images. This aspect has been validated on simulated datasets, healthy subjects and patients scanned for brain tumours. Applying the proposed methods on datasets constituted of data acquired on different populations, such as patients diagnosed with early stages of neurodegenerative diseases, pharmaco-resistant depression forms or subtle CBF perturbations located in small brain areas, and not related to an atrophy that would be visible on a structural image, could be of great interest in the context of future work. As an example, a study recently concluded to specific perfusion patterns correlated with state-anxiety in depressive subjects in the cingulate cortex, insula and amygdala [Conan 2017]. Applying the super-resolution method described in chapter 5 on the images acquired in the context of such a study may allow to refine the location of such particular

perfusion patterns.

Joined to improvements of the ASL acquisition sequences, and particularly concerning the achievable spatial resolutions, the super-resolution algorithms could be of great use in order to analyze CBF maps in neonates and young children CBF maps. Indeed, images acquisition, as well as the application of post-processing algorithms, reveals to be very challenging on these populations. Indeed, while included in an increasing number of studies as a matter to non-invasively assess child brain perfusion, ASL suffers from its low resolution. The evolution of the shape of the brain structure and perfusion patterns during brain development, and CBF changes induced by sedation, are other aspects that have to be taken into account in such cases [Carsin-Vu 2018, Proisy 2016]. Difficulties to perform CBF map registration to structural images, to conduct region-based CBF analysis or the necessity to create different child brain atlases and templates that follow the children's brain evolution with age, outline some of the difficulties related to imaging such particular populations.

The methods presented in this document could also allow to generate high resolution atlases of brain perfusion related parameters, such as CBF and ATT. While actual recommendations consist in acquiring a well resolved single-TI ASL series, and a low resolution multi-TI series to generate ATT maps [Dai 2016], improvements brought to acquisition sequences, associated with the application of a super-resolution algorithm, could allow to estimate more detailed images, that may provide information about localized perfusion decrease or slow down, not directly related to a global vascular territory.

Furthermore, the generation of well detailed ATT maps could allow to delineate these vascular territories, without the need for specific sequences acquisitions. Indeed, in normal brains, the boundaries between different vascular territories have longer ATT than their center [Donahue 2017].

An other aspect that would be interesting to investigate, is the influence that would have an application of a distortion correction method on ASL series, before processing it by means of a super-resolution algorithm. Indeed, while it can be assumed that small misalignments between the initially interpolated image and the structural one, used to drive the reconstruction, do not have a strong influence on the reconstruction process, because of the fact that patches are compared over a quite large search window, hypo and hyper intensities related to susceptibility artifacts could have an impact on the generated high resolution ASL images.



# List of Abbreviations

---

**AD** Alzheimer Disease  
**ANOVA** ANalysis Of VAriance  
**ASL** Arterial Spin Labelling  
**ATT** Arterial Transit Time  
**BAT** Bolus Arrival Time  
**BIDS** Brain Imaging Data Structure  
**BM** Block Matching  
**BS** Background Suppression  
**CASL** Continuous Arterial Spin Labelling  
**CATI** Centre pour l'Acquisition et le Traitement des Images  
**CATIDB** CATI DataBase  
**CBF** Cerebral Blood Flow  
**CBV** Cerebral Blood Volume  
**CT** Computed Tomography  
**DICOM** Digital Imaging and COmmunications in Medicine  
**DSC** Dynamic Susceptibility Contrast  
**DWI** Diffusion Weighted Image  
**EEG** ElectroEncephaloGraphy  
**EPI** Echo Planar Imaging  
**EPISTAR** Echo Planar Imaging Signal Targeting with Alternating Radio-frequency pulses  
**FAIR** Flow-sensitive Alternating Inversion Recovery  
**FDG** Fluorodeoxyglucose  
**FOV** Field Of View  
**GM** Gray Matter  
**GRAPPA** GeneRalized Autocalibrating Partial Parallel Acquisition  
**GRASE** GRadient And Spin Echo  
**GRE** Gradient Echo  
**HmPAO** Hexa-methyl-Propyl-AmineOxime  
**HR** High Resolution  
**HySCO** Hyperelastic Susceptibility artefact COrrrection  
**LD** Labelling Duration  
**Lin Reg** Linear Regression  
**LR** Low Resolution  
**MP2RAGE** Magnetization-Prepared 2 Rapid Gradient-Echoes  
**MPRAGE** Magnetization-Prepared Rapid Gradient-Echo  
**MR** Magnetic Resonance  
**MRI** Magnetic Resonance Imaging

---

**MTT** Mean Transit Time  
**PASL** Pulsed Arterial Spin Labelling  
**pCASL** pseudo-Continuous Arterial Spin Labeling  
**PCT** Perfusion Computed Tomography  
**PED** Phase Encoding Direction  
**PET** Positron Emission Tomography  
**PICORE** Proximal Inversion with Control of Off-Resonance Effects  
**PLD** Post-Labeling Delay  
**PS** Permeability Surface  
**PSNR** Peak Singal-To-Noise Ratio  
**PULSAR** PULsed Signal targeting with Alternating Radio-frequency  
**PV** Partial Volume  
**PVE** Partial Volume Effect  
**Q2TIPS** QUIPSS-II with thin-slice  $TI_1$  Periodic Saturation  
**QUASAR** QUAntitative STAR labeling of Arterial Regions  
**QUIPSS** QUAntitative Imaging of Perfusion using a Single Subtraction  
**rCMRO<sub>glu</sub>** regional Cerebral Metabolic Rate Of Glucose  
**rCMRO<sub>2</sub>** regional Cerebral Metabolic Rate Of Oxygen  
**RARE** Rapid Acquisition with Relaxation Enhancement  
**RF** Radio-Frequency  
**RMSE** Root Mean Square Error  
**rOEF** regional Oxygen Extraction Fraction  
**ROI** Region Of Interest  
**SE** Spin Echo  
**SENSE** SENSitivity Encoding  
**SNR** Signal-to-Noise Ratio  
**SPECT** Single Photon Emission Computed Tomography  
**SPM** Statistical Parametric Mapping  
**SR** Super-Resolution  
**SSIM** Structural SIMilarity  
**TE** Echo Time  
**TI** Inversion Time  
**TR** Repetition Time  
**tSNR** temporal Signal-To-Noise Ratio  
**TTP** Time To Peak  
**TTT** Tissue Transit Time  
**VENC** Velocity ENCoding  
**WM** White Matter

# List of Figures

1	Interface graphique ( <i>qualiCATI</i> ), sur laquelle sont affichés des images et graphiques issus du post-traitement des données ASL. . . . .	vi
2	Images d'un sujet sain : a) image structurale, images de signal ASL à partir de b) la série L>>R, c) la série R>>L, d) la série L>>R corrigée avec l'algorithme de Block Matching, e) la série L>>R corrigée avec l'algorithme TOPUP et f) la série L>>R corrigée avec l'algorithme HySCO. . . . .	ix
3	Sujet sain : coupes sagittales de a) l'image structurale, b) la carte de CBF issue de la série pCASL acquise à basse résolution, c) la carte reconstruite par interpolation trilinéaire, d) par application de B-splines d'ordre 3, et e) l'image obtenue à l'aide de la méthode proposée.	xii
4	Sujet sain: coupes axiales d'une image structurale (a), de la carte de CBF de basse résolution (b) associée, de celle de haute résolution (c), celle reconstruite avec SR3D (d), et des estimations de CBF obtenues suite aux applications de SR3D MULTI (e) et SR4D (f). . . . .	xv
5	Sujet sain: coupes axiales d'une image structurale (a), de la carte d'ATT de basse résolution (b) associée, de celle de haute résolution (c), celle reconstruite avec SR3D (d), et des estimations d'ATT obtenues suite aux applications de SR3D MULTI (e) et SR4D (f). . .	xvi
1.1	Representation of the brain lobes and some sulci and gyri. Image courtesy: <a href="https://en.wikipedia.org/wiki/Lobes_of_the_brain">https://en.wikipedia.org/wiki/Lobes_of_the_brain</a> . . . .	5
1.2	Representation of a) the carotids and vertebral arteries, b) an axial view of arteries ramifications at the basis of the brain and c) the circle of Willis. Image courtesy: [Gray 1918] . . . . .	6
1.3	Image representing the head and neck most important veins. Image courtesy: [College 2014] . . . . .	7
1.4	From left to right: MR diffusion image presenting an hyper-signal in the middle cerebral territory, associated with an hypo-perfusion on 3 axial slices of an ASL perfusion image, and to an occlusion of the middle cerebral artery on the MR angiography. Image courtesy: [Esquevin 2013] . . . . .	8
1.5	From left to right: FLAIR, post-gadolinium T <sub>1</sub> -weighted, and CBF images obtained with ASL of a subject diagnosed with a brain tumour. The tumour appears as hyper-perfused on the CBF maps. Image courtesy: [Esquevin 2013] . . . . .	9
1.6	From left to right: FDG-PET and ASL CBF maps. Left predominant bitemporal anterior hypo-perfusion can be observed on the CBF maps, in agreement with hypo-metabolisms visible on the PET scans. Image courtesy: [Esquevin 2013] . . . . .	9



1.7	14-month-old boy presenting with fever, right unilateral clonic seizures and ipsilateral hemiplegia that lasted for more than 1 hour. Postictal EEG showed slow focal and persistent left cerebral hemisphere activity 24 hours after the seizure. MRI performed during the postictal state shows no abnormality on conventional imaging. a) Apparent diffusion coefficient map reveals restricted focal left hippocampal diffusion (arrow). (b-d) ASL CBF map reveals a larger abnormal area of hyper-perfusion in the left temporal and parieto-occipital lobes (arrows). Image courtesy: [Proisy 2016] . . . . .	10
2.1	Principle of ASL image acquisitions. . . . .	17
2.2	Principle of continuous arterial spin labelling. . . . .	18
2.3	Principle of pulsed arterial spin labelling. . . . .	18
2.4	Timing diagram of pCASL and PASL (QUIPSS-II) acquisitions. . . . .	20
2.5	From upper left to bottom right: ASL signal evolution in an axial slice corresponding to a multi-TI ASL acquisition (12 TIs ranging from 500 ms to 4240 ms). . . . .	22
2.6	Schematic description of the standard model. . . . .	25
2.7	Signal evolution following the standard model. . . . .	26
2.8	Schematic description of the two compartment model. . . . .	27
2.9	Structural image processing. . . . .	28
2.10	ASL image processing pipeline. . . . .	29
2.11	Multi-TI ASL image processing pipeline with external $M_0$ and quantitative tissue $T_1$ acquisitions. . . . .	30
2.12	Upper left to bottom right: signal evolution in an axial slice of an averaged control and label time series. . . . .	31
2.13	Fitting of the $T_1$ recovery curve on the signal evolution of a voxel in an averaged control and label time series. . . . .	32
2.14	Multi-TI ASL image processing pipeline without external $M_0$ and quantitative tissue $T_1$ acquisitions. . . . .	32
3.1	French sites participating in research studies in which the CATI is involved. Research teams are located in sites marked with a star. The other sites perform images acquisitions in a clinical context. ( <i>i2bm.cea.fr</i> ) . . . . .	39
3.2	Images evaluation method adopted to perform the acquisition parameters standardization. . . . .	42
3.3	Data obtained in a healthy subject: tSNR and CBF calculated on the whole brain, gray matter and white matter for the GRAPPA and SENSE parallel imaging methods. . . . .	43
3.4	Motion artifact in the form of a) border duplication, b) image blurring. . . . .	45
3.5	Vascular artifact in the form of a) venous hyperintensities, b) arterial hyperintensities. . . . .	46

3.6	Signal drop caused by a) a labelling issue due to a tortuous artery in the labelling plane, b) a susceptibility artifact. . . . .	47
3.7	Temporal standard deviation maps of ASL series acquired on the same subject with the a) GRAPPA and b) SENSE parallel imaging techniques. . . . .	47
3.8	Difference between images of the same subject acquired following the a) A>>P and b) P>>A phase encoding directions. . . . .	48
3.9	Graphical interface ( <i>qualiCATTI</i> ) on which the review of the acquisition parameters is displayed. . . . .	50
3.10	Graphical interface ( <i>qualiCATTI</i> ) on which images necessary for the quality assessment are displayed. . . . .	51
3.11	Graphical interface ( <i>qualiCATTI</i> ): sections constituting the visual quality control panel. . . . .	52
4.1	Healthy subjects: correlations measured between quantified CBF maps obtained from ASL series acquired with reversed phase encoding directions, and compared while uncorrected for distortions, corrected with the block-matching algorithm, TOPUP or HySCO (left: A>>P and P>>A, right: L>>R and R>>L). . . . .	58
4.2	Healthy subjects: structural similarity index measured between quantified CBF maps obtained from ASL series acquired with reversed phase encoding directions, and compared while uncorrected for distortions, corrected with the block-matching algorithm, TOPUP or HySCO (left: A>>P and P>>A, right: L>>R and R>>L). . . . .	59
4.3	Healthy subjects: correlations (left) and structural similarity index (right) measured on quantified CBF maps obtained from ASL series acquired following the A>>P and L>>R phase encoding directions. . . . .	59
4.4	Images acquired on a healthy subject: a) structural images, b) mean ASL signal maps obtained from the ASL series acquired following the A>>P phase encoding direction, c) following the P>>A PED, d) after applying the block-matching distortion correction algorithm, e) after correction with the TOPUP method and f) after correction with the HySCO method. . . . .	61
4.5	Images acquired on a healthy subject: a) structural images, b) mean ASL signal maps obtained from the ASL series acquired following the L>>R phase encoding direction, c) following the R>>L PED, d) after applying the block-matching distortion correction algorithm, e) after correction with the TOPUP method and f) after correction with the HySCO method. . . . .	62
5.1	Pipeline describing the generation of the simulated dataset and the different reconstruction methods to be compared, applied to the downscaled and noise corrupted images. . . . .	71

5.2	Graphs showing the RMSE values calculated between the reference HR image and images reconstructed with the proposed high resolution reconstruction method, by taking only the ASL, $[\beta_{asl}; \beta_{struct}]$ equal to [0.25; 0.75] (more ASL than structural), [0.5; 0.5] (equivalent contribution), [0.75; 0.25] (less ASL than structural), or only the structural image into account. The displayed noise levels correspond to 3%, 6% and 9% of the GM CBF value. . . . .	74
5.3	Simulated dataset: comparison of a) a HR reference image and b) the corresponding low resolution downsampled image corrupted by noise with std=9% of the GM CBF value, c) nearest neighbor interpolation, d) trilinear interpolation, e) 3rd order B-spline interpolation, and f) proposed SR reconstruction. . . . .	75
5.4	Healthy subject: sagittal slices of a) a structural image, b) the corresponding CBF map from the acquired low resolution pCASL, c) after trilinear interpolation, d) after 3rd order B-spline interpolation, and e) the proposed SR reconstructed CBF image. Upper lines: sagittal slices, bottom lines: zoom on the same slices. . . . .	77
5.5	Healthy subject: axial slices of a) a structural image, b) the corresponding CBF map from the low resolution pCASL acquisition, c) the HR acquisition, d) after trilinear interpolation, e) after 3rd order B-spline interpolation, and f) the proposed SR reconstructed CBF image. Upper lines: sagittal slices, bottom lines: zoom on the same slices. . . . .	78
5.6	Pearson correlation coefficient between the reference DSC CBF maps and low resolution CBF images, the same images after trilinear interpolation, 3rd order B-spline interpolation and the proposed SR reconstruction method. These coefficients are presented for each of the 10 subjects. . . . .	79
5.7	a) structural image, b) DSC CBF image, c) low resolution ASL CBF image and d) SR reconstructed ASL CBF map. The two lines correspond to images of two different subjects. . . . .	80
5.8	Pipeline describing the operations applied to each of the 9 images of the simulated dataset and the GM contribution assessment maps to be compared. . . . .	81
5.9	Comparison of gray matter cerebral blood flow contribution maps: a) GM contribution maps from the reference image, b) linear regression applied to the low resolution CBF image, c) linear regression applied to the low resolution ASL and $M_0$ images, and d) proposed SR method applied to the LR CBF image (SNR=5). . . . .	82

5.10	Comparison of gray matter cerebral blood flow contribution maps: a) difference images obtained by subtraction of the reference GM contribution map from the images obtained by applying the linear regression (Lin Reg) to the low resolution (LR) CBF image, b) the linear regression to the LR ASL and $M_0$ images, and c) the proposed SR method to the LR CBF image (SNR=5). . . . .	83
6.1	Schematic representation of the reconstruction performed in the proposed SR4D method. . . . .	88
6.2	Schematic description of the SR3D MULTI method. . . . .	90
6.3	Simulated dataset: PSNR obtained by comparing reference CBF and ATT maps with the SR4D reconstructions obtained with different $\beta$ parameter values. . . . .	91
6.4	Simulated dataset: PSNR obtained by comparing reference CBF and ATT maps with the splines, SR3D, SR3D MULTI and SR4D reconstructions. . . . .	92
6.5	Simulated dataset: CBF maps from : a) the reference image, b) the CBF estimation from the noise corrupted downsampled series, c) the splines interpolation, d) the SR3D reconstruction, e) estimations from the SR3D MULTI and f) SR4D reconstructed ASL time series. . . . .	93
6.6	Simulated dataset: ATT maps from: a) the reference image, b) the ATT estimation from the noise corrupted downsampled series, c) the splines interpolation, d) the SR3D reconstruction, e) estimations from the SR3D MULTI and f) SR4D reconstructed ASL time series. . . . .	94
6.7	Simulated dataset: ASL signal temporal evolution of a voxel in the reference, 2 noisy low resolution and the 2 corresponding SR3D MULTI and SR4D reconstructed time series. . . . .	95
6.8	Healthy subjects: mean $\pm$ standard deviation (std) and percentage of brain voxels with correlations to the single compartment model superior to 0.5 for the low resolution (LR), high resolution (HR), SR3D MULTI and proposed SR4D reconstructed ASL signal time series. . . . .	96
6.9	Images from one healthy subject: axial slices of a structural image (a), low resolution CBF map (b), high resolution CBF map (c), SR3D CBF map reconstruction (d), and CBF estimations from the SR3D MULTI (e) and SR4D (f) reconstructions. . . . .	97
6.10	Images from one healthy subject: axial slices of a structural image (a), low resolution ATT map (b), high resolution ATT map (c), SR3D ATT map reconstruction (d), and ATT estimations from the SR3D MULTI (e) and SR4D (f) reconstructions. . . . .	98
6.11	Healthy subject: sagittal slices of a structural image (a), low resolution CBF map (b), high resolution CBF map (c), SR3D CBF map reconstruction (d), and CBF estimations from the SR3D MULTI (e) and SR4D (f) reconstructions. . . . .	100

- 6.12 Healthy subject: sagittal slices of a structural image (a), low resolution ATT map (b), high resolution ATT map (c), SR3D ATT map reconstruction (d), and ATT estimations from the SR3D MULTI (e) and SR4D (f) reconstructions. . . . . 100

# List of Tables

1	Nombre de sujets imagés par combinaison de paramètres, SNR temporel et CBF calculés sur des masques de cerveaux, et scores d'évaluation visuelle associés aux acquisitions ASL. Les astérisques indiquent qu'au moins l'une des cartes de CBF obtenues à partir des paramètres associés présentait un hypersignal artériel. . . . .	v
2	Moyenne et écart-type (std) des 9 RMSE calculées entre les images de référence et les reconstructions obtenues par application des interpolations de type plus proche voisin, trilineaire, B-splines d'ordre 3, ou la méthode proposée, pour des niveaux de bruit croissants. L'écart-type du bruit est exprimé en pourcentage de la valeur de CBF affectée à la substance grise. Les astérisques soulignent des différences significatives avec la méthode proposée.. . . .	xi
2.1	Recommended LD and PLD for single-TI pCASL and QUIPSS-II PASL acquisitions [Alsop 2015]. . . . .	21
3.1	Fixed parameters selected to perform the standardization study. . . .	40
3.2	Number of subjects scanned, tSNR, brain CBF and visual evaluation score associated with each of the parameters combinations used to acquire ASL images in the context of the acquisition parameters standardization study. Asterisks indicate that at least one of the CBF maps generated from the parameters set presented arterial hyper-signal.	44
3.3	Parameters selected following the acquisition parameters standardization study. . . . .	45
3.4	Summary of the quality control performed on the ASL scans acquired in the context of a neuroimaging study. . . . .	53
5.1	Means and standard deviations of the 9 RMSE values calculated between the reference HR image and the images reconstructed with nearest neighbor interpolation, trilinear interpolation, 3rd order B-spline interpolation and the proposed SR reconstruction method, with increasing levels of noise. Standard deviations of noise are expressed as percentage of the GM CBF value. Asterisks are joined to RMSE values corresponding to significant differences compared to the values obtained by application of the proposed method. . . . .	74
5.2	RMSE values calculated between the HR acquired reference image and the images generated by nearest neighbor interpolation, trilinear interpolation, 3rd order B-spline interpolation and the proposed SR reconstruction method, for each of the 4 healthy subjects (lowest RMSE value in bold for each subject). . . . .	76

---

5.3	Mean RMSE values between the reference GM CBF contribution images and the images obtained after linear regression (Lin Reg) on the low resolution (LR) CBF image, Lin Reg on the ASL and $M_0$ images, and the proposed SR method applied to the LR CBF images. . . . .	81
5.4	Mean RMSE values between the reference GM CBF contribution images and the images obtained after linear regression (Lin Reg) on the low resolution(LR) CBF image and on the ASL and $M_0$ images, with noise added to the partial volume estimates needed by the Lin Reg method, and the proposed SR method applied to the LR CBF images. . . . .	82
5.5	Mean RMSE values between the reference GM CBF contribution images and the images obtained after linear regression (Lin Reg) on the low resolution (LR) CBF image and on the ASL and $M_0$ images, with an opening+closing operation added to the partial volume estimates needed by the Lin Reg method, and the proposed SR method applied to the LR CBF images. . . . .	82

# Bibliography

- [Alsop 1996] D. C. Alsop and J. A. Detre. *Reduced Transit-Time Sensitivity in Noninvasive Magnetic Resonance Imaging of Human Cerebral Blood Flow*. *Journal of Cerebral Blood Flow & Metabolism*, vol. 16, no. 6, pages 1236–1249, nov 1996. (Cited on page 20.)
- [Alsop 2015] David C. Alsop, John A. Detre, Xavier Golay, Matthias Günther, Jeroen Hendrikse, Luis Hernandez-Garcia, Hanzhang Lu, Bradley J. MacIntosh, Laura M. Parkes, Marion Smits, Matthias J. P. van Osch, Danny J. J. Wang, Eric C. Wong and Greg Zaharchuk. *Recommended implementation of arterial spin-labeled perfusion MRI for clinical applications: A consensus of the ISMRM perfusion study group and the European consortium for ASL in dementia*. *Magnetic Resonance in Medicine*, vol. 73, no. 1, pages 102–116, 2015. (Cited on pages iv, 16, 19, 20, 21, 23, 40, 41, 102 and 113.)
- [Andersson 2003] Jesper L.R. Andersson, Stefan Skare and John Ashburner. *How to correct susceptibility distortions in spin-echo echo-planar images: application to diffusion tensor imaging*. *NeuroImage*, vol. 20, no. 2, pages 870–888, oct 2003. (Cited on pages vii, 56 and 57.)
- [Ashburner 2005] John Ashburner and Karl J. Friston. *Unified segmentation*. *NeuroImage*, vol. 26, no. 3, pages 839–851, jul 2005. (Cited on page 27.)
- [Asllani 2008] Iris Asllani, Ajna Borogovac and Truman R. Brown. *Regression algorithm correcting for partial volume effects in arterial spin labeling MRI*. *Magnetic Resonance in Medicine*, vol. 60, no. 6, pages 1362–1371, 2008. (Cited on pages xii, 66, 67, 78 and 79.)
- [Bokkers 2009] R.P.H. Bokkers, H. B. van der Worp, W. P.T.M. Mali and J. Hendrikse. *Noninvasive MR imaging of cerebral perfusion in patients with a carotid artery stenosis*. *Neurology*, vol. 73, no. 11, pages 869–875, sep 2009. (Cited on page 8.)
- [Boudes 2014] Elodie Boudes, Guillaume Gilbert, Ilana Ruth Leppert, Xianming Tan, G. Bruce Pike, Christine Saint-Martin and Pia Wintermark. *Measurement of brain perfusion in newborns: Pulsed arterial spin labeling (PASL) versus pseudo-continuous arterial spin labeling (pCASL)*. *NeuroImage: Clinical*, vol. 6, pages 126–133, 2014. (Cited on page 53.)
- [Bowring 2018] Alexander Bowring, Camille Maumet and Thomas Nichols. *Exploring the Impact of Analysis Software on Task fMRI Results*. mar 2018. (Cited on page 102.)



- [Buxton 1998] Richard B. Buxton, Lawrence R. Frank, Eric C. Wong, Bettina Siewert, Steven Warach and Robert R. Edelman. *A general kinetic model for quantitative perfusion imaging with arterial spin labeling*. *Magnetic Resonance in Medicine*, vol. 40, no. 3, pages 383–396, sep 1998. (Cited on pages [iv](#), [23](#), [24](#), [28](#), [71](#), [72](#) and [89](#).)
- [Carp 2012] Joshua Carp. *On the Plurality of (Methodological) Worlds: Estimating the Analytic Flexibility of fMRI Experiments*. *Frontiers in Neuroscience*, vol. 6, 2012. (Cited on page [102](#).)
- [Carsin-Vu 2018] Aline Carsin-Vu, Isabelle Corouge, Olivier Commowick, Guillaume Bouzillé, Christian Barillot, Jean-Christophe Ferré and Maia Proisy. *Measurement of pediatric regional cerebral blood flow from 6 months to 15 years of age in a clinical population*. *European Journal of Radiology*, vol. 101, pages 38–44, apr 2018. (Cited on page [103](#).)
- [Chang 1992] H. Chang and J.M. Fitzpatrick. *A technique for accurate magnetic resonance imaging in the presence of field inhomogeneities*. *IEEE Transactions on Medical Imaging*, vol. 11, no. 3, pages 319–329, 1992. (Cited on page [56](#).)
- [Chappell 2011] M. A. Chappell, A. R. Groves, B. J. MacIntosh, M. J. Donahue, P. Jezard and M. W. Woolrich. *Partial volume correction of multiple inversion time arterial spin labeling MRI data*. *Magnetic Resonance in Medicine*, vol. 65, no. 4, pages 1173–1183, 2011. (Cited on pages [66](#), [67](#) and [79](#).)
- [Chen 2011] Y. Chen, D. A. Wolk, J. S. Reddin, M. Korczykowski, P. M. Martinez, E. S. Musiek, A. B. Newberg, P. Julin, S. E. Arnold, J. H. Greenberg and J. A. Detre. *Voxel-level comparison of arterial spin-labeled perfusion MRI and FDG-PET in Alzheimer disease*. *Neurology*, vol. 77, no. 22, pages 1977–1985, nov 2011. (Cited on page [9](#).)
- [Chen 2018a] Yuhua Chen, Feng Shi, Anthony G. Christodoulou, Zhengwei Zhou, Yibin Xie and Debiao Li. *Efficient and Accurate MRI Super-Resolution using a Generative Adversarial Network and 3D Multi-Level Densely Connected Network*. *CoRR*, vol. abs/1803.01417, 2018. (Cited on page [66](#).)
- [Chen 2018b] Yuhua Chen, Yibin Xie, Zhengwei Zhou, Feng Shi, Anthony G. Christodoulou and Debiao Li. *Brain MRI Super Resolution Using 3D Deep Densely Connected Neural Networks*. *CoRR*, vol. abs/1801.02728, 2018. (Cited on page [66](#).)
- [College 2014] OpenStax College. *Anatomy & physiology*. OpenStax CNX, 2014. (Cited on pages [7](#) and [107](#).)
- [Colloby 2012] Sean J. Colloby, Michael J. Firbank, Jiabao He, Alan J. Thomas, Akshya Vasudev, Steve W. Parry and John T. O'Brien. *Regional cerebral*

*blood flow in late-life depression: arterial spin labelling magnetic resonance study.* British Journal of Psychiatry, vol. 200, no. 02, pages 150–155, feb 2012. (Cited on page 9.)

[Conan 2017] C. Conan, J.M. Batail, I. Corouge, J. Palaric, G. Robert and D. Drapier. *Apathy in depression: An arterial spin labeling study.* European Psychiatry, vol. 41, pages S344–S345, apr 2017. (Cited on page 102.)

[Coupé 2013] Pierrick Coupé, José V. Manjón, Maxime Chamberland, Maxime Descoteaux and Bassem Hiba. *Collaborative patch-based super-resolution for diffusion-weighted images.* NeuroImage, vol. 83, pages 245–261, dec 2013. (Cited on pages 66, 67, 68, 69 and 73.)

[Dai 2008] Weiyang Dai, Dairon Garcia, Cedric de Bazelaire and David C. Alsop. *Continuous flow-driven inversion for arterial spin labeling using pulsed radio frequency and gradient fields.* Magnetic Resonance in Medicine, vol. 60, no. 6, pages 1488–1497, dec 2008. (Cited on page 19.)

[Dai 2011] Weiyang Dai, Philip M Robson, Ajit Shankaranarayanan and David C. Alsop. *Reduced resolution transit delay prescan for quantitative continuous arterial spin labeling perfusion imaging.* Magnetic Resonance in Medicine, vol. 67, no. 5, pages 1252–1265, nov 2011. (Cited on page 96.)

[Dai 2016] Weiyang Dai, Tamara Fong, Richard N. Jones, Edward Marcantonio, Eva Schmitt, Sharon K. Inouye and David C. Alsop. *Effects of arterial transit delay on cerebral blood flow quantification using arterial spin labeling in an elderly cohort.* Journal of Magnetic Resonance Imaging, vol. 45, no. 2, pages 472–481, jul 2016. (Cited on page 103.)

[Detre 1992] John A. Detre, John S. Leigh, Donald S. Williams and Alan P. Koretsky. *Perfusion imaging.* Magnetic Resonance in Medicine, vol. 23, no. 1, pages 37–45, 1992. (Cited on pages 13 and 16.)

[Donahue 2017] Manus J Donahue, Eric Achten, Petrice M Cogswell, Frank-Erik De Leeuw, Colin P Derdeyn, Rick M Dijkhuizen, Audrey P Fan, Rashid Ghaznawi, Jeremy J Heit, M Arfan Ikram, Peter Jezzard, Lori C Jordan, Eric Jouvent, Linda Knutsson, Richard Leigh, David S Liebeskind, Weili Lin, Thomas W Okell, Adnan I Qureshi, Charlotte J Stagg, Matthias JP van Osch, Peter CM van Zijl, Jennifer M Watchmaker, Max Wintermark, Ona Wu, Greg Zaharchuk, Jinyuan Zhou and Jeroen Hendrikse. *Consensus statement on current and emerging methods for the diagnosis and evaluation of cerebrovascular disease.* Journal of Cerebral Blood Flow & Metabolism, vol. 38, no. 9, pages 1391–1417, aug 2017. (Cited on page 103.)

[Duhameau 2010] Bérengère Duhameau, Jean-Christophe Ferré, Pierre Jannin, Jean-Yves Gauvrit, Marc Vérin, Bruno Millet and Dominique Drapier.

- Chronic and treatment-resistant depression: A study using arterial spin labeling perfusion MRI at 3Tesla.* Psychiatry Research: Neuroimaging, vol. 182, no. 2, pages 111–116, may 2010. (Cited on page 9.)
- [Duncan 2010] John S. Duncan. *Imaging in the surgical treatment of epilepsy.* Nature Reviews Neurology, vol. 6, no. 10, pages 537–550, sep 2010. (Cited on page 10.)
- [Edelman 1994] R R Edelman, B Siewert, D G Darby, V Thangaraj, A C Nobre, M M Mesulam and S Warach. *Qualitative mapping of cerebral blood flow and functional localization with echo-planar MR imaging and signal targeting with alternating radio frequency.* Radiology, vol. 192, no. 2, pages 513–520, aug 1994. (Cited on page 19.)
- [Embleton 2010] Karl V. Embleton, Hamied A. Haroon, David M. Morris, Matthew A. Lambon Ralph and Geoff J.M. Parker. *Distortion correction for diffusion-weighted MRI tractography and fMRI in the temporal lobes.* Human Brain Mapping, vol. 31, no. 10, pages 1570–1587, feb 2010. (Cited on page 56.)
- [Esquevin 2013] Aurore Esquevin, Hélène Raoult, Serge Belliard, Isabelle Corouge, Elise Bannier, Florence Le Jeune, Christian Barillot, Jean-Yves Gauvrit and Jean-Christophe Ferré. *Étude de la perfusion cérébrale par Arterial Spin Labeling : principes et applications en neurosciences cliniques.* Revue de neuropsychologie, vol. 5, no. 2, page 135, 2013. (Cited on pages 8, 9 and 107.)
- [Fallatah 2018] S. M. Fallatah, F. B. Pizzini, B. Gomez-Anson, J. Magerkurth, E. De Vita, S. Bisdas, H. R. Jäger, H. J. M. M. Mutsaerts and X. Golay. *A visual quality control scale for clinical arterial spin labeling images.* European Radiology Experimental, vol. 2, no. 1, dec 2018. (Cited on page 101.)
- [Fazlollahi 2015] Amir Fazlollahi, Pierrick Bourgeat, Xiaoyun Liang, Fabrice Meriaudeau, Alan Connelly, Olivier Salvado and Fernando Calamante. *Reproducibility of multiphase pseudo-continuous arterial spin labeling and the effect of post-processing analysis methods.* NeuroImage, vol. 117, pages 191–201, aug 2015. (Cited on page 102.)
- [Fernández-Seara 2005] María A. Fernández-Seara, Ze Wang, Jiongjiang Wang, Heng-Yi Rao, Matthias Guenther, David A. Feinberg and John A. Detre. *Continuous arterial spin labeling perfusion measurements using single shot 3D GRASE at 3 T.* Magnetic Resonance in Medicine, vol. 54, no. 5, pages 1241–1247, 2005. (Cited on page 21.)
- [Ferré 2012] Jean-Christophe Ferré, Jan Petr, Elise Bannier, Christian Barillot and Jean-Yves Gauvrit. *Improving quality of arterial spin labeling MR imaging at 3 tesla with a 32-channel coil and parallel imaging.* Journal of Magnetic Resonance Imaging, vol. 35, no. 5, pages 1233–1239, jan 2012. (Cited on pages 23 and 41.)

- [Garcia 2005] Dairon M. Garcia, Guillaume Duhamel and David C. Alsop. *Efficiency of inversion pulses for background suppressed arterial spin labeling*. *Magnetic Resonance in Medicine*, vol. 54, no. 2, pages 366–372, 2005. (Cited on page 21.)
- [Golay 2004] Xavier Golay, Esben T. Petersen and Francis Hui. *Pulsed star labeling of arterial regions (PULSAR): A robust regional perfusion technique for high field imaging*. *Magnetic Resonance in Medicine*, vol. 53, no. 1, pages 15–21, 2004. (Cited on page 19.)
- [Gorgolewski 2011] Krzysztof Gorgolewski, Christopher D. Burns, Cindee Madison, Dav Clark, Yaroslav O. Halchenko, Michael L. Waskom and Satrajit S. Ghosh. *Nipype: A Flexible, Lightweight and Extensible Neuroimaging Data Processing Framework in Python*. *Frontiers in Neuroinformatics*, vol. 5, 2011. (Cited on pages 27 and 73.)
- [Gorgolewski 2016] Krzysztof J. Gorgolewski, Tibor Auer, Vince D. Calhoun, R. Cameron Craddock, Samir Das, Eugene P. Duff, Guillaume Flandin, Satrajit S. Ghosh, Tristan Glatard, Yaroslav O. Halchenko, Daniel A. Handwerker, Michael Hanke, David Keator, Xiangrui Li, Zachary Michael, Camille Maumet, B. Nolan Nichols, Thomas E. Nichols, John Pellman, Jean-Baptiste Poline, Ariel Rokem, Gunnar Schaefer, Vanessa Sochat, William Triplett, Jessica A. Turner, Gaël Varoquaux and Russell A. Poldrack. *The brain imaging data structure, a format for organizing and describing outputs of neuroimaging experiments*. *Scientific Data*, vol. 3, page 160044, jun 2016. (Cited on page 28.)
- [Grade 2015] M. Grade, J. A. Hernandez Tamames, F. B. Pizzini, E. Achten, X. Golay and M. Smits. *A neuroradiologist’s guide to arterial spin labeling MRI in clinical practice*. *Neuroradiology*, vol. 57, no. 12, pages 1181–1202, sep 2015. (Cited on page 8.)
- [Gray 1918] Henry Gray. *Anatomy of the human body*. Lea & Febiger, 1918. (Cited on pages 6 and 107.)
- [Griswold 2002] Mark A. Griswold, Peter M. Jakob, Robin M. Heidemann, Mathias Nittka, Vladimir Jellus, Jianmin Wang, Berthold Kiefer and Axel Haase. *Generalized autocalibrating partially parallel acquisitions (GRAPPA)*. *Magnetic Resonance in Medicine*, vol. 47, no. 6, pages 1202–1210, jun 2002. (Cited on pages 23 and 47.)
- [Günther 2001] Matthias Günther, Michael Bock and Lothar R. Schad. *Arterial spin labeling in combination with a look-locker sampling strategy: Inflow turbo-sampling EPI-FAIR (ITS-FAIR)*. *Magnetic Resonance in Medicine*, vol. 46, no. 5, pages 974–984, oct 2001. (Cited on page 13.)

- [Günther 2005] Matthias Günther, Koichi Oshio and David A. Feinberg. *Single-shot 3D imaging techniques improve arterial spin labeling perfusion measurements*. *Magnetic Resonance in Medicine*, vol. 54, no. 2, pages 491–498, 2005. (Cited on page 21.)
- [Hedouin 2017] Renaud Hedouin, Olivier Commowick, Elise Bannier, Benoit Scherrer, Maxime Taquet, Simon K. Warfield and Christian Barillot. *Block-Matching Distortion Correction of Echo-Planar Images With Opposite Phase Encoding Directions*. *IEEE Transactions on Medical Imaging*, vol. 36, no. 5, pages 1106–1115, may 2017. (Cited on pages vii, 56 and 57.)
- [Hendrikse 2004] Jeroen Hendrikse, Matthias J. P. van Osch, Dirk R. Rutgers, Chris J. G. Bakker, L. Jaap Kappelle, Xavier Golay and Jeroen van der Grond. *Internal Carotid Artery Occlusion Assessed at Pulsed Arterial Spin-labeling Perfusion MR Imaging at Multiple Delay Times*. *Radiology*, vol. 233, no. 3, pages 899–904, dec 2004. (Cited on page 8.)
- [Ho 2013] Tiffany C. Ho, Jing Wu, David D. Shin, Thomas T. Liu, Susan F. Tappert, Guang Yang, Colm G. Connolly, Guido K.W. Frank, Jeffrey E. Max, Owen Wolkowitz, Stuart Eisendrath, Fumiko Hoeft, Dipavo Banerjee, Corey Hood, Robert L. Hendren, Martin P. Paulus, Alan N. Simmons and Tony T. Yang. *Altered Cerebral Perfusion in Executive, Affective, and Motor Networks During Adolescent Depression*. *Journal of the American Academy of Child & Adolescent Psychiatry*, vol. 52, no. 10, pages 1076–1091.e2, oct 2013. (Cited on page 9.)
- [Homan 2012] P Homan, J Kindler, M Hauf, D Hubl and T Dierks. *Cerebral blood flow identifies responders to transcranial magnetic stimulation in auditory verbal hallucinations*. *Translational Psychiatry*, vol. 2, no. 11, pages e189–e189, nov 2012. (Cited on page 10.)
- [Hong 2015] Xin Hong, Xuan Vinh To, Irvin Teh, Jian Rui Soh and Kai-Hsiang Chuang. *Evaluation of EPI distortion correction methods for quantitative MRI of the brain at high magnetic field*. *Magnetic Resonance Imaging*, vol. 33, no. 9, pages 1098–1105, nov 2015. (Cited on page 56.)
- [Jain 2017] Saurabh Jain, Diana M. Sima, Faezeh Sanaei Nezhad, Gilbert Hangel, Wolfgang Bogner, Stephen Williams, Sabine Van Huffel, Frederik Maes and Dirk Smeets. *Patch-Based Super-Resolution of MR Spectroscopic Images: Application to Multiple Sclerosis*. *Frontiers in Neuroscience*, vol. 11, jan 2017. (Cited on pages 66, 67 and 68.)
- [Jezzard 1995] Peter Jezzard and Robert S. Balaban. *Correction for geometric distortion in echo planar images from B0 field variations*. *Magnetic Resonance in Medicine*, vol. 34, no. 1, pages 65–73, jul 1995. (Cited on page 56.)

- [Jia 2017] Yuanyuan Jia, Ali Gholipour, Zhongshi He and Simon K. Warfield. *A New Sparse Representation Framework for Reconstruction of an Isotropic High Spatial Resolution MR Volume From Orthogonal Anisotropic Resolution Scans*. IEEE Transactions on Medical Imaging, vol. 36, no. 5, pages 1182–1193, may 2017. (Cited on page 66.)
- [Johnston 2015] Megan E. Johnston, Kun Lu, Joseph A. Maldjian and Youngkyoo Jung. *Multi-TI Arterial Spin Labeling MRI with Variable TR and Bolus Duration for Cerebral Blood Flow and Arterial Transit Time Mapping*. IEEE Transactions on Medical Imaging, vol. 34, no. 6, pages 1392–1402, jun 2015. (Cited on page 31.)
- [Kety 1948] Seymour S. Kety and Carl F. Schmidt. *THE NITROUS OXIDE METHOD FOR THE QUANTITATIVE DETERMINATION OF CEREBRAL BLOOD FLOW IN MAN: THEORY, PROCEDURE AND NORMAL VALUES 1*. Journal of Clinical Investigation, vol. 27, no. 4, pages 476–483, jul 1948. (Cited on pages 11 and 12.)
- [Kim 1995] Seong-Gi Kim. *Quantification of relative cerebral blood flow change by flow-sensitive alternating inversion recovery (FAIR) technique: Application to functional mapping*. Magnetic Resonance in Medicine, vol. 34, no. 3, pages 293–301, sep 1995. (Cited on page 19.)
- [Kim 2013] Tae Kim, Wanyong Shin, Tiejun Zhao, Erik B. Beall, Mark J. Lowe and Kyongtae T. Bae. *Whole brain perfusion measurements using arterial spin labeling with multiband acquisition*. Magnetic Resonance in Medicine, vol. 70, no. 6, pages 1653–1661, jul 2013. (Cited on page 23.)
- [Kimura 2005] Hirohiko Kimura, Hirotugu Kado, Yoshio Koshimoto, Tatsuro Tsuchida, Yoshiharu Yonekura and Harumi Itoh. *Multislice continuous arterial spin-labeled perfusion MRI in patients with chronic occlusive cerebrovascular disease: A correlative study with CO<sub>2</sub> PET validation*. Journal of Magnetic Resonance Imaging, vol. 22, no. 2, pages 189–198, 2005. (Cited on page 8.)
- [Kindler 2013] J. Kindler, K. Jann, P. Homan, M. Hauf, S. Walther, W. Strik, T. Dierks and D. Hubl. *Static and Dynamic Characteristics of Cerebral Blood Flow During the Resting State in Schizophrenia*. Schizophrenia Bulletin, vol. 41, no. 1, pages 163–170, dec 2013. (Cited on page 10.)
- [Kiselev 2001] V.G. Kiselev. *On the theoretical basis of perfusion measurements by dynamic susceptibility contrast MRI*. Magnetic Resonance in Medicine, vol. 46, no. 6, pages 1113–1122, 2001. (Cited on page 12.)
- [Knutsson 2010] Linda Knutsson, Danielle van Westen, Esben T. Petersen, Karin Markenroth Bloch, Stig Holtås, Freddy Ståhlberg and Ronnie Wirestam. *Absolute quantification of cerebral blood flow: correlation between*

- dynamic susceptibility contrast MRI and model-free arterial spin labeling*. Magnetic Resonance Imaging, vol. 28, no. 1, pages 1–7, jan 2010. (Cited on page 72.)
- [Lassen 1988] Niels A. Lassen, Allan R. Andersen, Lars Friberg and Olaf B. Paulson. *The Retention of [99mTc]-d, l-HM-PAO in the Human Brain after Intracarotid Bolus Injection: A Kinetic Analysis*. Journal of Cerebral Blood Flow & Metabolism, vol. 8, no. 1\_suppl, pages S13–S22, dec 1988. (Cited on page 11.)
- [Li 2015] Xiufeng Li, Dingxin Wang, Edward J. Auerbach, Steen Moeller, Kamil Ugurbil and Gregory J. Metzger. *Theoretical and experimental evaluation of multi-band EPI for high-resolution whole brain pCASL Imaging*. NeuroImage, vol. 106, pages 170–181, feb 2015. (Cited on page 23.)
- [Liu 2010] Peiyong Liu, Jinsoo Uh and Hanzhang Lu. *Determination of spin compartment in arterial spin labeling MRI*. Magnetic Resonance in Medicine, vol. 65, no. 1, pages 120–127, aug 2010. (Cited on page 13.)
- [Luh 1999] Wen-Ming Luh, Eric C. Wong, Peter A. Bandettini and James S. Hyde. *QUIPSS II with thin-slice T1 periodic saturation: A method for improving accuracy of quantitative perfusion imaging using pulsed arterial spin labeling*. Magnetic Resonance in Medicine, vol. 41, no. 6, pages 1246–1254, jun 1999. (Cited on page 19.)
- [Ma 2017] Hong Ma, Zizheng Wang, Kai Xu, Zefeng Shao, Chun Yang, Peng Xu, Xiaohua Liu, Chunfeng Hu, Xin Lu and Yutao Rong. *Three-dimensional arterial spin labeling imaging and dynamic susceptibility contrast perfusion-weighted imaging value in diagnosing glioma grade prior to surgery*. Experimental and Therapeutic Medicine, vol. 13, no. 6, pages 2691–2698, apr 2017. (Cited on page 72.)
- [MacIntosh 2010] Bradley J. MacIntosh, Nicola Filippini, Michael A. Chappell, Mark W. Woolrich, Clare E. Mackay and Peter Jezzard. *Assessment of arterial arrival times derived from multiple inversion time pulsed arterial spin labeling MRI*. Magnetic Resonance in Medicine, vol. 63, no. 3, pages 641–647, mar 2010. (Cited on page 13.)
- [Madai 2016] Vince I. Madai, Steve Z. Martin, Federico C. von Samson-Himmelstjerna, Cornelius X. Herzig, Matthias A. Mutke, Carla N. Wood, Thoralf Thamm, Sarah Zweynert, Miriam Bauer, Stefan Hetzer, Matthias Günther and Jan Sobesky. *Correction for Susceptibility Distortions Increases the Performance of Arterial Spin Labeling in Patients with Cerebrovascular Disease*. Journal of Neuroimaging, vol. 26, no. 4, pages 436–444, jan 2016. (Cited on pages vii, 56, 57 and 60.)

- [Mak 2012] Henry K.F. Mak, Queenie Chan, Zhipeng Zhang, Esben T. Petersen, Deqiang Qiu, Linda Zhang, Kelvin K.W. Yau, Leung-Wing Chu and Xavier Golay. *Quantitative Assessment of Cerebral Hemodynamic Parameters by QUASAR Arterial Spin Labeling in Alzheimer's Disease and Cognitively Normal Elderly Adults at 3-Tesla*. *Journal of Alzheimer's Disease*, vol. 31, no. 1, page 33–44, Jul 2012. (Cited on page 9.)
- [Maleki 2011] Nasim Maleki, Weiyang Dai and David C. Alsop. *Optimization of background suppression for arterial spin labeling perfusion imaging*. *Magnetic Resonance Materials in Physics, Biology and Medicine*, vol. 25, no. 2, pages 127–133, oct 2011. (Cited on page 21.)
- [Manjón 2010] José V. Manjón, Pierrick Coupé, Antonio Buades, D. Louis Collins and Montserrat Robles. *MRI Superresolution Using Self-Similarity and Image Priors*. *International Journal of Biomedical Imaging*, vol. 2010, pages 1–11, 2010. (Cited on pages 66, 67 and 68.)
- [Marques 2010] José P. Marques, Tobias Kober, Gunnar Krueger, Wietske van der Zwaag, Pierre-François Van de Moortele and Rolf Gruetter. *MP2RAGE, a self bias-field corrected sequence for improved segmentation and T1-mapping at high field*. *NeuroImage*, vol. 49, no. 2, pages 1271–1281, jan 2010. (Cited on pages 27 and 70.)
- [Maumet 2014] Camille Maumet, Pierre Maurel, Jean-Christophe Ferré and Christian Barillot. *Robust estimation of the cerebral blood flow in arterial spin labelling*. *Magnetic Resonance Imaging*, vol. 32, no. 5, pages 497 – 504, 2014. (Cited on page 66.)
- [Meurée 2019] Cédric Meurée, Pierre Maurel, Jean-Christophe Ferré and Christian Barillot. *Patch-based super-resolution of arterial spin labeling magnetic resonance images*. *NeuroImage*, vol. 189, pages 85–94, apr 2019. (Cited on page 84.)
- [Morgan 2004] Paul S. Morgan, Richard W. Bowtell, Dominick J.O. McIntyre and Brian S. Worthington. *Correction of spatial distortion in EPI due to inhomogeneous static magnetic fields using the reversed gradient method*. *Journal of Magnetic Resonance Imaging*, vol. 19, no. 4, pages 499–507, 2004. (Cited on page 56.)
- [Mugler 1990] John P. Mugler and James R. Brookeman. *Three-dimensional magnetization-prepared rapid gradient-echo imaging (3D MP RAGE)*. *Magnetic Resonance in Medicine*, vol. 15, no. 1, pages 152–157, jul 1990. (Cited on pages 27 and 57.)
- [Musiek 2012] Erik S. Musiek, Yufen Chen, Marc Korczykowski, Babak Saboury, Patricia M. Martinez, Janet S. Reddin, Abass Alavi, Daniel Y. Kimberg, David A. Wolk, Per Julin, Andrew B. Newberg, Steven E. Arnold and



- John A. Detre. *Direct comparison of fluorodeoxyglucose positron emission tomography and arterial spin labeling magnetic resonance imaging in Alzheimers disease*. *Alzheimers & Dementia*, vol. 8, no. 1, pages 51–59, jan 2012. (Cited on page 9.)
- [Mutsaerts 2015] Henri J.M.M. Mutsaerts, Matthias J.P. van Osch, Fernando O. Zelaya, Danny J.J. Wang, Wibeke Nordhøy, Yi Wang, Stephen Wastling, Maria A. Fernandez-Seara, E.T. Petersen, Francesca B. Pizzini, Sameeha Fallatah, Jeroen Hendrikse, Oliver Geier, Matthias Günther, Xavier Golay, Aart J. Nederveen, Atle Bjørnerud and Inge R. Groote. *Multi-vendor reliability of arterial spin labeling perfusion MRI using a near-identical sequence: Implications for multi-center studies*. *NeuroImage*, vol. 113, pages 143–152, jun 2015. (Cited on pages 38 and 41.)
- [Okell 2013] Thomas W Okell, Michael A Chappell, Michael E Kelly and Peter Jezzard. *Cerebral Blood Flow Quantification Using Vessel-Encoded Arterial Spin Labeling*. *Journal of Cerebral Blood Flow & Metabolism*, vol. 33, no. 11, pages 1716–1724, aug 2013. (Cited on page 20.)
- [Østergaard 1996] Leif Østergaard, Robert M. Weisskoff, David A. Chesler, Carsten Gyldensted and Bruce R. Rosen. *High resolution measurement of cerebral blood flow using intravascular tracer bolus passages. Part I: Mathematical approach and statistical analysis*. *Magnetic Resonance in Medicine*, vol. 36, no. 5, pages 715–725, nov 1996. (Cited on pages 12 and 72.)
- [Owen 2018] David Owen, Andrew Melbourne, Zach Eaton-Rosen, David L. Thomas, Neil Marlow, Jonathan Rohrer and Sébastien Ourselin. *Deep Convolutional Filtering for Spatio-Temporal Denoising and Artifact Removal in Arterial Spin Labelling MRI*. In *Medical Image Computing and Computer Assisted Intervention – MICCAI 2018*, pages 21–29. Springer International Publishing, 2018. (Cited on page 66.)
- [Parkes 2002] Laura M. Parkes and Paul S. Tofts. *Improved accuracy of human cerebral blood perfusion measurements using arterial spin labeling: Accounting for capillary water permeability*. *Magnetic Resonance in Medicine*, vol. 48, no. 1, pages 27–41, jun 2002. (Cited on page 26.)
- [Parkes 2004] Laura M. Parkes, Waqar Rashid, Declan T. Chard and Paul S. Tofts. *Normal cerebral perfusion measurements using arterial spin labeling: Reproducibility, stability, and age and gender effects*. *Magnetic Resonance in Medicine*, vol. 51, no. 4, pages 736–743, 2004. (Cited on page 70.)
- [Petr 2010a] Jan Petr, Jean-Christophe Ferre, Jean-Yves Gauthier and Christian Barillot. *Denoising arterial spin labeling MRI using tissue partial volume*. *Proc.SPIE*, vol. 7623, pages 7623 – 7623 – 9, 2010. (Cited on pages 66, 67 and 79.)

- [Petr 2010b] Jan Petr, Jean-Christophe Ferre, Jean-Yves Gauvrit and Christian Barillot. *Improving arterial spin labeling data by temporal filtering*. Proc.SPIE, vol. 7623, pages 7623 – 7623 – 9, 2010. (Cited on page 66.)
- [Pham 2017] Chi-Hieu Pham, Ronan FABLET and François Rousseau. Multi-scale brain MRI super-resolution using deep 3D convolutional networks. working paper or preprint, November 2017. (Cited on page 66.)
- [Phelps 1979] M. E. Phelps, S. C. Huang, E. J. Hoffman, C. Selin, L. Sokoloff and D. E. Kuhl. *Tomographic measurement of local cerebral glucose metabolic rate in humans with (F-18)2-fluoro-2-deoxy-D-glucose: Validation of method*. Annals of Neurology, vol. 6, no. 5, pages 371–388, nov 1979. (Cited on page 11.)
- [Prince 2005] Jerry L. Prince. Medical imaging signals and systems. Prentice Hall, apr 2005. (Cited on pages 11 and 12.)
- [Proisy 2016] M. Proisy, B. Bruneau, C. Rozel, C. Tréguier, K. Chouklati, L. Rifaud, P. Darnault and J.-C. Ferré. *Arterial spin labeling in clinical pediatric imaging*. Diagnostic and Interventional Imaging, vol. 97, no. 2, pages 151–158, feb 2016. (Cited on pages 10, 103 and 108.)
- [Protter 2009] M. Protter, M. Elad, H. Takeda and P. Milanfar. *Generalizing the Nonlocal-Means to Super-Resolution Reconstruction*. IEEE Transactions on Image Processing, vol. 18, no. 1, pages 36–51, jan 2009. (Cited on pages 67 and 68.)
- [Pruessmann 1999] Klaas P. Pruessmann, Markus Weiger, Markus B. Scheidegger and Peter Boesiger. *SENSE: Sensitivity encoding for fast MRI*. Magnetic Resonance in Medicine, vol. 42, no. 5, pages 952–962, nov 1999. (Cited on pages 23, 40 and 46.)
- [Rousseau 2006] Francois Rousseau, Orit A. Glenn, Bistra Iordanova, Claudia Rodriguez-Carranza, Daniel B. Vigneron, James A. Barkovich and Colin Studholme. *Registration-Based Approach for Reconstruction of High-Resolution In Utero Fetal MR Brain Images*. Academic Radiology, vol. 13, no. 9, pages 1072–1081, sep 2006. (Cited on page 66.)
- [Rousseau 2010a] F. Rousseau, K. Kim, C. Studholme, M. Koob and J. L. Dietemann. *On super-resolution for fetal brain MRI*. Med Image Comput Comput Assist Interv, vol. 13, no. Pt 2, pages 355–362, 2010. (Cited on page 66.)
- [Rousseau 2010b] François Rousseau. *A non-local approach for image super-resolution using intermodality priors*. Medical Image Analysis, vol. 14, no. 4, pages 594–605, aug 2010. (Cited on pages 66, 67 and 68.)

- [Rueda 2013] Andrea Rueda, Norberto Malpica and Eduardo Romero. *Single-image super-resolution of brain MR images using overcomplete dictionaries*. Medical Image Analysis, vol. 17, no. 1, pages 113–132, jan 2013. (Cited on page 66.)
- [Ruthotto 2012] L Ruthotto, H Kugel, J Olesch, B Fischer, J Modersitzki, M Burger and C H Wolters. *Diffeomorphic susceptibility artifact correction of diffusion-weighted magnetic resonance images*. Physics in Medicine and Biology, vol. 57, no. 18, pages 5715–5731, sep 2012. (Cited on pages vii, 56 and 57.)
- [Ruthotto 2013] Lars Ruthotto, Siawoosh Mohammadi, Constantin Heck, Jan Modersitzki and Nikolaus Weiskopf. *Hyperelastic Susceptibility Artifact Correction of DTI in SPM*. In Bildverarbeitung für die Medizin 2013, pages 344–349. Springer Berlin Heidelberg, 2013. (Cited on pages vii, 56 and 57.)
- [Scherrer 2012] Benoit Scherrer, Ali Gholipour and Simon K. Warfield. *Super-resolution reconstruction to increase the spatial resolution of diffusion weighted images from orthogonal anisotropic acquisitions*. Medical Image Analysis, vol. 16, no. 7, pages 1465–1476, oct 2012. (Cited on page 66.)
- [Shi 2015] Feng Shi, Jian Cheng, Li Wang, Pew-Thian Yap and Dinggang Shen. *LRTV: MR Image Super-Resolution With Low-Rank and Total Variation Regularizations*. IEEE Transactions on Medical Imaging, vol. 34, no. 12, pages 2459–2466, dec 2015. (Cited on page 66.)
- [Smith 2004] Stephen M. Smith, Mark Jenkinson, Mark W. Woolrich, Christian F. Beckmann, Timothy E.J. Behrens, Heidi Johansen-Berg, Peter R. Bannister, Marilena De Luca, Ivana Drobnjak, David E. Flitney, Rami K. Niazy, James Saunders, John Vickers, Yongyue Zhang, Nicola De Stefano, J. Michael Brady and Paul M. Matthews. *Advances in functional and structural MR image analysis and implementation as FSL*. NeuroImage, vol. 23, pages S208–S219, jan 2004. (Cited on page 57.)
- [Speck 2000] Oliver Speck, Linda Chang, N. Menaka DeSilva and Thomas Ernst. *Perfusion MRI of the human brain with dynamic susceptibility contrast: Gradient-echo versus spin-echo techniques*. Journal of Magnetic Resonance Imaging, vol. 12, no. 3, pages 381–387, 2000. (Cited on page 12.)
- [SPM 2006] Statistical parametric mapping: The analysis of functional brain images. Academic Press, 2006. (Cited on pages vi, 27, 57, 70 and 87.)
- [Steenkiste 2016] Gwendolyn Van Steenkiste, Dirk H. J. Poot, Ben Jeurissen, Arnold J. den Dekker, Floris Vanhevel, Paul M. Parizel and Jan Sijbers. *Super-resolution T1 estimation: Quantitative high resolution T1 mapping from a set of low resolution T1-weighted images with different slice orientations*. Magnetic Resonance in Medicine, vol. 77, no. 5, pages 1818–1830, jul 2016. (Cited on page 66.)

- [Tortora 2017] Domenico Tortora, Peter Angelo Mattei, Riccardo Navarra, Valentina Panara, Rita Salomone, Andrea Rossi, John A. Detre and Massimo Caulo. *Prematurity and brain perfusion: Arterial spin labeling MRI*. NeuroImage: Clinical, vol. 15, pages 401–407, 2017. (Cited on page 53.)
- [Vardal 2013] Jonas Vardal, Raimo A. Salo, Christopher Larsson, Anders M. Dale, Dominic Holland, Inge Rasmus Groote and Atle Bjørnerud. *Correction of B0-Distortions in Echo-Planar-Imaging-Based Perfusion-Weighted MRI*. Journal of Magnetic Resonance Imaging, vol. 39, no. 3, pages 722–728, oct 2013. (Cited on page 56.)
- [Vidorreta 2013] Marta Vidorreta, Ze Wang, Ignacio Rodríguez, María A. Pastor, John A. Detre and María A. Fernández-Seara. *Comparison of 2D and 3D single-shot ASL perfusion fMRI sequences*. NeuroImage, vol. 66, pages 662–671, feb 2013. (Cited on page 23.)
- [Voss 2006] Henning U. Voss, Richard Watts, Aziz M. Ulug and Doug Ballon. *Fiber tracking in the cervical spine and inferior brain regions with reversed gradient diffusion tensor imaging*. Magnetic Resonance Imaging, vol. 24, no. 3, pages 231–239, apr 2006. (Cited on page 56.)
- [Wang 2003] Jiongjiong Wang, David C. Alsop, Hee Kwon Song, Joseph A. Maldjian, Kathy Tang, Alana E. Salvucci and John A. Detre. *Arterial transit time imaging with flow encoding arterial spin tagging (FEAST)*. Magnetic Resonance in Medicine, vol. 50, no. 3, pages 599–607, aug 2003. (Cited on page 23.)
- [Wang 2005] Ze Wang, Jiongjiong Wang and John A. Detre. *Improved data reconstruction method for GRAPPA*. Magnetic Resonance in Medicine, vol. 54, no. 3, pages 738–742, 2005. (Cited on page 23.)
- [Warmuth 2003] Carsten Warmuth, Matthias Günther and Claus Zimmer. *Quantification of Blood Flow in Brain Tumors: Comparison of Arterial Spin Labeling and Dynamic Susceptibility-weighted Contrast-enhanced MR Imaging*. Radiology, vol. 228, no. 2, pages 523–532, aug 2003. (Cited on pages 8 and 72.)
- [Weber 2006] M. A. Weber, S. Zoubaa, M. Schlieter, E. Juttler, H. B. Huttner, K. Geletneky, C. Ittrich, M. P. Lichy, A. Kroll, J. Debus, F. L. Giesel, M. Hartmann and M. Essig. *Diagnostic performance of spectroscopic and perfusion MRI for distinction of brain tumors*. Neurology, vol. 66, no. 12, pages 1899–1906, jun 2006. (Cited on page 8.)
- [Weiduschat 2013] Nora Weiduschat and Marc J. Dubin. *Prefrontal cortical blood flow predicts response of depression to rTMS*. Journal of Affective Disorders, vol. 150, no. 2, pages 699–702, sep 2013. (Cited on page 10.)
- [Wells 2009] Jack A Wells, Mark F Lythgoe, Mankin Choy, David G Gadian, Roger J Ordidge and David L Thomas. *Characterizing the Origin of the*

- Arterial Spin Labelling Signal in MRI Using a Multiecho Acquisition Approach*. *Journal of Cerebral Blood Flow & Metabolism*, vol. 29, no. 11, pages 1836–1845, aug 2009. (Cited on page 13.)
- [Williams 1992] D. S. Williams, J. A. Detre, J. S. Leigh and A. P. Koretsky. *Magnetic resonance imaging of perfusion using spin inversion of arterial water*. *Proceedings of the National Academy of Sciences*, vol. 89, no. 1, pages 212–216, jan 1992. (Cited on page 16.)
- [Wintermark 2005] Max Wintermark, Musa Sesay, Emmanuel Barbier, Katalin Borbe  
ly, William P. Dillon, James D. Eastwood, Thomas C. Glenn, Ce  
cile B. Grandin, Salvador Pedraza, Jean-Franc  
ois Soustiel, Tadashi Nariai, Greg Zaharchuk, Jean-Marie Caille  
, Vincent Dousset and Howard Yonas. *Comparative Overview of Brain Perfusion Imaging Techniques*. *Stroke*, vol. 36, no. 9, sep 2005. (Cited on pages 11 and 12.)
- [Wolf 2012] Robert Christian Wolf, Philipp Arthur Thomann, Fabio Sambataro, Nenad Vasic, Markus Schmid and Nadine Donata Wolf. *Orbitofrontal cortex and impulsivity in borderline personality disorder: an MRI study of baseline brain perfusion*. *European Archives of Psychiatry and Clinical Neuroscience*, vol. 262, no. 8, pages 677–685, mar 2012. (Cited on page 10.)
- [Wong 1997] Eric C. Wong, Richard B. Buxton and Lawrence R. Frank. *Implementation of quantitative perfusion imaging techniques for functional brain mapping using pulsed arterial spin labeling*. *NMR in Biomedicine*, vol. 10, no. 4-5, pages 237–249, jun 1997. (Cited on page 19.)
- [Wong 1998] Eric C. Wong, Richard B. Buxton and Lawrence R. Frank. *Quantitative imaging of perfusion using a single subtraction (QUIPSS and QUIPSS II)*. *Magnetic Resonance in Medicine*, vol. 39, no. 5, pages 702–708, may 1998. (Cited on page 19.)
- [Wong 2007] Eric C. Wong. *Vessel-encoded arterial spin-labeling using pseudocontinuous tagging*. *Magnetic Resonance in Medicine*, vol. 58, no. 6, pages 1086–1091, 2007. (Cited on page 20.)
- [Wu 2007] Wen-Chau Wu, María Fernández-Seara, John A. Detre, Felix W. Wehrli and Jiongjiiong Wang. *A theoretical and experimental investigation of the tagging efficiency of pseudocontinuous arterial spin labeling*. *Magnetic Resonance in Medicine*, vol. 58, no. 5, pages 1020–1027, 2007. (Cited on page 71.)
- [Yoshiura 2009] Takashi Yoshiura, Akio Hiwatashi, Tomoyuki Noguchi, Koji Yamashita, Yasumasa Ohyagi, Akira Monji, Eiki Nagao, Hironori Kamano, Osamu Togao and Hiroshi Honda. *Arterial spin labelling at 3-T MR imaging*

*for detection of individuals with Alzheimer's disease.* European Radiology, vol. 19, no. 12, pages 2819–2825, jul 2009. (Cited on page 9.)

[Yun 2012] Tae Jin Yun, Chul-Ho Sohn, Moon Hee Han, Byung-Woo Yoon, Hyun-Seung Kang, Jeong Eun Kim, Jin Chul Paeng, Seung Hong Choi, Ji hoon Kim and Kee-Hyun Chang. *Effect of carotid artery stenting on cerebral blood flow: evaluation of hemodynamic changes using arterial spin labeling.* Neuroradiology, vol. 55, no. 3, pages 271–281, oct 2012. (Cited on page 8.)

[Zhao 2017] Moss Y. Zhao, Melvin Mezue, Andrew R. Segerdahl, Thomas W. Okell, Irene Tracey, Yingyi Xiao and Michael A. Chappell. *A systematic study of the sensitivity of partial volume correction methods for the quantification of perfusion from pseudo-continuous arterial spin labeling MRI.* NeuroImage, vol. 162, pages 384–397, nov 2017. (Cited on pages 77, 79 and 80.)



# Communications

---

## Peer-reviewed journals

Cédric Meurée, Pierre Maurel, Jean-Christophe Ferré, Christian Barillot, *Patch-based super-resolution of arterial spin labeling magnetic resonance images*, NeuroImage, vol. 189, 2019, pp. 85-94

## Abstract conferences

Cédric Meurée, Pierre Maurel, Élise Bannier, Christian Barillot, *Patch-based super-resolution for arterial spin labeling MRI*, International Society for Magnetic Resonance in Medicine 25th Annual Meeting & Exhibition (ISMRM), 2017, Honolulu, United States

## Workshop communications

Cédric Meurée, Élise Bannier, Irène Tropres, Jan Warnking, Jean-Christophe Ferré, Marie Chupin, Isabelle Corouge, Christian Barillot, *Standardization and quality control of ASL scans in multicenter neuroimaging studies*, March 2015, European cooperation in science and technology workshop, Les Diablerets, Switzerland

Cédric Meurée, Élise Bannier, Irène Tropres, Jan Warnking, Jean-Christophe Ferré, Marie Chupin, Isabelle Corouge, Christian Barillot, *Standardization and quality control of ASL scans in multicenter neuroimaging studies*, October 2015, European cooperation in science and technology workshop, Airth, United Kingdom

## Software

Integration of a super-resolution module into the Siemens Healthineers postprocessing *syngo.via* Frontier prototype: MR ASL Perfusion Analysis (<http://www.siemens.com/syngo.via-frontier>)



